UNIVERSITY OF SOUTHAMPTON

FACULITY OF ENGINEERING SCIENCE AND MATAMATICS

School of Chemistry

The electrodeposition of bulk and mesoporous lead telluride films onto gold and silicon substrates

by

Robert J. Hudson M.Sc.

Thesis for the degree of Master of Philosophy

October 2008

UNIVERSITY OF SOUTHAMPTON

FACULTY OF SCIENCE MATHEMATICS AND ENGINEERING

SCHOOL OF CHEMISTRY

Master of Philosophy

ABSTRACT

By Robert J. Hudson

Lead telluride is a semi-conductor with a band gap in the infra-red region of the electromagnetic spectrum. This makes it a very useful material for infrared radiation detectors, thermal imaging and photovoltaic devices. Thin films of lead telluride are often produced by expensive and technically complex methods including chemical vapour deposition and molecular beam epitaxy. Electrochemical deposition provides a cheaper and easier way to produce these films. Recently the fabrication of electrodeposited films of metals and semiconductors with a mesoporous structure has been investigated. Due to their increased surface area and the dimensions of the mesoporous structure these materials are expected to exhibit enhanced properties compared to bulk films of the same materials. These include increased photovoltaic efficiency due to the fact the materials are almost entirely composed of surface atoms, they also can have greatly improved catalytic activity.

This thesis describes the fabrication of bulk and mesoporous lead telluride films on silicon and gold-on-glass substrates. The electrochemistry of lead telluride deposition was investigated using cyclic voltammetry which demonstrated the under potential co-deposition process. Bulk films were deposited onto gold and silicon over a range of potentials. The film morphology and composition were investigated using SEM, EDXS and wide angle XRD. Most films were powdery and had poor adhesion however shorter durations of deposition gave better film quality. Mesoporous films were deposited by liquid crystal templating using the surfactant octaethylene glycol monohexadecyl ether in the hexagonal phase. Mesoporous films on silicon often peeled off during removal of the liquid crystal. To improve adhesion chemical modification of the silicon wafer using 3-mercaptopropyl-trimethoxysilane was investigated. The film adhesion dramatically improved and small angle XRD of the films suggested that a mesoporous structure was present. The film composition determined by EDXS however showed that the films were tellurium rich. A double pulse nucleation technique was also employed to improve film adhesion and morphology. Films deposited onto silicon using this technique did show some improvement in quality compared to films deposited without this technique or chemical modification. Small angle XRD of films deposited onto gold using the double pulse regime again indicated the possibility of a mesoporous structure being present. Atomic force microscopy (AFM) was also used to examine the surface morphology of some deposited films and etched silicon substrates.

Contents

List of figures and tables

List of figures

Chapter 1:

Chapter 2

Chapter 3

Chapter 4

List of Tables

Chapter 1

Chapter 3

Declaration of authorship

I, Robert J. Hudson declare that the thesis entitled "*The electrodeposition of bulk and mesoporous lead telluride films onto gold and silicon substrates*" and the work presented in the thesis are both my own and have been generated by me as the result of my own original research. I confirm that:

- This work was done wholly or mainly while in the candidature for a research degree at this university.
- Where any part of this thesis has previously been submitted for a degree or any other qualification at this university or any other institution, this has been clearly stated.
- Where I have consulted the published work of others the source is always clearly attributed.
- Where I have quoted from the work of others, the source is always given. With the exception of such quotations, this thesis is entirely my own work.
- I have acknowledged all main sources of help.
- Where the thesis is based on work done by myself jointly with others, I have made clear exactly what was done by others and what I have contributed myself.
- None of this work has been published before submission.

Signed: .....

Date: .....

Acknowledgements

Firstly I would like to thank my supervisor Dr. Iris Nandhakumar for giving me this research project to work on. I have at times found it both challenging and infuriating! I appreciate her help and guidance and of course her patience. I also thank Dr Peter Birkin, my advisor as well. A big thank you should also go to Dr. Xiahong Li who also gave me plenty of help and advice with my practical work in the lab. Over in the School of Physics I would like to say thank you to Zondy Webber, the nano-fabrication laboratory technician who helped me so much with the AFM which I found so difficult and frustrating on many occasions. Another person I must mention is Marjory Webber my mentor from the University disabilities service. Without her help things would probably have been so much harder on several occasions over the last two years. Thanks also to Rev. Simon Stevens (the chaplain at the University chaplaincy) for also helping me out on several occasions and being an extra source of support and someone to discuss difficult issues with, I really appreciated your advice. A thank you to my friends here as well like Steve Moore (Smoore), and Luke Virgo for putting up with me as well, especially in that cramped tent in the pouring rain! Also I should include my ex-housemates, Steve and Andy and friends back in St. Albans for keeping in touch and showing so much interest in my life and work in Southampton. Of course I must not forget my family, Dad and Monica who have also helped me so much. Finally I thank the EPSRC for funding me, without it none of this could have been possible.

Abbreviations and symbols used

Å	Angstroms
AFM	atomic force microscopy
at.%	atomic percent composition
Brij	registered trademark of ICI Americas Inc.
c	speed of light
CTAB	cetyltrimethylammonium bromide
CuK_α	copper K_α radiation
CV	cyclic voltammetry
$C_{12}EO_4$	tetraethylene glycol monododecyl ether
$C_{16}EO_8$	octaethylene glycol monohexadecyl ether
D	pore to pore repeat distance
d	lattice spacing distance
$d_{(100)}$	spacing of the (100) planes
E	potential, energy
EDXS	energy dispersive x-ray spectroscopy
eV	electron volts
F	Faraday constant
FTIR	Fourier transform infrared spectroscopy
GPES	general purpose electrochemical system
h	Planck's constant
H_1	hexagonal lyotropic phase
H_1-eX	electrodeposited material 'X' with hexagonal mesoporous structure
HF	hydrofluoric acid
HNO_3	nitric acid
I_1	cubic micellar lyotropic phase
IPA	isopropyl alcohol
IR	infra-red radiation
JCPDS	Joint Committee on Powder Diffraction Standards
L_α	lamellar lyotropic phase
L_1	lamellar lyotropic phase
MCM-41S	Mobil corporation material series

3-MPTMS	3-mercaptopropyltrimethoxysilane
n	number of electrons transferred
$Pb(Ac)_2$	lead (II) acetate
PbTe	lead telluride
POE	polyoxyethylene surfactant
POM	polarising optical microscopy
SAXD	small angle x-ray diffraction
SCE	saturated calomel electrode
SEM	scanning electron microscopy/microscope/micrograph
SHE	standard hydrogen electrode
TCO	transparent conducting oxide
TEM	transmission electron microscopy/microscope/micrograph
TeO_2	tellurium dioxide
TLCT	true liquid crystal templating
V	volts
V_1	cubic lyotropic phase
v/v	volume to volume
w/w	weight to weight
WAXD	wide angle x-ray diffraction
wt.%	weight percent
XRD	x-ray diffraction
α	absorption coefficient
λ	wavelength
θ	diffraction angle
ΔE	potential shift
ΔG°_{f}	standard free energy of formation

Aims and objectives

The principle aim of this research is the fabrication of nanostructured mesoporous films of the semiconductor lead telluride on to silicon wafer substrates by means of electrodeposition. Deposition onto silicon is of interest as this would provide a means of integrating these films directly into electronic devices improving their efficiency. The deposition process will employ the liquid crystal templating method to create the mesoporous structure using the surfactant octaethylene glycol monohexadecyl ether $C_{16}EO_8$. Objectives include investigating the electrochemistry of the deposition of lead telluride using cyclic voltammetry and the deposition of bulk (non-mesoporous films). Analysis of the deposited films will investigate the elemental composition by energy dispersive x-ray scattering, film morphology and thickness measurements by scanning electron microscopy and the crystal structure using wide angle x-ray diffraction. The presence of a mesoporous film structure will be determined by small angle x-ray diffraction. Measurement of the optical band gap energy of deposited films will also be undertaken using FTIR spectroscopy and film thickness measurement using SEM. Atomic force microscopy is also used to study the surfaces of deposited films and investigate the surface of silicon substrates.

Chapter 1

Introduction and Background

1. Introduction and background

1.1 Introducing lead telluride and its applications

Lead telluride (PbTe) belongs to a group of materials known as the chalcogenides. These compounds can be classified as being binary or ternary, containing either one or two metallic elements combined with an element from the oxygen group (sulphur, selenium or tellurium). Lead telluride is itself a binary chalcogenide, an example of a ternary compound is mercury cadmium telluride (HgCdTe). Lead telluride and the other binary lead chalcogenides, PbS and PbSe have a face centred cubic (NaCl) crystal structure. The co-ordination number of the crystal lattice structure is six with each atom being bound to six other atoms. The bond between the lead and the chalcogenide atoms is mostly ionic in character [1]. The scanning electron micrograph below shows electrodeposited lead telluride crystals demonstrating the cubic crystal structure.

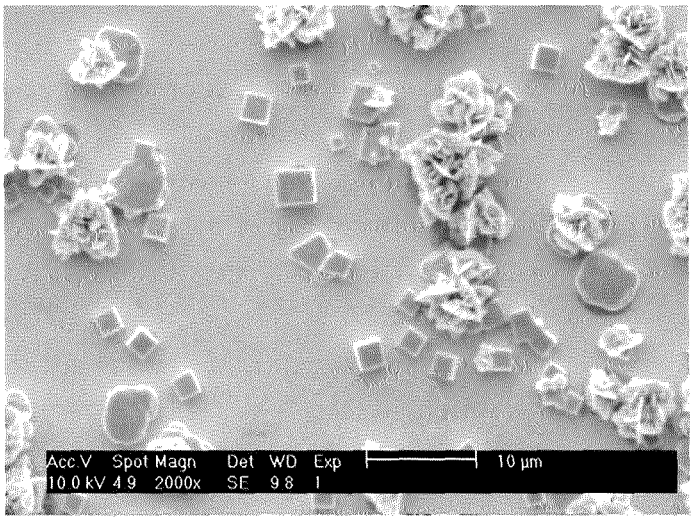

Fig. 1.1 SEM micrograph of electrodeposited lead telluride crystals
Scale bar is 10 µm

Lead chalcogenides have semiconductor properties, i.e. having an electrical conductivity between a conductor and an insulator and they have narrow band gaps [2,3,4,5] generally ranging from 0.278 to 0.310 eV [6]. Table 1.1 on the next page gives the band gap and density of PbS, PbSe and PbTe.

Table 1.1 Band-gap and density data for the binary lead chalcogenides

	PbS	PbSe	PbTe
band gap (eV) at 77 K	0.307 [1]	0.176 [1]	**0.217** [1]
band gap (eV)at 300 K	0.41 [1]	0.27 [1]	**0.31** [1]
band gap (eV) at 373 K	0.44 [1]	0.31 [1]	**0.34** [1]
density, g/cm^3	7.61 [7]	8.15 [7]	**8.16** [7]

From the table it can be seen that the band gap energy increases with temperature this is a unique property of lead chalcogenides, for other semiconductors the band gap decreases with increasing temperature. This is probably due to their semi-metallic properties. The type of conductivity can be controlled by the stoichiometry of the lead chalcogenide. An excess of Pb creates n-type conductivity whereas an excess of the chalcogenide makes p-type conductivity [5]. Crucially the band gap energy range of lead telluride falls into the infrared region of the electromagnetic spectrum thus making them strongly absorbent of this radiation. Because of this they have been employed in many infrared applications for example lead telluride films on silicon have been fabricated and used for IR detectors [8,9]. Lead chalcogenide films on silicon have been used in thermal imaging arrays [10,11] and have also been investigated for space applications [12]. Lead sulphide thin films have been used in glass window panes as a thermal control coating to reduce heat loss from buildings [13]. Lead telluride could also be used as a source of "clean" electricity, as it is a thermoelectric material. When a temperature gradient is applied to a thermoelectric material a voltage is developed across it. Lead telluride has a high melting point, good chemical stability and strength and is thermally stable up to 900 K [14]. Lead chalcogenides have also been used in laser diodes which emit infrared radiation that can be tuned to a specific wavelength between three and 20 μm. They have been used for the spectroscopic detection of trace gaseous pollutants and atmospheric water vapour and carbon dioxide levels. An added advantage of the lead chalcogenide laser diodes is that they are strongly resistant to radiation damage, therefore they can be used at high altitude or in space as well [15,16]. Laser diodes based on lead chalcogenides have also been used for the detection of chlorohydrocarbon contamination of water with sensitivities of up to 100 μg / litre being reported [17].

Lead chalcogenide films can be produced by a wide range of techniques. Vacuum evaporation is often used for example Zimin *et al* [18] vacuum deposited lead telluride onto porous silicon with a film thickness between 0.55 and 0.74 μm. Parris *et al* [19] also produced vacuum deposited lead telluride. They deposited the films from vaporised lead and tellurium. By changing the partial pressure of the tellurium they were able to adjust the stoicheometry of the deposited film and therefore its semiconductor properties and band gap energy. Chemical vapour deposition has been used to deposit lead sulphide films onto silicon substrates from a precursor compound containing lead and sulphur. At the temperature of the deposition process the compound broke down producing free lead and sulphur which deposited onto the substrate [20]. A lesser used approach to the formation of lead chalcogenide thin films is chemical solution deposition as described by Gorer *et al* who describe the formation of lead selenide films [21]. The film is deposited by two possible processes, an "ion by ion" mechanism where metal and chalcogenide ions precipitate and form the film on the substrate or the "clustering" mechanism where adsorption and coagulation of colloidal particles composed of the precursor elements forms the film on the substrate surface. Molecular beam epitaxy (MBE) is also often used to deposit lead chalcogenide thin films.

1.2 Electrodeposition of lead telluride films

Electrochemical deposition has also been used as a means for deposition of lead chalcogenide films. It has many advantages over the methods noted in the previous section. It is less expensive and technically elaborate as no complex vacuum and vaporising systems are needed and depositions can be carried out at room temperature. With the deposition process it is also much easier to control the composition, and crystal structure. There is also the potential for large area film deposition as well, the only significant drawback is that the substrate has to be electrically conductive [2,3,22,23,24].

1.2.1 A review of electrodeposition of lead telluride in the literature

This section will review the research that has been undertaken concerning the electrodeposition of lead telluride. Little work has been reported in the literature regarding this subject, since as previously explained lead telluride thin films have been produced mostly by non-electrochemical processes. The earliest report is from Saloniemi *et al* [2] they deposited lead telluride films onto copper and tin oxide substrates using a potentiostatic regime. Tellurium dioxide and lead acetate were used in the electroplating solution and ethylendiaminetetraacetic acid (EDTA) as a complexing agent for Pb^{2+}. The solution pH was adjusted to 9.0 with sodium hydroxide to improve the solubility of tellurium dioxide and stability of the Pb-EDTA complex. Initial experiments showed that adhesion of PbTe to copper substrates was good, however for tin oxide substrates adhesion was poor. To improve adhesion tin oxide substrates were subsequently pretreated by electrochemically reducing them in 0.1 M sulphuric acid at -0.1 V *vs.* a saturated calomel electrode (SCE) for 30 seconds prior to deposition. They found that there was a potential range over which the film composition was constant. This was dependent upon the concentration of Pb^{2+} and the substrate. For tin oxide substrates the range was from -0.70 V to -0.90 V vs. SCE, and on copper -0.80 V to -0.95 V *vs.* SCE with a Pb^{2+} concentration of 0.1 M. With 0.05 M Pb^{2+} the ranges were slightly more negative, -0.75 V to 0.95 V for tin oxide and -0.85 V to -0.95 V for copper substrates, the concentration of TeO_2 was constant (1 mM) for all depositions. The films were smooth and dense with a cubic crystalline

structure, although they were tellurium rich with a stoichiometry of 45% Pb to 55% Te.

Streltsov *et al* have demonstrated the electrodeposition of $PbSe_{1-x}Te_x$ where x is between 0 and 1 [25]. They used platinum films vacuum deposited onto (100) silicon substrate as the working electrode with an apparent area of 1 cm^2, a platinum counter electrode and Ag/AgCl reference electrode. The solution consisted of 0.1 M HNO_3, 50 mM $Pb(NO_3)_2$, Se^{4-} and Te^{4-} added to the solution as selenium and tellurium dioxide. The concentrations of the Se and Te anions were varied from 0.1 to 1 mM to give the range of $x = 0$ to 1. Films were deposited cathodically under potentiostatic control at – 0.30 V *vs.* Ag/AgCl. At this potential lead is deposited onto selenium and tellurium simultaneously. By changing the deposition potential over the range from 0 V to -0.30 V during the deposition resulted in creating layers of different composition (PbSe/ $PbSe_{1-x}Te_x$) within the deposited film. Deposited films were crystalline in structure with some excess of amorphous selenium and tellurium. It was shown that the composition of the film could be altered by changing the concentrations of the chalcogenides in the solution and the deposition potential. At more negative potentials the lead content in the deposited film increased and chalcogenide content decreased. Increasing the chalcogenide concentration increased its content in the deposited films.

Eptaxial PbTe films were electrodeposited cathodically onto (111) indium phosphide, InP single crystal wafers by Froment *et al* [26]. They used a three electrode cell with a platinum gauze counter electrode and a saturated KCl-Ag/AgCl electrode. The electroplating bath solution was 0.1 M HNO_3 + 0.05 M $Pb(NO_3)_2$ + 0.001 M TeO_2. The pH was adjusted to 2.2 and the temperature held at 25°C. An excess of cadmium as 0.5 M $Cd(NO_3)_2$ was added to the electrolyte solution as addition of cadmium ions was found to produce stoicheometric and homogeneous films in a previous study [28]. The addition of excess cadmium did improve the film quality, without cadmium rough dendritic films were deposited but with cadmium at a concentration around 0.5 M the films were much smoother. Streltsov *et al* attribute this effect to the inhibition of lead underpotential deposition due to competition between Pb^{2+} and Cd^{2+} which modifies crystal growth direction of the film [27]. During deposition a constant stirring rate was used. The deposited film thickness was 40-50 nm and the films were polycrystalline in structure. Epitaxial growth was poor due to the large lattice mismatch between PbTe and InP.

Mondal *et al* [3] report the electrochemical deposition of lead telluride onto transparent conducting oxide coated (TCO) glass substrates using a solution of 0.1 M lead acetate and 1 mM TeO_2. The pH of the solution was adjusted to 2.0 to allow tellurium dioxide to dissolve, the solution was not stirred during deposition. Their deposition process did not use a potentiostat, instead they used a metallic lead strip as a sacrificial anode connected to the TCO substrate via a copper wire. Pb^{2+} ions were released into solution from the lead anode and the released electrons passed through the copper wire to the TCO substrate (cathode). The Pb^{2+} and $HTeO_2^+$ ions in the solution were attracted to the TCO substrate due to its negative charge and then reduced on its surface to form lead telluride. The reaction was sustained until all the telluryl ions were exhausted. The potential difference between the electrodes therefore provided the driving force for the deposition. Depositions were carried out at 298 K, 313 K and 353 K for up to four hours. Increasing the temperature was found to increase the growth rate and thickness of films due to the increased mobility of the ions in solution. Lead telluride deposits were also observed on the lead strip anode, it was suggested that lead ions were reacting with $HTeO_2^+$ ions on the anode surface to form PbTe. The deposited dark grey films of lead telluride had a uniform and stoicheometric composition and showed good adhesion. X-ray diffraction and SEM analysis showed that the films were polycrystalline, average grain size increased from 60 nm for films deposited at 298 K to 200 nm at 353 K. The infra-red absorption spectrum gave a band gap energy of 0.26 eV, in the region of the literature value for lead telluride, 0.33 eV [28].

Myung *et al* [22] deposited lead telluride onto silicon wafers coated with an evaporated gold thin film. Depositions were carried out potentiostatically using a platinum wire counter electrode and a Ag/AgCl (saturated KCl) reference electrode. They used two different electrolyte solutions to investigate the effect of tellurium concentration on film composition and morphology. One solution had a $HTeO_2^+$ concentration of 10 mM and the other a $HTeO_2^+$ concentration of 0.1 mM, both solutions had Pb^{2+} at a concentration of 0.05 M. Tellurium dioxide and lead nitrate were used to provide Pb^{2+} and $HTeO_2^+$ to aid dissolution of TeO_2 the solution was acidified with nitric acid at a concentration of 1 M. During film deposition the solution was stirred at 300 rpm using a magnetic stirrer. The effect of solution composition, deposition potential and temperature on film composition, crystal structure and morphology was investigated. The films deposited from the 0.1 mM

$HTeO_2^+$ solution were almost stoichiometric (46 at.% Pb, 54 at.% Te) at deposition potentials between -0.14 V and -0.43 V, above -0.43 V the films became lead rich. For films deposited from the 10 mM $HTeO_2^+$ solution the results were much the same with almost stoicheometric films being deposited over the same range of potentials. The crystalline structure and morphology of the deposited films was affected greatly by $HTeO_2^+$ concentration and deposition potential. For films deposited with 10 mM tellurium, 50 mM Pb^{2+} at a potential of -0.12 V a dense, smooth and uniform grey film was formed, the principle crystalline growth was in the (100) direction. At more negative potentials, up to -0.40 V the films were not as smooth and had a dendritic morphology and the growth direction was in the (211) direction. For films deposited using the 0.1 mM tellurium 50 mM Pb^{2+} solution separate cubic PbTe crystals were observed with a deposition potential of -0.12 V, the direction of growth was (100). At -0.13 V no cubic crystals were seen and the direction of growth changed to (111). At -0.15 V a mixed morphology of cubic crystals and dendrites was observed, and at -0.40 V the morphology was dendritic. The deposition temperature also had a marked effect upon film composition. At 300 K the film was almost stoicheometric (46 wt.% Pb) at lower and higher temperatures the films became tellurium rich.

Myung *et al* [29] also electrodeposited lead telluride cubes onto silicon wafers coated with an evaporated gold thin film. They used a potentiostatic deposition regime with a platinum coated titanium sheet counter electrode and a Ag/AgCl (saturated KCl) reference electrode. The electrolyte solution contained 0.1 mM tellurium dioxide and 50 mM lead nitrate acidified with 1 M nitric acid. All depositions were carried out at -0.12 V with stirring of the solution. Analysis of the crystalline deposits by energy dispersive x-ray spectroscopy showed that stoicheometric lead telluride was formed. X-ray diffraction analysis showed that the crystals had a face centred cubic structure which is expected for PbTe, the direction of growth was predominantly in the (100) lattice planes and parallel to the gold substrate surface. The average size of the PbTe crystals increased with duration of deposition. After two minutes the width was 340 nm at 50 minutes it was 720 nm.

Streltsov *et al* [4] electrodeposited lead telluride onto silicon (100) wafers. Films were deposited from a solution containing 50 mM $Pb(NO_3)_2$, 1 mM TeO_2 and 0.1 M HNO_3. The deposition potential was -0.38 V *vs.* Ag/AgCl reference electrode with a platinum counter electrode, the temperature was kept at 20 +/- 2 °C. SEM analysis of the deposit showed cubic crystals on the substrate surface, 80 -180 nm in

size. X –ray diffraction indicted a NaCl type crystal structure which is consistent with the structure for PbTe. The composition of the deposit determined by energy dispersive X –ray analysis (EDXS) was almost stoicheometric, with a Pb:Te element ratio of 0.93 : 1. Cyclic voltammetry of deposited PbTe in 50 mM $Pb(NO_3)_2$ + 0.1 M HNO_3 solution under illumination showed anodic oxidation of the PbTe. This was not seen without illumination. The photo-oxidation of the PbTe was attributed to generation of charge carriers in the silicon substrate.

Nandhakumar *et al* [30] have electrodeposited lead telluride directly onto n-type phosphorous doped silicon (100) wafers with a resistivity of 1 -10 Ω cm. Films were deposited potentiostatically using a saturated calomel reference electrode and a platinum gauze counter electrode. The electrolyte contained 50 mM lead acetate and 1 mM tellurium dioxide. To allow the dissolution of the tellurium dioxide nitric acid was also present at a concentration of 0.1 M. Films were deposited at room temperature with stirring of the solution. The optimum deposition potential was found to be -0.43 V vs. SCE. Deposited films were shiny and metallic with good adherence to the silicon substrate. From the amount of charge passed the theoretical film thickness was calculated to be 584 nm, the actual film thickness measured by SEM was found to be 580 nm. This indicates that the electrodeposition process was very efficient, with a current efficiency of 99.3%. EDXS analysis showed that the composition was uniform across the whole area of the film and stoicheometric, 51.2 at.% Pb / 48.8 at.% Te. X-ray diffraction indicated that the deposited films had a cubic rock salt crystal structure as expected for lead telluride and were polycrystalline. The average grain size was found to be 76 nm. Infrared absorption spectroscopy of the film showed that the band gap energy was 0.31 eV, which is in good agreement with the literature value for lead telluride, 0.33 eV [28].

1.2.2 The electrochemistry of lead telluride deposition and the co-deposition reaction mechanism

a) Overview of the electrochemistry of PbTe deposition

This section will give an overview of the electrochemistry of PbTe electrodeposition and an explanation of the underpotential co-deposition mechanism which is characteristic of this process. Firstly the electrochemical behaviour of the lead and tellurium species present in the solutions used for the deposition of lead telluride needs to be considered. The electrochemistry of tellurium is much more complex than that of lead. It is amphoteric, it can behave as an acid or a base depending upon the pH of the solution and it has multiple oxidation states ranging from Te^{6+} to Te^{2-} [31]. In the work described in this thesis tellurium dioxide was used as the source of tellurium however it is poorly soluble in neutral aqueous solutions. Tellurium dioxide is soluble in strongly acidic solutions below pH 2.0, under this condition tellurium exists as the telluryl cation, $HTeO_2^+$ [3,22,31]. This is initially reduced to tellurium by a four electron reduction reaction as shown in equation (1.1) below [32]:

$$HTeO_2^+ + 3H^+ + 4e^- \longrightarrow Te_{(s)} + 2H_2O \qquad E^o = +0.551 \text{ V vs. SHE} \qquad (1.1)$$

At potentials more negative than -0.60 V *vs.* SCE tellurium deposition occurs by a two step process. Initially generation of H_2Te occurs at the electrode surface as an intermediate species, equation (1.2), H_2Te is unstable in the acid solution and is chemically reduced to tellurium, equation (1.3) [33]

$$HTeO_2^+ + 5H^+ + 6e^- \longrightarrow H_2Te + 2H_2O \qquad (1.2)$$

$$H_2Te + HTeO_2^+ + H^+ + 2e^- \longrightarrow 2Te_{(s)} + 2H_2O \qquad (1.3)$$

Tellurium can also be deposited by a combination of both reactions 1.1 and 1.3 [34]

$$H_2Te + 2HTeO_2^+ + 4H^+ + 6e^- \longrightarrow 3Te_{(s)} + 4H_2O \qquad (1.4)$$

So initially the cathodic deposition of tellurium is a four electron reduction process. Then if the deposition potential is suitable further reduction of tellurium can occur via

an H_2Te intermediate. The reduction of lead is much simpler as given by equation (1.5).

$$Pb^{2+} + 2e^- \longrightarrow Pb_{(s)} \qquad E^o = -0.126 \text{ V vs. SHE} \qquad (1.5)$$

The electrodeposited lead then combines chemically with the electrodeposited tellurium nuclei on the electrode surface to form lead telluride, equation (1.6).

$$Pb_{(s)} + Te_{(s)} \longrightarrow PbTe \qquad (1.6)$$

The overall process can also be expressed as equation (1.7).

$$HTeO_2^+ + Pb^{2+} + 3H^+ + 6e^- \longrightarrow PbTe + 2H_2O \qquad (1.7)$$

The deposition of lead telluride is dependent upon the reduction of tellurium, i.e. formation of tellurium is the rate determining step of the process. Further growth of the lead telluride film proceeds by underpotential deposition of lead onto deposited tellurium and lead telluride and overpotential deposition of tellurium onto deposited lead telluride and bare substrate surface [4,22]. The terms underpotential deposition and overpotential deposition will be explained in the next section.

b) The co-deposition reaction mechanism

The induced co-deposition reaction mechanism refers to where over a particular deposition potential range both metal and chalcogenide will co-deposit to form the film on the substrate. The induced co-deposition reaction was first conceived by Kröger [35]. A basic explanation of this states that the deposition potential of a metal-chalcogenide compound is determined by the less noble (most reactive) element and is more positive than the deposition potential of the less noble element if it was being deposited on its own, i.e. it is under-potentially deposited. At the same time the less reactive element is deposited at a more negative potential than if it was deposited on its own, it is over-potentially deposited. This situation arises because there is an energy gain from the formation of the deposited compound which shifts the deposition potential to a more positive value. In the case of PbTe lead is the less noble component and tellurium is the more noble component. Since the reduction potential of $HTeO_2^+$ to Te is more positive than the deposition potential of lead, the lead concentration must be greatly in excess of the tellurium concentration so that the formation of a stoicheometric film will occur [2,3,5]. Therefore underpotential co-deposition of lead occurs during PbTe formation. The shift in potential caused by the energy gain of PbTe formation can be calculated from (1.8):

$$\Delta E = \Delta G^{o}_{f(PbTe)} / nF \qquad (1.8)$$

Where ΔE is the potential shift in volts, $\Delta G^{o}_{f(PbTe)}$ is the standard free energy of formation of lead telluride from its constituent elements, n is the number of electrons transferred (2) and F is the Faraday constant (96485 C mol^{-1}). The ΔG^{o}_{f} for lead telluride is -69.5 kJ mol^{-1} [36]. This gives a potential shift of:

$$\Delta E = 69500 / 2 \times 96485 \qquad 0.36 \text{ V} \qquad (1.9)$$

from the deposition potential of lead on its own ($E^{o}_{Pb^{2+} > Pb}$ = -0.126 V *vs.* SHE). Therefore lead telluride deposition would be expected to start at; -0.126 V + 0.36 V, 0.234 V *vs.* SHE. The underpotential co-deposition mechanism is shown schematically in figure 1.2 as a current-potential curve. The top two curves show the

deposition of lead and tellurium alone. The bottom curve is the deposition of lead telluride from a solution containing both lead and tellurium.

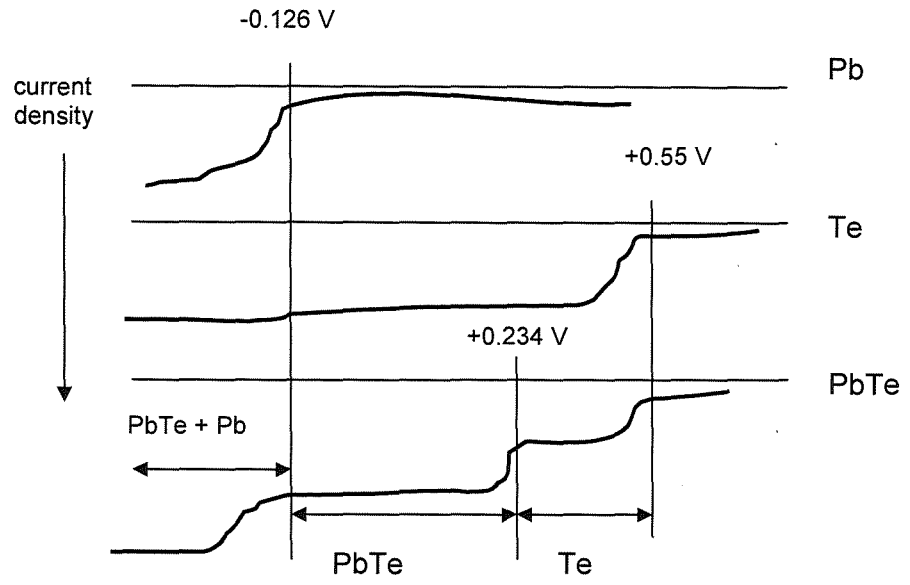

Fig. 1.2 Schematic current-potential curves for deposition of Pb, Te and PbTe
Adapted from reference 37

Voltammetry studies by Myung *et al* [22] and Streltsov *et al* [4] illustrate the co-deposition of lead telluride by comparing the voltammograms of deposition of lead and tellurium alone and from a solution containing both lead and tellurium. The current density observed in the potential range of tellurium deposition when both lead and tellurium was present in solution was much greater then when tellurium was being deposited on its own. At the same potential for lead deposition no current was seen. They attributed this extra current density to the underpotential co-deposition of lead.

1.3. Liquid crystals, their compositions and phase structures

1.3.1 Composition of liquid crystals and surfactants

Liquid crystalline materials are a unique class of materials that exhibit properties that are intermediate between true crystalline solids and liquids. In a crystalline material the atoms/ions or molecules are ordered in a regular lattice structure and movement of them is usually limited at ambient conditions leading to a rigid material. In a liquid there is very little order with the constituent atoms or molecules and they are relatively free to move around. Compared to true crystals the amount of order in a liquid crystal is fairly small, however although the molecules are much freer to move around as they do so they maintain some degree of structural order within the bulk of the material. Liquid crystals can be divided into two major classes, thermotropic and lyotropic. With thermotropic liquid crystals the crystalline phase is formed and is stable over a particular temperature range, they are temperature dependent. Lyotropic liquid crystals are also formed over a specific temperature range but in addition require the presence of a polar solvent at a defined concentration. Lyotropic liquid crystals are therefore always mixtures whereas thermotropic liquid crystals can be just a single compound [38]. For electrodeposition of mesoporous films lyotropic liquid crystals are used since a polar aqueous domain is required for the ionic species to reside in.

In our case lyotropic liquid crystals phases are formed from mixtures of non-ionic polyoxyethylene surfactants and a polar solvent, usually water. The surfactants are bifunctional amphiphillic molecules containing hydrophobic and hydrophilic sections (amphillic means "loving both kinds"). The hydrophobic part is a long aliphatic hydrocarbon chain (often referred to as the tail group). The hydrophilic part consists of either a charged or polar moiety, the head group, the charged group can be either positive (cationic) or negative (anionic). Since these molecules have both hydrophobic and hydrophilic properties they can form ordered structures in polar and non-polar solvents [39]. Examples of a charged (cationic) surfactant, cetyltrimethylammonium bromide and a polar surfactant tetraethylene glycol monododecyl ether ($C_{12}EO_4$) are shown on the next page

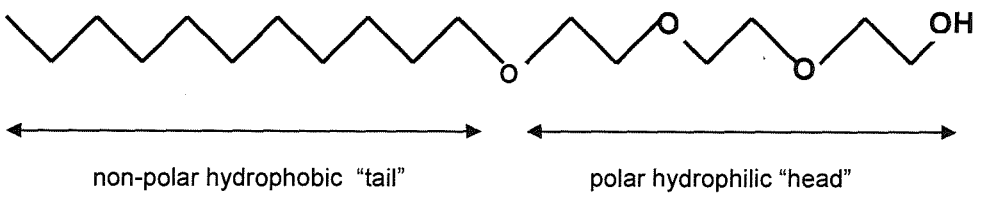

Fig. 1.3 Molecular structure of the surfactant $C_{12}EO_4$ showing its polar and non polar parts

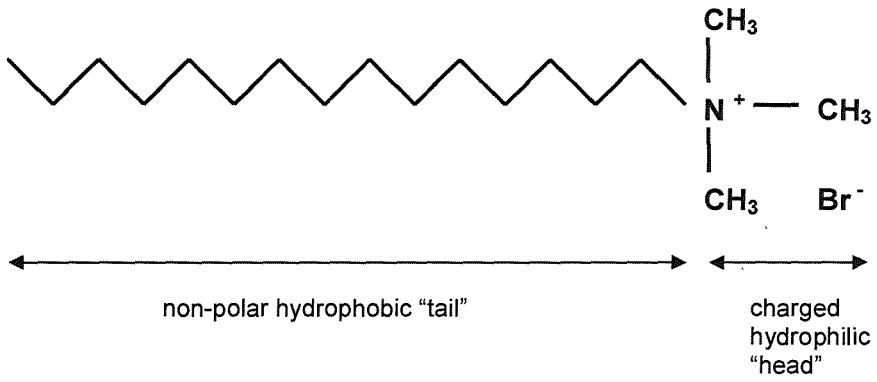

Fig. 1.4 Molecular structure of the ionic surfactant cetyltrimethylammonium bromide (CTAB)

There is a wide range of surfactants that can be used to form liquid crystal structures. Polyoxyethylene (POE) surfactants such as $C_{12}EO_4$ are very expensive in their pure form. The ionic surfactants such as CTAB are much cheaper and have been used for the synthesis of mesoporous silicates. For the electrodeposition of mesoporous films they cannot be used though as the applied potential could affect the arrangement of the surfactant molecules. This is because the positively charged head groups would be drawn towards the cathode, leading to disruption of the liquid crystal structure. Surfactants like Brij 56 are less expensive as they are composed of POE molecules of different chain lengths. Table 1.2 gives examples of surfactants often used in the preparation of mesoporous materials.

Table 1.2 Examples of surfactants used in the preparation of mesoporous materials. From references 31 and 40

Surfactant	Structure	Comments
$C_{16}EO_8$	$CH_3(CH_2)_{15}(OCH_2CH_2)_8OH$	Nonionic POE surfactant, Very expensive
Brij 76	$CH_3(CH2)_{17}(OCH_2CH_2)_{10}OH$ (average chain length)	Nonionic POE surfactant, mixture of chain lengths, cheap
Brij 56	$CH_3(CH2)_{15}(OCH_2CH_2)_{10}OH$ (average chain length)	Nonionic POE surfactant, mixture of chain lengths, cheap
Pluronics	$HO(OCH_2CH_2)_x(OCH_2CH_2CH_2)_y(OCH_2CH_2)_xOH$	Nonionic surfactant, long chain block co-polymer
CTAB	$CH_3(CH2)_{15}N(CH_3)_3Br$	Cationic surfactant, cheap

In the experimental work described in this thesis the POE surfactant octaethylene glycol monohexadecyl ether ($C_{16}EO_8$) was used to create the liquid crystal templating mixtures for deposition of mesoporous films. Figure 1.5 shows a space filling model of $C_{16}EO_8$ alongside $C_{12}EO_8$ and Brij 56.

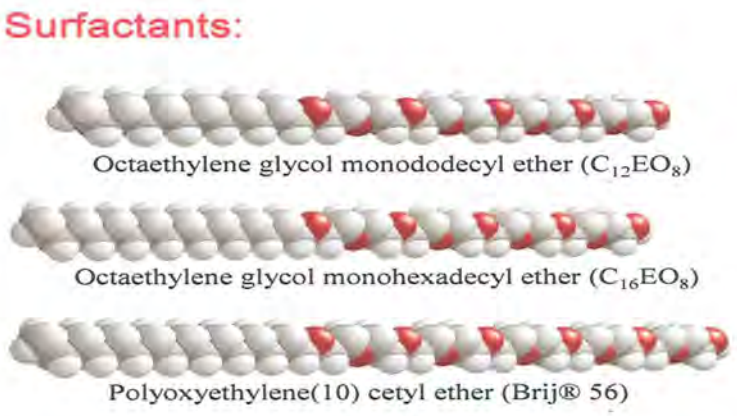

Fig. 1.5 Space filling models of $C_{12}EO_8$, $C_{16}EO_8$ and Brij56®. from reference 41

1.3.2 Liquid crystal phases

As explained earlier surfactants form lyotropic liquid crystals when mixed with a polar solvent whose structure is dependent on the concentration of the surfactant in the solution/mixture as well as the temperature. In fact amphillic molecules are able to arrange themselves into different aggregate structures (phases) depending upon these variables. At very low concentrations in a polar solvent like water the surfactant molecules are randomly diffused throughout the solution. With increasing concentration of surfactant the molecules start to form structures called micelles, the concentration at which this occurs is called the critical micelle concentration. The micelle is a spherical structure where the hydrophobic tails of the molecules are repelled by the solvent and gather together inside the sphere excluding the surrounding polar solvent. The polar head groups form the surface of the sphere and are in contact with the solvent. These micelles are randomly distributed throughout the solution, this is called the micellar phase and is denoted as L_1. At slightly higher concentrations the micelles can sometimes arrange themselves in a regular cubic lattice through the bulk solution. This is the cubic micellar phase, I_1 it is not as common as other liquid crystal phases. Increasing the concentration further the hexagonal liquid crystal phase (H_1) is formed. In this phase the surfactant molecules no longer form spherical micelles but instead arrange themselves into long cylindrical structures. Like the micelles the non-polar tails of the molecules form the core of the cylinders and the polar head groups are on the cylinder surface. The cylinders are organised in a hexagonal close packed structure. The cylinders have a spacing of one to five nanometres depending upon the exact surfactant concentration. The hexagonal phase is very viscous since this structure is relatively rigid. This phase is of most importance to the deposition of mesoporous films. The next phase that can be observed is the cubic phase, V_1. Here the cylindrical structures form a continuous three dimensional network of interconnected channels running through the bulk material. On increasing the surfactant concentration further the lamellar phase (L_α) is produced. This is made up of extensive flat bilayer sheets interspaced with the polar solvent. The surfactant molecules are arranged so that their hydrophobic tails mesh together in the centre with the polar head groups on the surfaces of the sheet in contact with the solvent, forming a structure reminiscent of biological cell

membranes. This phase has low viscosity despite the relatively high surfactant concentration because the bilayer sheets can slide over each other. At extremely high surfactant concentrations inverse hexagonal (H_2) and inverse micellar (L_2) phases are formed. In these phases the surfactant molecule positions are reversed, the polar head groups are on the inside and the hydrophobic tails on the outside of the structures. The figure below shows some of the liquid crystal phase structures just discussed.

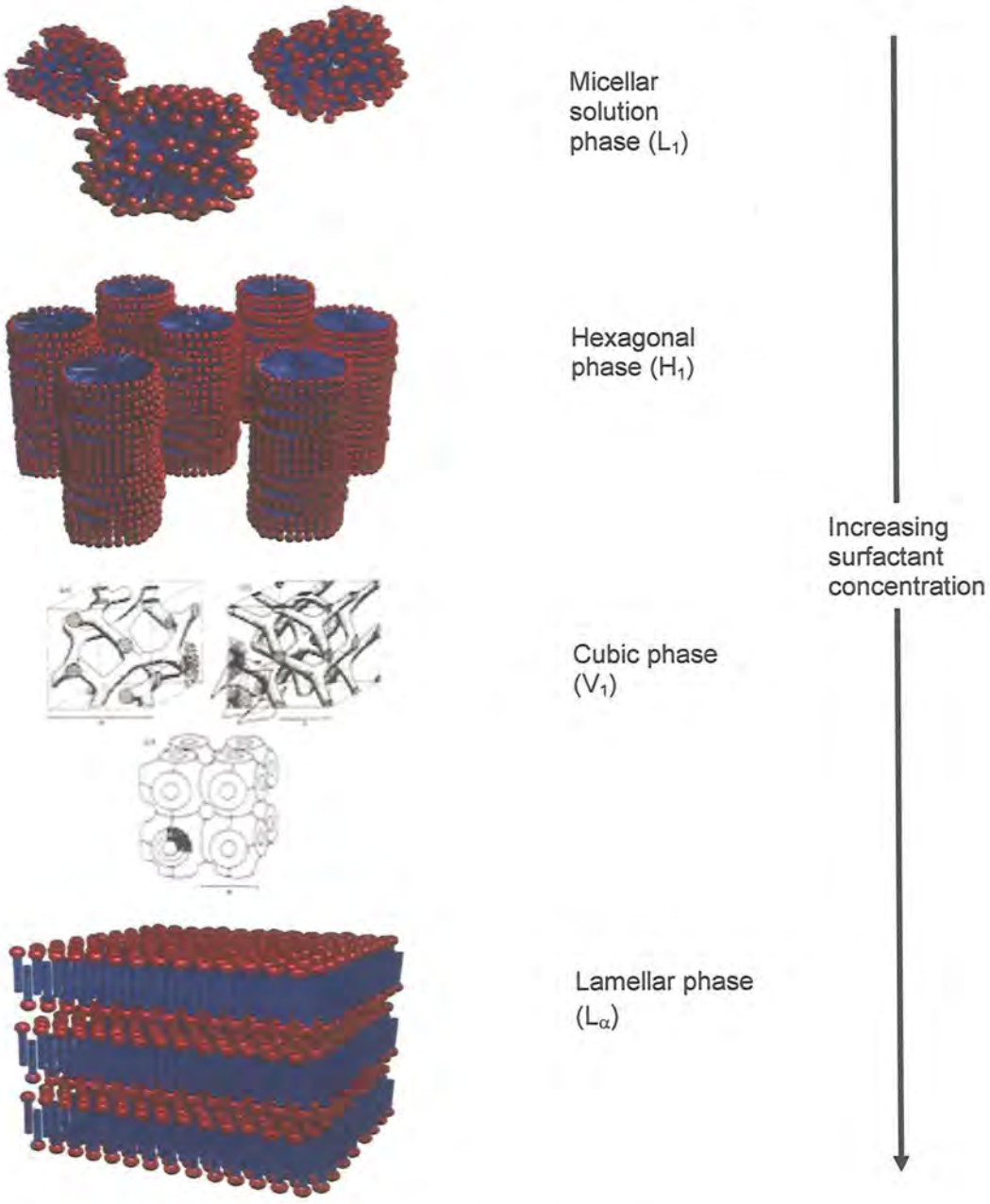

Fig 1.6 Representation of some of the liquid crystal phases obtained with increasing surfactant concentration. Red spheres are head groups, blue rods are the hydrophobic tails. From reference 42

The concentrations and temperature ranges over which the various lyotropic liquid crystal phases of a surfactant are stable can be shown using a phase diagram. Phase diagrams are constructed by plotting observed phase transitions as a function of temperature and surfactant concentration. This is done by using polarising optical microscopy (POM) to study the optical texture changes that occur with transitions from one phase to another, (greater detail is given explaining this in the next section). Small angle x-ray diffraction can also be used to determine the phase of a liquid crystal. Figure 1.7 shows the phase diagram for the surfactant $C_{16}EO_8$ in water.

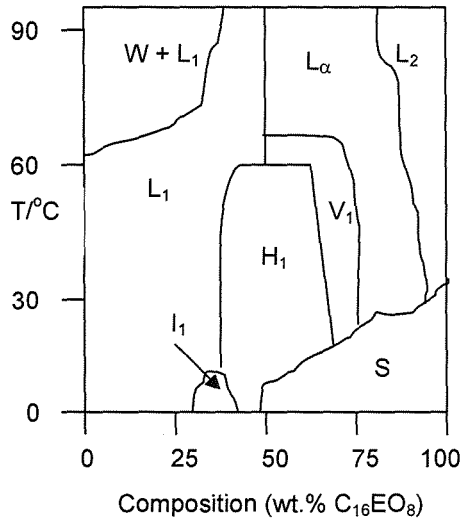

Fig. 1.7 Liquid crystal phase diagrams for the POE surfactant $C_{16}EO_8$ in water. W + L_1, water and micellar biphasic solution, L_1 micellar phase, L_2 inverse micellar phase, L_α lamellar phase, H_1 hexagonal phase, V_1 cubic phase, S solid surfactant Redrawn from reference 43

The lines on the phase diagram indicate where phase transitions occur and the areas between them show the temperature and composition ranges where an individual phase is stable. Therefore phase diagrams can be used as a guide to determine what composition and temperature is needed to form a particular phase with a specific surfactant. For example to make a hexagonal phase liquid crystal template using $C_{16}EO_8$ in water the composition needs to be between 35 and 70 wt.% at a temperature between 20 °C and 60°C. As well as the lyotropic phases the phase diagram for $C_{16}EO_8$ also indicates a biphasic region at low surfactant concentrations and high temperature (W + L_1) where the micellar solution separates. The boundary that separates this phase and the micellar phase is called the cloud point since when observed under the POM the solution becomes cloudy as the W + L_1 phase is reached.

At high surfactant concentrations and lower temperatures no lyotropic liquid crystal phases are formed and the surfactant is insoluble. The line on the phase diagram that separates the lyotropic phases from the solid insoluble surfactant is known as the Krafft boundary.

1.3.3 Identification of lyotropic liquid crystal phases by polarising optical microscopy

Liquid crystals can have an optical property known as birefringence or anisotropy. In a birefringent material an incident light ray is split into two separate rays due to the presence of two different refractive indices 90° apart. Because of this they are able to change the plane of polarised light. A birefringent liquid crystal structure is formed when the micelles within it are arranged in a regular order in one or two spatial directions. In the hexagonal phase the micelles are arranged regularly in two directions and in the lamellar phase arranged regularly in one direction (in the direction of the bilayer sheets) therefore they are anisotropic. The cubic phase is non-birefringent as it has spatial order in three dimensions. Liquid crystal phases such as the hexagonal and lamellar can be identified by polarising optical microscopy (POM). POM uses an optical microscope using an un-polarised light source with two crossed polarised filters, one below (the polariser) and one above (the analyser) sample stage. Figure 1.8 shows a POM used for studying lyotropic liquid crystal phases.

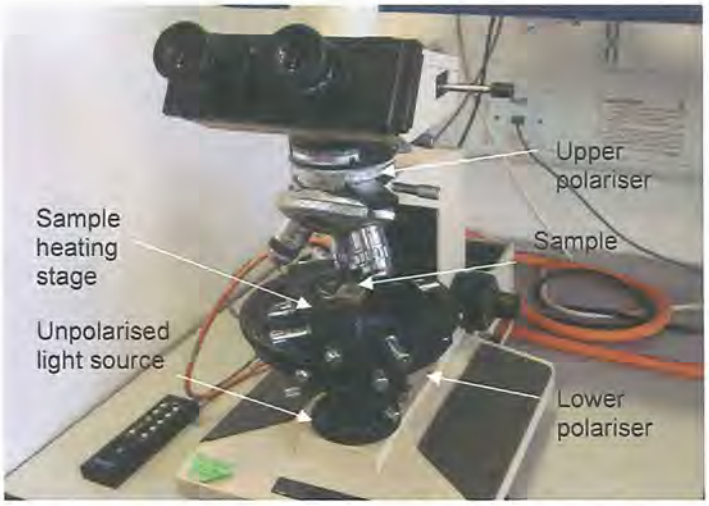

Fig. 1.8 Polarising optical microscope with heating stage

Each lyotropic liquid crystal phase has a specific optical texture when observed using the POM. Figures 1.9 to 1.13 show the optical textures typical of the hexagonal, cubic, lamellar and micellar phases of a liquid crystal mixture made using the surfactant $C_{16}EO_8$.

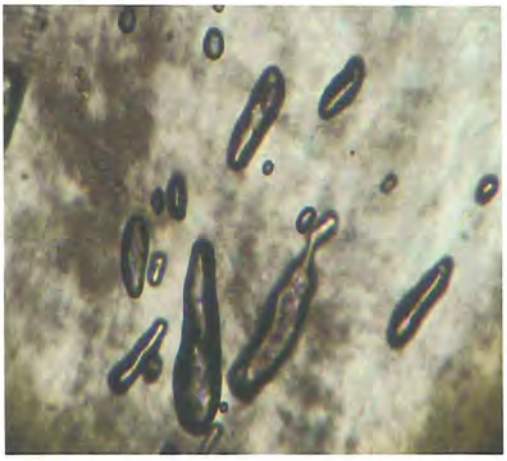

Fig. 1.9 Optical texture typical of the hexagonal phase of $C_{16}EO_8$ at approx. 25°C

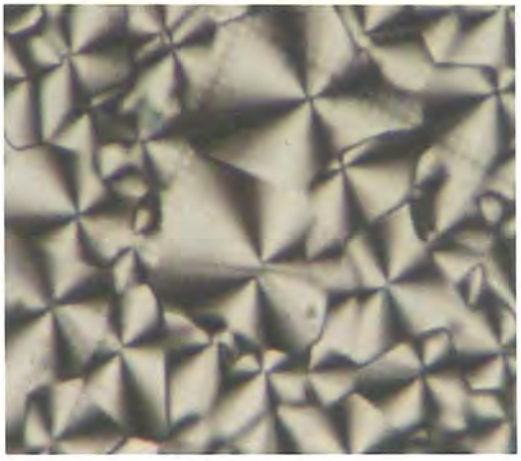

Fig. 1.10 Optical texture produced after heating above 65 °C and then cooling to reform the hexagonal phase of $C_{16}EO_8$

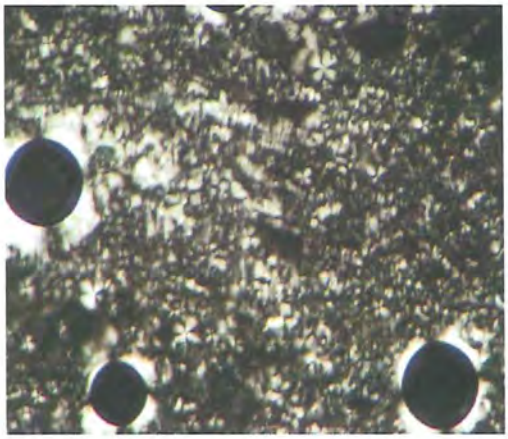

Fig. 1.11 Optical texture of the lamellar phase of $C_{16}EO_8$.

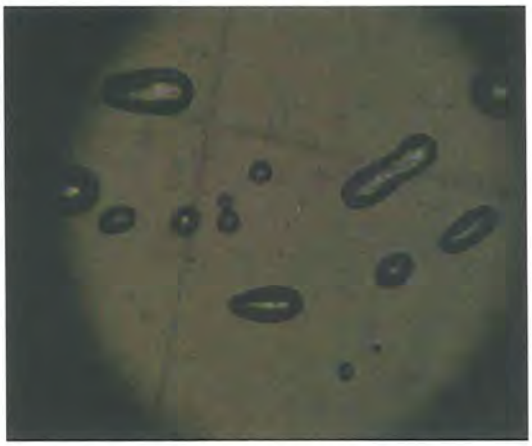

Fig. 1.12 Optical texture of the cubic phase of $C_{16}EO_8$.

Fig. 1.13 Optical texture of the micellar phase of $C_{16}EO_8$.

Figure 1.9 shows the typical optical texture of the hexagonal phase at ambient temperature it is often described as being "feathery". The irregular elongated bubbles are also a good indication of the hexagonal phase their shape is due to the high viscosity of the mixture. If the sample is heated beyond the temperature at which the hexagonal phase is stable, (for a liquid crystal of 50 wt.% $C_{16}EO_8$ this is around 65°C) and is then slowly cooled back to reform the hexagonal phase a cross or fan like texture is usually seen as shown in figure 1.10. This type of pattern is called a Schlieren brush effect. These brush patterns form around a central point defect in the liquid crystal structure generated during the reformation of the hexagonal phase. The cross pattern is formed because the polarisers are superimposed at 90° to each other. The dark brushes appear where the surfactant columns are aligned with one of the polarisers preventing light to pass, the light regions are where the surfactant columns are not aligned with the polarisers allowing light through. The brushes are wider further away from the point defect because there are more columns aligned with the polarisers [39,44]. Figure 1.14 overleaf illustrates the formation of the Schlieren cross effect seen with the hexagonal phase of lyotropic liquid crystals.

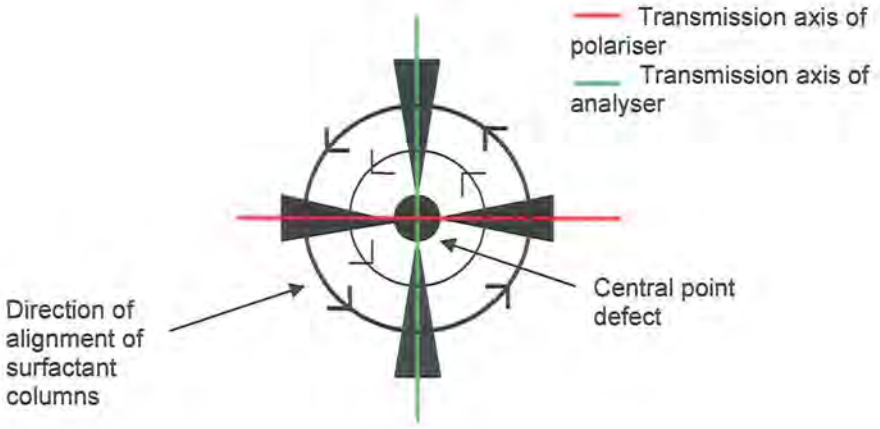

Fig. 1.14 A diagrammatic explanation of the Schlieren crossed-fan optical texture. Reproduced from reference 44

The lamellar phase produces an optical texture as seen in figure 1.12 often referred to as a "marble like" texture sometimes a sweeping streaky effect is apparent produced by the bilayer structure. Any bubbles that are present are spherical because of the low viscosity of this phase. The optical texture of the cubic phase is shown in figure 1.13. Because the cubic phase is non-birefringent no light is passed and the texture appears dark. The bubbles are similar in shape to those found in the hexagonal phase since the cubic phase is also viscous preventing them to adopt a less strained spherical form. Figure 1.14 shows the optical texture of the micellar phase. Like the cubic phase the micellar phase is also non-birefringent so it also appears dark. The micellar phase is distinguished from the cubic phase by the shape of the bubbles, this phase has very low viscosity so the bubbles are spherical.

As briefly noted earlier the liquid crystal phase can also be identified using small angle x-ray diffraction. From measuring the positions of the peaks and calculating the pore spacing (d-spacing) from Braggs law. The spacing ratio of each lattice plane can then be used to determine the liquid crystal phase. For example with the hexagonal phase of $C_{16}EO_8$ gives diffraction peaks for the (100), (110) and (200) crystal lattice planes. When mixed with water the spacing ratio of these peaks is $1:\sqrt{3}:2$. Addition of an electrolyte solution for electroplating mesoporous films will slightly alter the spacing ratios, but at low concentrations this effect is small. Table 1.3 overleaf lists some of the spacing ratios for the hexagonal, lamellar and cubic liquid crystal phases.

Table 1.3 Spacing ratios of diffraction peaks used to determine the crystal structure from small angle x-ray diffraction peaks. Taken from reference 31.

Liquid crystal phase	Lattice planes (hkl)	Spacing ratio
Hexagonal phase (H_1)	(100)	1
	(110)	$\sqrt{3}$
	(200)	2
	(210)	$\sqrt{7}$
Lamellar phase (L_α)	(100)	1
	(200)	2
	(300)	3
Cubic phase (V_1)	(110)	$\sqrt{2}$
	(200)	2
	(211)	$\sqrt{6}$
	(220)	$\sqrt{8}$

1.4 Mesoporous materials

This section will firstly introduce mesoporous materials and explain why they are of interest in research and industry. Then the history of their development will be presented including a review of the literature concerning the electrodeposition of mesoporous films. Finally the synthesis of mesoporous electrodeposited films using the liquid crystal templating method is given.

1.4.1 Introducing porous materials

a) Porosity

A porous material is defined as a material that has a high proportion of void space within its three dimensional bulk. The internal structure of a porous substance can be thought to be dominated by an extensive void-solid interface created by a network of channels running throughout the material. A good example of a highly porous material is a solid foam or sponge [45]. Porous materials have been classified by the

International Union of Pure and Applied Chemistry (IUPAC) on the basis of their pore size [46]. Table 1.4 shows the pore size classifications.

Table 1.4 IUPAC classification of porous materials by pore size
Taken from T. Gabriel, ref. 32

Pore Width	Pore Classification
>50 nm	Macropore
2 – 50 nm	Mesopore
1.4 – 2 nm	Supermicropore
0.5 -1.4 nm	Micropore
<0.5 nm	Ultramicropore

The pores within these materials can have either a random distribution or an ordered regular array depending upon how they are synthesised. The experimental work described in this thesis is concerned with mesoporous lead telluride films with a regular porous structure.

b) Mesoporous materials, their importance and applications

Because of its highly porous structure a mesoporous material has an extremely high internal surface area compared to the same non-mesoporous bulk material. For example mesoporous platinum powder has been produced with a specific surface area of 60 m^2 /g, whereas platinum black has only a specific surface area of 25 m^2 /g [47]. This increased effective surface area allows much more interaction for reactant species leading to greater catalytic activity. Mesoprous materials can exhibit enhanced magnetic, optical and electronic properties in comparison to non-mesoporous materials. For example nanostructured cobalt films were found to have greatly enhanced magnetic coercivity in comparison to bulk cobalt films, the observed magnetic characteristics increased with a larger pore size [48]. Mesoporous tin with a regular hexagonal array of pores has been synthesised [49] and investigated for lithium ion battery electrodes, they were shown to be more durable then the non-mesoporous electrodes. The mesoporous structure allowed expansion and contraction during ion insertion and removal with reduced structural damage and subsequently increased

battery life time [50]. They also appear to be very promising for applications in fuel cells and sensors. An added advantage of having the very high density of pores that exists in a mesoporous material is that less material is needed this would drastically reduce the cost when a metal like platinum is used [51,40]. It can be expected that mesoporous semiconducting materials will display enhanced optical properties since they are composed almost entirely of surface atoms leading to an increased efficiency of photo-generated charge carriers. However there is a probability that electrons promoted to the conduction band may become trapped by the surface atoms especially the partially positively charged lead atoms. This could counter any gain in efficiency produced by the increased surface area. These properties make the fabrication of mesoporous chalcogenide semiconductors especially compelling in the development of more efficient photovoltaic solar cells [52]. Due to the dimensions of the nanostructure quantum confinement effects may occur, where the charge carriers (electrons and electron-"holes") generated become trapped. This allows modification of the band gap energy in mesoporous semiconductors.

1.4.2 The development of mesoporous materials

a) The "Mobil method"

Mesoporous materials with a regular array of pores are a fairly recent innovation. The first report of an ordered mesoporous material was by Beck and associates [53] in 1992. They produced a series of materials called the Mobil Corporation Material Series (MCM-41S). These were produced by taking aluminosilicate gel and mixing with an alkyltrimethlyammonium surfactant at 150°C for 48 hours. During this time the surfactant forms cylindrical micelles in a hexagonal array with the polar head groups of the surfactant molecules on the outside, the silica gel forms around the polar surface of the surfactant cylinders. Removal of the surfactant by calcination produced a hexagonal mesoporous structure this material was called MCM-41. The pore size could be controlled by the length of the alkyl chain in the surfactant or adding a pore swelling agent like 1,3,5-trimethlybenzene [54]. The product formed however was amorphous and granular. Therefore this method is not suitable for the formation of thin films of metals or semiconductors. By increasing the amount of surfactant present they were able to create two other porous structure types. On increasing the amount of

surfactant a complex interconnected pore structure (cubic phase structure) was obtained, called MCM-48 and at highest surfactant concentrations a lamellar structure was formed, MCM-50 [55].

b) The "True Liquid Crystal Templating" (TLCT) method

The first direct templating procedure was reported by the Attard group [56]. They also produced mesoporous silica, but in contrast to the Mobil method a much higher concentration of surfactant, 50 wt.% was used. The Mobil method only uses up to 10 wt.% surfactant. The higher concentration of surfactant allows for better stability and control of the liquid crystal structure and therefore improves the porous structure of the final product. Another major advantage is that the pore morphology of the fabricated product can be predicted. The non-ionic surfactants octaethylene glycol monododecyl ether ($C_{12}EO_8$) and octaethylene glycol hexadecyl ether ($C_{16}EO_8$) were used to make the liquid crystal templates and tetramethyl-orthosilicate (TMOS) was used as the precursor. The silica material condenses in the aqueous domains of the surfactant liquid crystal phase, therefore the final mesoporous structure of the calcined silica is a cast of the liquid crystal phase. Transmission electron microscopy (TEM) and X-ray diffraction analysis showed that the prepared materials had a regular hexagonal mesoporous structure. The pores were regularly sized with a diameter of 28 Å separated with silica walls approximately 12 Å thick. The pore to pore distance was 39 Å and nitrogen absorption studies showed that the specific surface area was 1400 $m^2 g^{-1}$. Like the Mobil method they were also able to produce mesoporous silica with cubic and lamellar porous structures. Thin film preparations of mesoporous silica were also produced showing that this method could be employed to make mesoporous materials with regular dimensions rather than just amorphous granular products. Another major advantage to the direct liquid crystal templating method is that it is not limited to producing mesoporous inorganic oxides like the silicate materials just described, a wide range of materials can be synthesised using this technique including metals and semiconductors. This is because the formation of the liquid crystalline structure is not dependent on the interaction of the surfactant and the precursor material. Therefore the direct templating approach has opened up lots of exciting possibilities for making mesoporous materials. For example the Attard group synthesised mesoporous platinum using the TLCT method [57]. They obtained a coarse

granular material with a specific surface area between 17 and 23 $m^2 g^{-1}$. This kind of material could be used as a catalyst, however for applications such as sensors and electrochemical devices a thin film is required. A mesoporous platinum-ruthenium alloy was also prepared by the Attard group [58] using TLCT. TEM analysis of the fine powder showed a regular mesoporous structure and the specific surface area was found to be 86 $m^2 g^{-1}$. The following section will look at examples of mesoporous thin films that have been produced by electrodeposition using liquid crystal templating.

c) Electrodeposition of metallic mesoporous thin films using TLCT

After synthesising amorphous mesoporous platinum Attard *et al* went on to produce thin films of hexagonal phase mesoporous platinum (H_1-ePt) by electrodeposition from liquid crystal templates [59]. They used a ternary mixture consisting of 42 wt.% $C_{16}EO_8$ as the surfactant, 29 wt.% hexachloroplatinic acid and 29 wt.% deionised water as the templating mixture. Films were deposited onto polished gold electrodes at temperatures between 25°C and 65°C. The deposited films were uniform and shiny. TEM showed that a hexagonal mesoporous structure was present with a long range of order the pores had a diameter of 25 Å (+/- 1.5 Å), wall thickness was also 25 Å (+/- 1.5 Å). Pore size was adjusted by using a surfactant with a shorter hydrophobic tail (for smaller pores) or larger by adding a hydrophobic swelling agent in a similar manner to the Mobil method. The specific surface area was estimated to be 22 (+/- 2) $m^2 g^{-1}$ a bulk film deposited from the same conditions had a surface area of only 4.5 (+/- 0.5) $m^2 g^{-1}$. Elliott *et al* reported the preparation of hexagonal phase electrodeposited platinum (H_1-ePt) films with an extremely high surface area of 460 $m^2 g^{-1}$ using a similar procedure to that used by the Attard group [60]. They found that the temperature and deposition potential have a strong influence on the specific surface area morphology and nanostructure of the film. As briefly highlighted earlier mesoporous cobalt (H_1-eCo) has been produced by Bartlett and co-workers [48] and mesoporous tin by Whitehead [49,50] using the TLCT method. Because nickel is widely used as a material for battery electrodes and other electrochemical components mesoporous nickel was synthesised, the greater surface area was expected to enhance the performance of these devices [61]. Bartlett and Marwan report the electrodeposition of mesoporous hexagonal phase rhodium thin films (H_1-eRh) [62]. The specific surface area was calculated to be 32 $m^2 g^{-1}$. Bartlett *et al* have also prepared mesoporous

palladium thin films with a hexagonal pore structure (H_1-ePd) [63]. The surface area of the deposited H_1-ePd was much larger than that for H_1-eRh at 91 m^2g^{-1}. Mesoporous palladium films could potentially be used as sensors for methane gas detectors.

d) Electrodeposition of mesoporous semiconductor thin films by TLCT

The first mesoporous semiconductor films were fabricated by Attard *et al* [64] who fabricated hexagonal mesoporous selenium (H_1-eSe) films. They deposited onto evaporated gold on glass electrodes at -0.65 V *vs.* mercurous sulphate electrode (SMSE) using a templating mixture containing 50 wt.% $C_{16}EO_8$ and 50 wt.% of an acidified aqueous solution containing 10 mM selenium dioxide and 2 M sulphuric acid. TEM showed a regular hexagonal porous structure with a pore diameter of 25 Å +/- 2 Å. Nandhakumar and associates [65] then electrodeposited mesoporous tellurium films (H_1-eTe) onto evaporated gold on glass electrodes. They used a templating mixture containing 50 wt.% $C_{16}EO_8$ and 50 wt.% of an acidified aqueous solution containing 5 mM tellurium dioxide and 2 M sulphuric acid. Films were electrodeposited at a potential of -0.70 V *vs.* (SMSE). TEM micrographs of the film clearly showed a hexagonal array of pores with a diameter of 30 +/- 2 Å and a wall thickness at closest distance between pores of 28 +/- 2 Å. SAXD indicated a pore to pore distance of 66 Å which was in good agreement with the TEM measurements.

The synthesis of mesoporous thin films of tellurium and selenium encouraged the search for developing nanostructured chalcogenide thin films. Progressing from their work on mesoporous tellurium Nandhakumar *et al* electrodeposited mesoporous cadmium telluride thin films (H_1-eCdTe) [66]. They used a templating mixture consisting of 50 wt.% $C_{16}EO_8$ and 50 wt.% of a solution of 0.15 M cadmium sulphate and 5 mM tellurium dioxide dissolved in 2 M sulphuric acid. The films were deposited onto evaporated gold on glass electrodes at potentials between -0.54 and 0.65 V *vs.* SCE at room temperature, deposition duration was from five to 16 hours. TEM micrographs revealed a regular hexagonal arrangement of pores with an average pore to pore spacing of 70 +/- 2 Å. SAXD showed one diffraction peak for the (100) planes with a spacing of 69 +/- 1 Å, in good agreement with the TEM data. Wide angle X-ray diffraction indicated that the CdTe crystal structure was aligned along the (111) direction. The stoicheometry of the deposited film could be controlled by adjusting the deposition potential between -0.40 and -0.80 V *vs.* SCE.

References

1. G.P. Kothiyal, B. Ghosh, On conductivity of lead tellurides. *Prog. Cryst. Growth Charact.* **(1990)**, vol. 20, p.313

2. H. Saloniemi, T. Kanniainen, M. Ritala, M. Leskelä, *Thin Solid Films* (**1998**), 326, pp. 78-82

3. A. Mondal, N Mukherjee, S.K. Bhar, D. Banerjee. *Thin Solid Films*, **(2006)**, vol. 515, pp. 1255-1259

4. Y.A. Ivanova, D.K. Ivanou, E.A. Streltsov. *Electrochem. Commun.* **(2007)**, vol. 9, pp. 599-604

5. H. Saloniemi. Electrodeposition of PbS, PbSe and PbTe thin films. Academic dissertation, Department of Chemistry, University of Helsinki, **(2000)**, p. 11

6. L. Beaunier, H. Cachet, R. Cortes, M. Fromat. *J. of Electroanal. Chem.* (**2002**), vol. 552, pp. 215-218

7. R. C. Weast (ed. in chief). *CRC Handbook of Chemistry and Physics*, 66th edition, 1985-1986, Boca Raton. USA

8. Y. Yang, W. Li, L. Yu, X. Sun, L. Xu, L. Hou. *Infrared Phys. Tech.* **(1997)**, vol. 38, p. 9-12

9. C Boschetti, I. N. Bandeira, H. Closs, A.Y. Ueta, P.H.O. Rappl, P. Motisuke, E. Abramof. *Infrared Phys. Tech.* **(2001)**, vol. 42, p. 91-99

10. H Zogg, C Maissen, J. Masek, T. Hoshino, S. Blunier and A, N. Tiwari. *Semicond. Sci. Technol B.* **(1991)**, p. C36-C41.

11. H. Zogg, A. Fach, C. Maissen, J. Masek, S. Blunier. *Optical Engineering.* **(1994)**, 33(5), p. 1440-9.

12. S.N. Chesnokov, D.E. Dolzhenko, I.I. Ivanchik, D.R. Khoklov. *Infrared Phys. Tech.* **(1994)**, vol. 35, p. 23-31

13. P.K. Nair, M.T.S. Nair, *J. Phys. D: Appl. Phys.* **(1990),** vol. 23, p. 150-155.

14. Z.H. Dughaish. *Physica B*, **(2002),** vol. 322, p. 205–223

15. A. Lambrecht, R. Kurbel, M. Agne. *Mater. Sci. Eng. B.* **(1993)**, vol. 21, p.217

16. M. Tacke. *Infrared Phys. Tech.* **(1995)**, vol. 36, p. 447-463

17. R. Krska, R. Kellner, U. Schiessl, M. Tacke and A. Katzir, *Appl. Phys. Lett.* **(1993).** Vol. 63, p. 1868.

18. S.P. Zimin, M.N. Preobrazhensky, D.S. Zimin, R.F. Zaykina, G.A. Borzova, V.V. Naumov *Infrared Phys. and Tech.* **(1999)**, vol. 40, pp. 337-42

19. P.K. Parris, D. Mukherjee, C.A. Hogarth. *Physica Status Solidi A.* **(1995)**, vol. 152, p 461

20. N.I. Fainer, M.L. Kosinova, Yu.M. Rumyantsev, E.G. Salman, F.A. Kuznetsov. *Thin Solid Films.* **(1996)**, vol. 280, p. 16-19

21. S. Gorer, A. Albu-Yaron, G. Hodes. *Chem. Mater.* **(1995),** vol. 7, p. 1243-1256

22. F. Xiao B. Yoo, M.A. Ryan, K-H. Lee, N.V. Myung. *Electrochemica Acta,* **(2006)**, vol. 56, pp. 1101-1107

23. D.K. Ivanou, E.A. Streltsov, A.K. Fedotov, A.V. Mazanik, D. Fink, A. Petrov. *Thin Solid films*, **(2005)**, vol. 490, p. 154-160

24. C.R.B. Miranda, P.G. Abramov, F.C.L. de Melo, N.G. Ferreira, *Materials Res.* **(2004)**, vol. 7, p. 619-623

25. E.A. Streltsov, N.P. Osipovich, L.S. Ivashkevich, L.S. Lyakhov. *Electrochim. Acta,* **(1998)**, vol. 44, p. 407-413

26. L. Beaunier, H. Cachet, R. Cortes, M. Froment. *J. of Electroanal. Chem.* **(2002)**, vol. 552, pp. 215-2

27. E.A. Streltsov, N.P. Osipovich, L.S. Lyakhov. *Electrochim. Acta,* **(1999)**, vol. 44, p. 2645

28. S. Kumar, Z.H. Khan, M.A. Majeed-Khan, M. Husain. *Curr. Appl. Phys.* **(2005)**, vol. 5, pp. 561-566

29. F. Xiao, B Yoo, K.N. Bozhilov, K-H. Lee N.V. Myung, *J. Phys. Chem. C,* **(2007),** vol. 111, p. 11397-11402

30. I.S. Nandhakumar, X. Li, *Electrochem Commun.* **(2008)**, vol. 10, p. 363-366

31. T. Gabriel. PhD thesis, University of Southampton, **(2005)**, p. 41

32. M. P. R. Panicker, M. Knaster, F. A. Kroger, *J. Electrochem. Soc.* **(1978)**, vol. 125, p. 566-572

33. M.S. Martın-Gonzalez, A.L. Prieto, R. Gronsky, T. Sands, A.M. Stacy. *J. Electrochem. Soc.* **(2002)**, vol. 149, p. C546-C554

34. J.G.N Matias, J.F. Juliao, D.M. Soares, A. Gorenstein *J. Electroanal. Chem.* **(1997)**, vol. 431, pp. 163-169

35. F.A. Kröger. *J. Electrochem. Soc.* **(1978)**, vol. 125(12), pp.2028-2034

36. D.R. Lide (ed. in chief), *The CRC Handbook of Chemistry and Physics* **(2003-04)**, 84th edn. P. 5-24. Boca Raton

37. D. Lincot, Electrodeposition of semiconductors. *Thin Solid Films*. **(2005)**, vol. 487, pp 40-48

38. I. Dierking. Textures of liquid crystals. **(2003)**, p. 2. Wiley-VCH

39. P.J. Collings, M. Hird, Introduction to liquid crystals, **(2004)**, Chapt. 7, Taylor and Francis London.

40. S.A.A. Leclerc, Ph.D. Thesis, University of Southampton, **2000**

41. S. Guerin, PhD thesis, University of Southampton School of Chemistry, **(1999)**

42. Website reference:
http://search.live.com/images/results.aspx?q=surfactant+phase+diagrams&mkt=en-gb
19th June 2008-06-19

43. D.J. Mitchell, G.J.T. Tiddy, L. Waring, T. Bostock, M.P. McDonald. *J. Chem. Soc. Faraday Trans. I.* **(1983)**, vol. 79, p. 975-1000

44. M.L. Markham, Ph.D. thesis, University of Southampton, School of Physics and Astronomy **(2006)**

45. S. Polarz, B. Smarslya, *J. Nanoscience and Nanotechnology*, **(2002)**, vol. 6, p. 581-612

46. J. Rouquerol, D. Avnir, C.W. Fairbridge, D.H. Everett, J.H. Haynes, *Pure and Applied Chemistry*, **(1994)**, vol. 66(8), pp. 1739 -1758

47. J.R. Owen, G.S. Attard, P.N. Bartlett *et al. Chem. Mater.* **(1999)**, vol. 11, pp. 3602-3609

48. P.N. Bartlett, P.N. Birkin, M.A. Ghanem, P. de Groot, M.S Pawick. *J. Electrochem. Soc.* **(2001)**, vol. 148, p. C119-123

49. A.H. Whitehead, J.M. Elliot, J.R. Owen, G.S. Attard. *Chem. Comm.* **(1999)**, pp. 331-2

50. A.H. Whitehead, J.M. Elliot, J.R. Owen, *J. of Power Sources* **(1999)**, vol. 81. pp. 33-38

51. J.M. Elliot, J.R. Owen, G.S. Attard, P.N. Bartlett, N. Ryan, G. Singh. *J. Of New Materials for Electrochemical Systems*. **(1999)**, vol. 2, p. 239-241

52. I.S. Nandhakumar, T. Gabriel, X. Li, G.S. Attard, M. Markham, D.S. Smith, J.J. Baumberg, *Chem. Commun.* **(2004)**, pp 1374-1375

53. C.T. Kresge, M.E. Leonowicz, W.J. Roth, J.C. Vartuli, J.S. Beck. *Nature*, (**1992**), 359, pp. 710-12

54. N. Ulagappan, C. N. R. Rao, *Chem. Commun.*, **(1996)**, vol. 24 p. 2759-27

55. J.C. Vartuli, K.D. Schmitt, C.T. Kres, W. J. Roth, M.E. Leonowicz, E. W. Sheppard, S.B. McCullen, S.D. Hellring, J. S. Beck, J. L. Schlenker, D. H. Olson. *Chem. Mater.* **(1994)**, vol. 6, p. 2317-2326

56. G.S. Attard, J.C. Glyde, C.G. Goltner, *Nature*, (**1995**), 378, pp. 366-8

57. G.S. Attard, J.M. Corker, C.G. Goltner, S. Henke, R.H. Templer. *Angew. Chem. Intl. Edn. Eng.* **(1997)**, vol. 36, p. 1315

58. G.S. Attard, S.A.A Leclerc, S. Maniguet, A.E. Russell, I.S. Nandhakumar, B.R Gollas, P.N. Bartlett. *Microporous and Mesoporous Materials*. **(2001)**, vol. 44-45, p. 159-163.

59. G.S. Attard, P.N. Bartlett, N.R.B. Coleman, J.M. Elliot, J.R. Owen, J.H. Wang *Science*, (**1997**), 278, pp. 838-840

60. J.M. Elliot, G.S. Attard, P.N. Bartlett, N.R.B. Coleman, D.A.S. Merckel, J.R. Owen. *Chem Mater.* **(1999)**, vol. 11, p. 3602-3609

61. P.A. Nelson, J.M. Elliott, G.S. Attard, J.R. Owen. *Chem. Mater.* **(2002),** vol. 14, p. 524-529

62. P.N. Bartlett, J. Marwan, *Microporous and Mesoporous Materials.* **(2003),** vol. 62 p. 73–79

63. P.N Bartlett, B. Gollas, S. Guerin, J. Marwan. *Phys. Chem. Chem. Phys.* **(2002)**, vol. 4, p. 3835-3842

64. I.S. Nandhakumar, J.M. Elliott, G.S. Attard. *Chem. Mater.* **(2001),** vol. 13, p. 3840-3842

65. T. Gabriel, I.S. Nandhakumar, G.S. Attard. *Electrochem. Commun.* **(2002)**, vol. 4, p. 610-612

66. I.S. Nandhakumar, T. Gabriel, X. Li G.S. Attard, M. Markham, D.S. Smith J.J. Baumberg, *Chem. Commun.* **(2004)**, pp 1374-1375

Chapter 2

Experimental procedures

2 Experimental Procedures

2.1 Solutions used for cyclic voltammetry and PbTe film deposition

All solutions were made using purified water from a Purite Select Fusion 160 (Ondeo) purification system, resistivity 18.20 Ω cm. Glassware was cleaned by soaking overnight in a 3% Decon 90 solution and then rinsed in purified water. Individual solutions of nitric acid alone, lead acetate/nitrate in nitric acid, and tellurium dioxide in nitric acid and the actual electroplating solution containing all three of the deposition compounds were prepared. This was to investigate the electrochemistry of each component and the actual electroplating solution, concentrations are given in appropriate sections and figure captions. Lead acetate (Alfa Aesar), tellurium dioxide (Aldrich), nitric acid (Fisher Scientific, UK) and lead nitrate (Puratronic, Alfa Aesar) were all used as received to make these solutions. To aid dissolution of tellurium dioxide in solutions, heating and stirring on a hotplate was used.

2.2 Pre-treatment of gold and silicon substrate wafers

Throughout this work silicon wafers, n-type, (100) lattice orientation, phosphorous doped, double sided polish with resistivity of 1 -10 Ω cm (IDB technologies Ltd. UK) were used. Gold on glass substrates were prepared by evaporating approximately 15 nm of chromium then approximately 270 nm of gold (99.99%, Agar UK) onto 1 mm thick glass microscope slides The chromium allows better adhesion of the gold layer.

2.2.1 Silicon wafer preparation

To produce a grease and contaminant free substrate surface, silicon wafers were firstly sonicated in isopropyl alcohol (Fisher Scientific, UK) for 30 minutes. Then placed in either a hot solution of two volumes of 30% H_2O_2 (BDH, UK) one volume concentrated HCl (Fisher Scientific, UK) and eight volumes of purified water at 80°C for 15 minutes or ca. 56% v/v concentrated HNO_3 in water at 80°C for 30 seconds. After that the wafer was etched either in hydrofluoric acid or ammonium fluoride (concentration and duration of etching given in results/discussion) to remove the

oxide layer on the surface of the wafer. This procedure was followed for all wafers used for cyclic voltammetry (CV) work and film depositions. After drying in a stream of argon the wafer was mounted onto a piece of glass slide, the wafer being a few millimetres longer than the glass to give a projecting edge for electrical connection to the potentiostat. Polyimide tape was used to fix the wafer to the glass slide, covering the edges of the wafer to prevent "edge effects" the exposed electrode surface area was then measured so current densities could be calculated. If polyimide tape was not available then varnish was applied.

2.2.2 Gold substrate preparation

Pre-treatment of gold-on-glass substrates was more straightforward. As for silicon wafers they were cleaned by sonicating in IPA for 30 minutes to remove any grease or organic contamination. A cadmium connecting strip was fixed to one end of the gold substrate using silver conducting paint. After drying for five to ten minutes polyimide tape was used to mask the edges of the substrate.

2.3 Cyclic voltammetry studies of bulk solutions

Cyclic voltammetry was performed using a Pyrex water jacketed cell and a standard three electrode system. The working electrode was a either a silicon substrate or a gold on glass substrate. The counter electrode was a platinum wire gauze and the reference electrode was a home made saturated calomel electrode (SCE, +0.244 V *vs.* standard hydrogen electrode), the homemade SCE was calibrated against a commercial SCE. All potentials are reported with respect to the SCE. Figure 2.1 shows a schematic of the cell set up and figure 2.2 is a photo of the cell set up. Although not indicated in the diagram a Teflon lid was used to cover the cell to prevent evaporation and possible contamination of the solution. The lid had holes cut into it to allow insertion of the electrodes. The cell was connected up to a μautolab type II potentiostat/galvanostat, (Eco Chemie, Netherlands). Control of the potentiostat was by the General Purpose Electrochemical System (GPES) software. To improve electrical contact between the silicon wafer and the connecting clip, gallium indium eutectic (Aldrich) was applied to the silicon surface. For experiments using a gold substrate this was not required. Sweep rates and electrode areas are given

in the appropriate sections and figure captions. All CV experiments were performed without stirring.

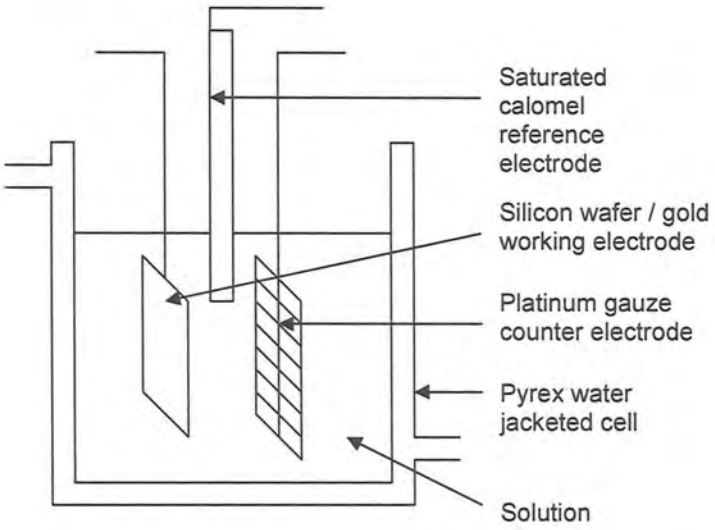

Fig. 2.1 Schematic of experimental set up of cell for CV work and bulk film deposition

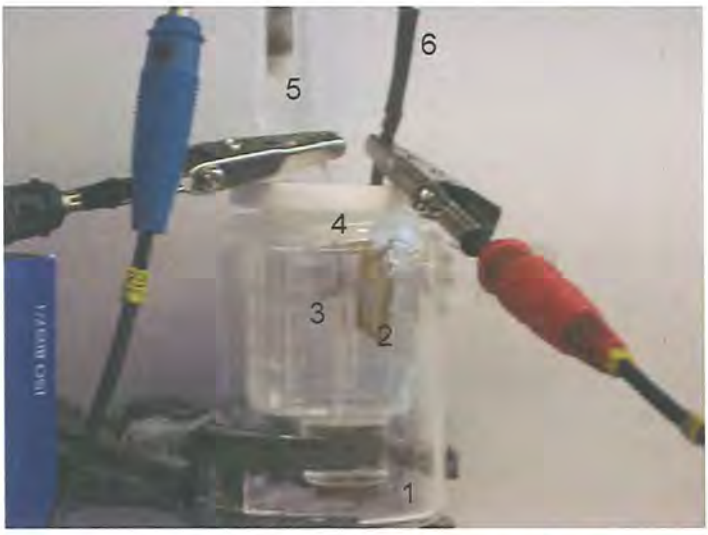

Fig. 2.2 Cell set up for CV and bulk film deposition on gold.
1. Water jacketed glass cell, 2. Gold substrate, 3. Platinum counter electrode
4. Teflon lid, 5. Calomel reference electrode, 6. Cadmium connecting strip to gold substrate

2.4 Bulk film deposition

Bulk films of lead telluride were deposited using a potentiostatic regime. A potentiostatic deposition uses a reference electrode as well as the substrate (working electrode) and counter electrode. During a potentiostatic deposition the potential is kept constant between the substrate and reference electrode and the current that is passed is measured between the substrate and the counter electrode. Potentiostatic deposition is more frequently used to deposit films as the composition can be easily controlled. In the work described in this thesis all the films were deposited cathodically using the potentiostatic method. Figure 2.3 shows a schematic diagram for the potentiostatic cell set up, WE is the working electrode, RE is the reference electrode and CE is the counter electrode.

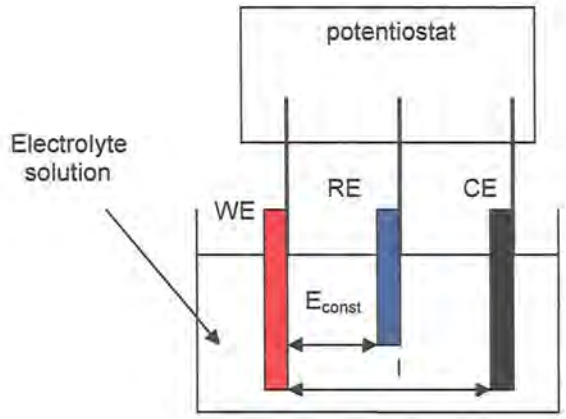

Fig. 2.3 Cell set up for a potentiostatic deposition

Film deposition was performed by chronoamperometry. This method sets the working electrode (the gold or silicon substrate) at a fixed potential versus the reference electrode using the GPES-potentiostat system. The electrodeposition is then run for a predetermined duration, the current that is passed is recorded as a function of elapsed time. Choice of deposition potential was done by analysis of the CV produced from the solution. Deposition was performed either with or without stirring of the solution. Duration of deposition was between five minutes and two hours (exact times given in appropriate sections). Film thickness was controlled by the amount of charge passed.

After deposition the tape was carefully removed and the film area was measured so the charge density (C cm^{-2}) for the deposition could be calculated.

2.5 Mesoporous film deposition

Templating mixtures for the electrodeposition of mesoporous films are composed of the surfactant $C_{16}EO_8$ and a solution containing salt(s) of the element(s) that make up the film being deposited. For example for the deposition of a hexagonal mesoporous PbTe film using $C_{16}EO_8$, a 50 wt.% mixture of $C_{16}EO_8$ and an aqueous solution containing a lead salt such as lead acetate and tellurium dioxide is prepared. POM was used to check that the hexagonal phase was present. The templating mixture is then placed onto the substrate which acts as the cathode during deposition. Since the ionic species can only reside in the aqueous domains of the liquid crystal and not in the hexagonally arranged surfactant cylinders, the film is electrodeposited around the surfactant. Once the deposition is complete the liquid crystal template mixture is removed by soaking in a solvent this leaves behind the mesoporous structure. Figure 2.4 shows a schematic of the liquid crystal templating process.

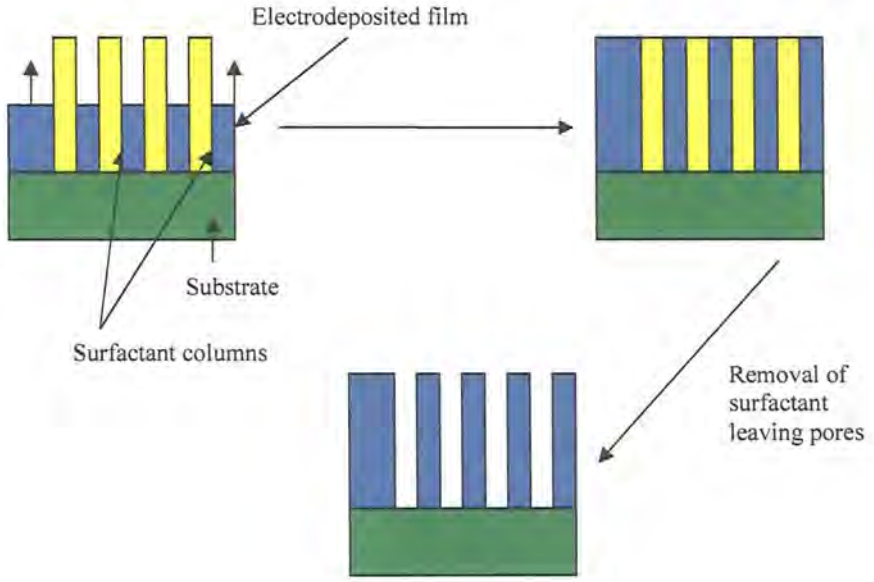

Fig 2.4 Schematic of the deposition of a mesoporous film using the liquid crystal templating process

2.5.1 Preparation of liquid crystal template mixture

For all mesoporous films deposited a 50 wt% liquid crystal template mixture was prepared by weighing equal amounts of the surfactant octaethylene glycol monohexadecyl ether, $C_{16}EO_8$ (Nikko Co., Japan) and electrolyte containing nitric acid, lead acetate (or lead nitrate) and tellurium dioxide into a small glass vial, (actual concentrations used in the electrolyte are given in the appropriate sections and figure captions). A magnetic stirrer bead was added and the vial was then capped and placed in a water bath and heated to 70°C. Once the mixture had melted it was stirred at this temperature for up to 30 minutes to allow through mixing. Then the hot plate was turned off and the mixture was allowed to cool slowly to room temperature. The mixture was left to homogenise for a minimum of one hour before use.

2.5.2 Liquid crystal phase structure determination

Before carrying out deposition the phase of the liquid crystal template mixture was verified, usually to determine that the hexagonal phase was present. This was done by using polarised optical microscopy, POM. To examine and identify the liquid crystal phase behaviour of a liquid crystal templating mixture a small amount of the mixture is sandwiched between a piece of microscope slide and a glass cover slip. This is then placed upon a heating stage, (Linkam TMS90) and the temperature is gradually increased and maintained to within +/- 0.1°C. The different phases that may form with increasing temperature can be identified by observing the optical textures using the POM (Olympus BH2). The phase transition boundary is reached when the optical texture changes, the temperature at which this occurs can be recorded for construction of the phase diagram of the templating mixture. At the phase transition boundary between the hexagonal and micellar phases light was no longer able to pass the crossed polarised filters at this point the temperature was recorded. The temperature was then reduced gradually, whereupon a fan-like optical texture was seen indicating that the hexagonal phase was present.

2.5.3 Construction of the phase diagram of $C_{16}EO_8$ and electrolyte solution

To investigate the phase behaviour of the $C_{16}EO_8$ / electrolyte mixture used for deposition of mesoporous films of PbTe a phase diagram was constructed. Small quantities (<0.2g) of mixtures containing $C_{16}EO_8$ mixed with an electrolyte solution containing 50 mM $Pb(Ac)_2$, 1 mM TeO_2, 0.15 M HNO_3 were prepared by the method outlined in section 2.5.1. The preparations ranged from containing 5% to 95% w/w $C_{16}EO_8$. Each preparation was examined using POM as described in the previous section to investigate its phase behaviour and the temperature at which phase boundary(s) were observed was recorded. By plotting the phase transition points for each composition tested a phase diagram was produced.

2.5.4 Preparation of the cell for mesoporous deposition

After treating the wafer as described in 2.2 it was taped to a small piece of glass slide in the same way as for bulk film deposition leaving an exposed area of silicon. A vitton seal was then placed on top and the liquid crystal template applied and firmly packed into the seal on top on the exposed silicon surface. Then a platinum wire gauze counter electrode was placed onto the liquid crystal mixture. This gauze had a hole in the middle of it to allow insertion of the reference electrode into the liquid crystal mixture. A thin coating of template mixture was then applied to the gauze. A piece of glass slide with a hole in its centre was then placed with its hole aligned with the hole in the gauze. Finally the cell assembly was wrapped with insulating tape to prevent drying of the template mixture which would lead to possible loss of the hexagonal phase and reduced diffusion of the ionic species. Figure 2.5 is a schematic of the cell assembly and figure 2.6 shows the actual components of a cell used for deposition onto gold on glass substrate.

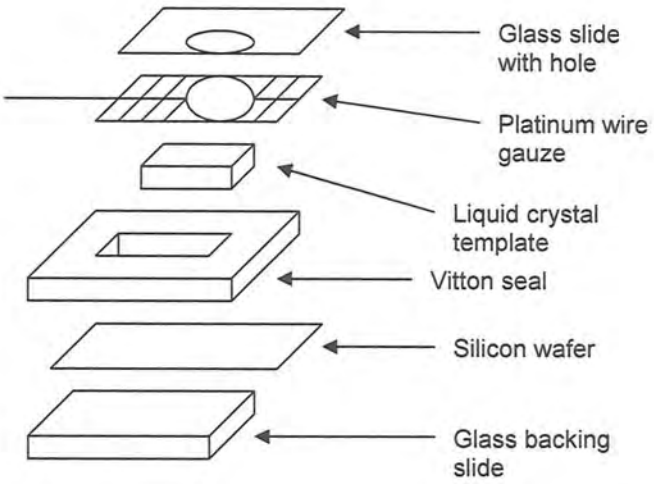

Fig. 2.5 Schematic diagram showing the cell assembly for mesoporous deposition

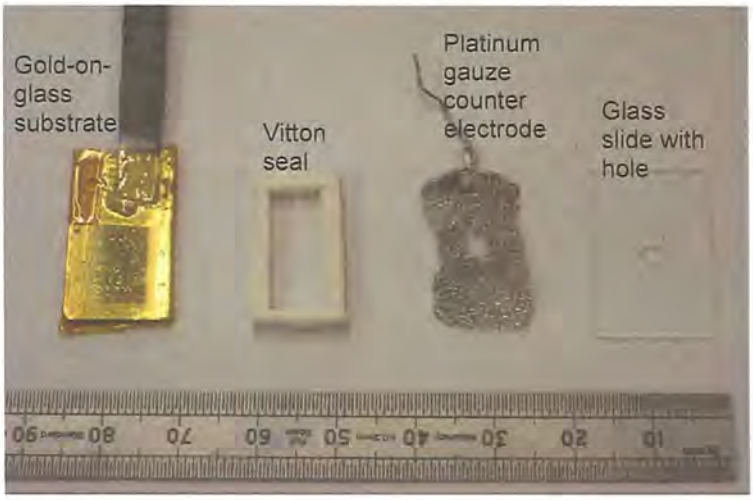

Fig 2.6 Components of a cell used for deposition of a mesoporous film onto a gold-on-glass substrate. Ruler scale is in millimetres.

After wrapping the cell gallium indium eutectic was applied to the end of the silicon wafer. The reference electrode was inserted carefully into the liquid crystal template and the counter, reference and silicon wafer working electrode connected to the potentiostat. Figure 2.7 shows the set up for deposition of mesoporous PbTe onto gold.

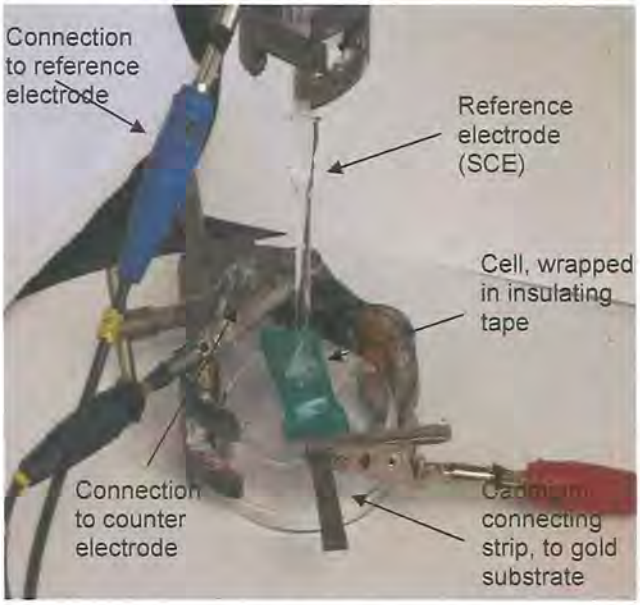

Fig. 2.7 Photo showing the actual set up for deposition of a mesoporous film onto gold

Electrodeposition was performed in the same way as bulk film formation by chronoamperometry at a constant potential. After deposition the cell was carefully unwrapped and taken apart. The tape covering the edges of the wafer was gently peeled off. Then the wafer and deposited film was soaked in isopropyl alcohol for several hours to remove any liquid crystal template mixture before subsequent film analysis. The film area was measured to calculate the charge density of the deposition.

2.6 Deposition of lead telluride films using double pulse deposition

Nucleation pulse electrodeposition or more accurately double pulse electrodeposition is a method where two distinct potential pulses are applied to the cell. This method was introduced by Sheludko and Todorova [1]. The first pulse, the *nucleation pulse* is very short at most only a few seconds in duration. The potential of this pulse has to be sufficiently negative for nucleation to occur, exceeding the critical nucleation potential. The second pulse, or the *growth pulse* is of lower potential where the nucleation sites expand in size and coalesce to form the film. Ideally nucleation should only occur during the nucleation pulse and film growth only occurring during the growth pulse. By controlling the pulse duration and potential a homogeneous nucleation site size and distribution can be achieved. Generally a large negative potential and short pulse duration produce this situation [2,3]. Figure 2.8 shows a

schematic of the double pulse technique. E_1 and E_2 are nucleation and growth potentials and t_1 and t_2 are the durations of the nucleation and growth pulses. E_{crit} is the critical potential for nucleation to occur.

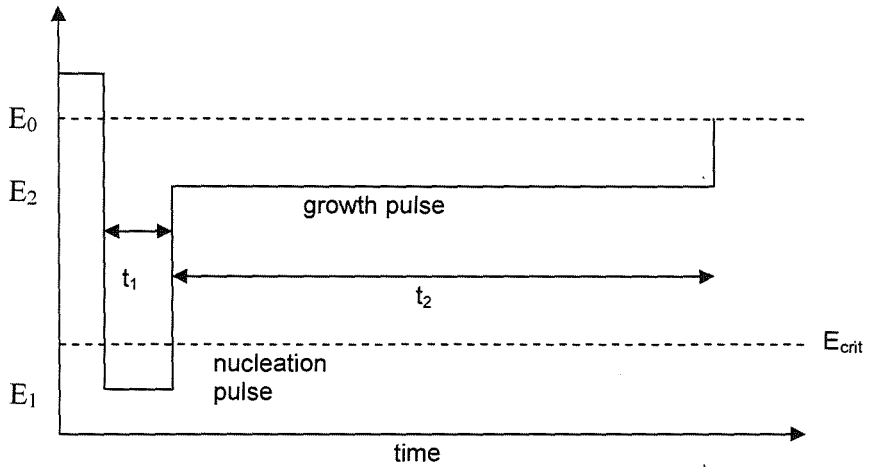

Fig. 2.8 Schematic representation of the double-pulse nucleation method, taken from reference 2

2.7 Characterisation of electrodeposited films and templating mixtures

After depositing mesoporous and bulk films scanning electron microscopy, energy dispersive X-ray analysis, wide and small angle X-ray diffraction, infra-red adsorption spectroscopy and atomic force microscopy were used to investigate film morphology, composition, structure and band gap energy.

2.7.1 Scanning Electron Microscopy of deposited films

To obtain information about film surface morphology scanning electron microscopy (SEM) was performed using a Phillips XL30 ESEM electron microscope. The silicon wafer with the deposited film was stuck onto an aluminium stub. For films deposited onto gold on glass substrates a small piece of carbon tape was applied between the edge of the gold substrate and the stub to prevent charging of the substrate and subsequently a poor SEM image. An accelerating potential of between 10 – 30 kV (usually 10 kV) was used with a secondary electron detector to image the film surface. The sample stage could be tilted from 0° to about 70° when film thickness measurements were needed.

2.7.2 Energy Dispersive X-Ray Scattering analysis

To determine film composition and stoicheometry energy dispersive x-ray scattering was undertaken using the Phillips XL30 ESEM electron microscope which was equipped with an EDXS detector. When the electron beam strikes the film, ground state valance electrons in the atoms composing the film are raised into higher energy electron orbitals or completely ejected. This leaves electron holes in the low energy valance orbitals which are filled by electrons migrating from higher energy orbitals. When these electrons fall back to fill the vacancies left behind they release the excess energy as an X-ray, whose energy is dependent on the energy difference between the two orbitals. This allows quantitative elemental analysis as different elements have unique X-ray emissions. An accelerating potential of 10 – 12 kV was used for a duration of 100 seconds. Usually several measurements (approximately ten) of the same film were performed at different locations to obtain an average film composition.

2.7.3 Transmission electron microscopy of mesoporous films

To obtain direct evidence of a mesoporous structure in a film transmission electron microscopy (TEM) was used. TEM is similar to SEM, the sample is placed on a specimen stage inside the microscope chamber and the system is evacuated. The main difference between SEM and TEM is that with TEM the image is produced by the electrons transmitted by the sample whereas in SEM the image is produced by secondary electrons emitted from the sample. An electron beam is generated by an electron gun and electrons are accelerated by a potential of up to 300 kV so they can pass through the sample. However care has to be taken on using very high accelerating potentials as this can cause heating of the specimen and possible damage of the nanostructure. The beam is focused onto the specimen by a series of electromagnetic lenses (condensers). The image of the specimen is produced from the transmitted electrons (electrons that have passed through the sample). Magnification of the transmitted image is done by an objective and projector lens [4,5]. The image is formed and observed on a fluorescent screen and can be recorded with a camera. Figure 2.9 shows a schematic of a typical transmission electron microscope.

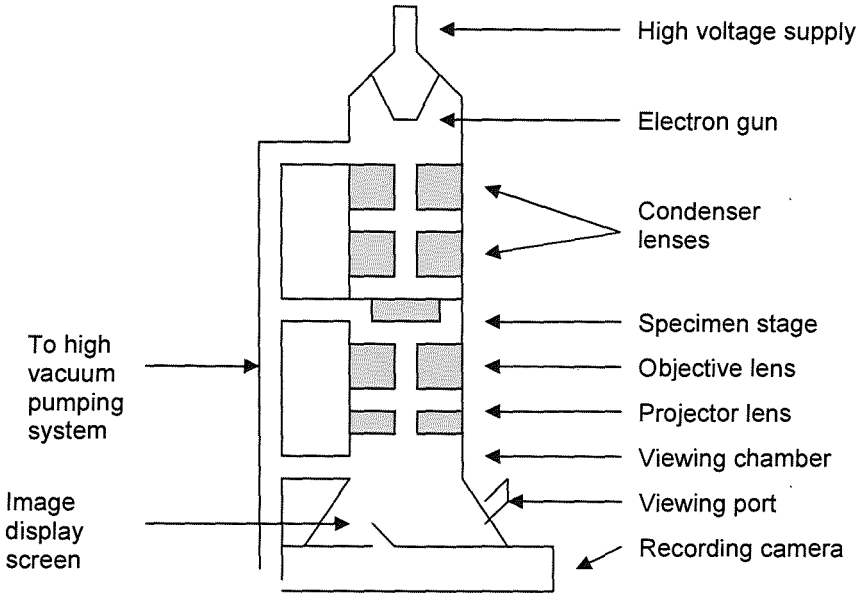

Fig. 2.9 Schematic of a typical transmission electron microscope, taken from refs. 4 and 5

Specimens were prepared by carefully scraping off the deposited film from the substrate and placing it in water. The sample was broken down by sonication to create a suspension of film particles. A drop of the suspension was placed onto a circular carbon coated copper TEM grid (Agar Scientific, UK) and then allowed to dry under ambient conditions. To ensure complete drying they were then placed overnight in a dessicator. Images were obtained using a JEOL 2000FX transmission electron microscope.

2.7.4 X- Ray Diffraction analysis of deposited films

X-ray diffraction was used to determine the crystal structure of deposited films (wide angle X-ray diffraction WAXD) and for the analysis of mesoporous structure and liquid crystal template mixture phase (small angle X-ray diffraction SAXD). The diffraction pattern is produced by constructive interference of X-rays diffracted by the lattice planes of the material. This is indicative of the crystal structure and material being analysed. The lattice plane spacings of a crystal can be calculated from the X-ray diffraction angles in the pattern using the Bragg law, equation 2.1.

$$n\lambda = 2d.\sin\theta \qquad (2.1)$$

n is the order of the diffraction peak, λ is the X-ray wavelength, d is the lattice plane spacing and θ is the diffraction angle between the incident and the diffracted beams. In a mesoporous material the regular porous structure also produces a diffraction pattern, Braggs law can therefore be used to determine the pore spacing. By using equation 2.2 the inter-pore repeat distance in mesoporous films can be calculated.

$$D = d_{100} / \cos 30 \qquad (2.2)$$

Here D is the pore to pore repeat distance and d_{100} is the lattice spacing for the (100) planes of the hexagonal phase. This relationship is derived assuming that the pores are arranged in a uniform hexagonal array, each pore being at a corner of a triangle as illustrated in figure 2.10 below.

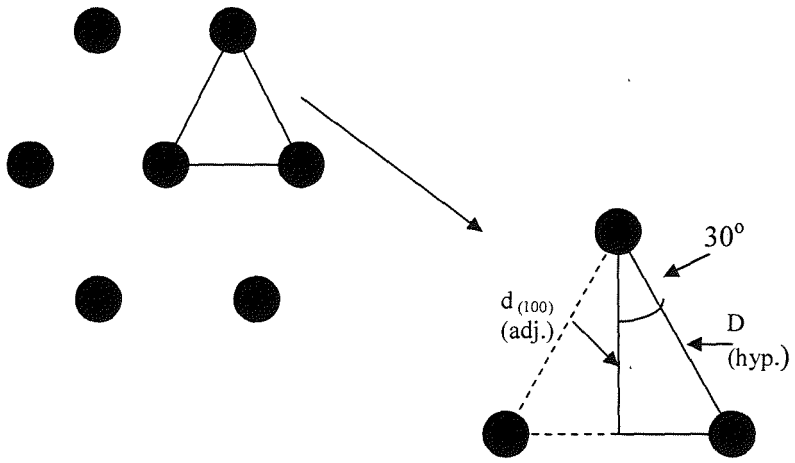

Fig. 2.10 Schematic illustrating the hexagonal phase structure and how the interpore distance, D is calculated

As shown in the diagram the interpore spacing, D can be found by trigonometry, by knowing the lattice spacing, $d_{(100)}$ which is the adjacent (adj.) of triangle, D forming the hypotenuse (hyp.). Now cosθ = adjacent / hypotenuse, or cos.30 = $d_{(100)}$ / D. Rearranging gives $D = d_{100} / \cos 30$. All diffraction analysis were performed using a powder diffractometer, (Siemens D5000) with CuK_α radiation, λ = 1.5406 Å. The sample (silicon wafer with deposited film) was mounted onto a plastic holder with a piece of bluetak and was adjusted until it was flat and level with the rim of the holder,

this was then placed inside the diffractometer. Figure 2.11 is a schematic of the diffractometer.

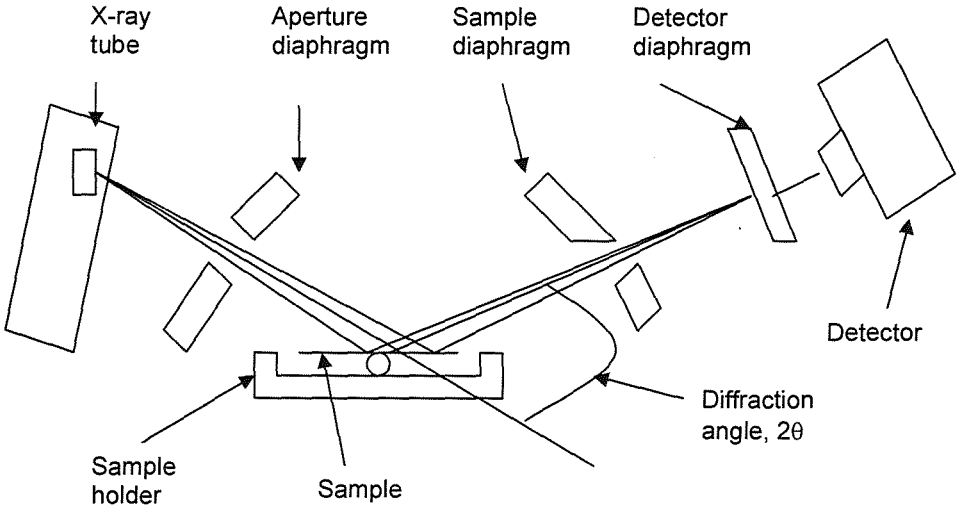

Figure 2.11 Schematic diagram of the Siemens D5000 powder diffractometer

The average crystallite size of the deposited material can be calculated using the Sherrer equation [6];

$$L = 0.9\lambda \times 180 / \pi B.\cos\theta \qquad (2.3)$$

Here L is the crystallite size, λ is the X-ray wavelength, θ is the angle of diffraction for the largest peak and B is the width at half maximum of the largest peak in degrees. For analysis of liquid crystal template mixtures a small amount of the mixture was spread in the shallow recess of a powder sample holder and made flat and even by scraping with a glass slide. For wide angle X-ray diffraction a 2θ range of 10 to 80° was used with a scan speed of 12° per minute. For rough analysis sampling time was usually about 30-40 minutes, more accurate and clearer diffractograms were run overnight. Small angle diffractions were run over a 2θ range of 1 to 4° with a scan speed of 4° per minute, sampling time was up to one hour.

2.7.5 Measurement of the band gap energy of deposited films

Semiconductor compounds such as lead telluride and elements including tellurium have specific band gap energies which can be used as a means of identification. The band gap energy is the amount of energy that has to be adsorbed by the semiconductor material for valence electrons to be promoted to the conduction band energy level. For lead telluride this is 0.33 eV [7], which is equivalent to infra-red radiation of 3.75 μm or 2660 cm^{-1}. Therefore infra-red absorption spectroscopy can be used to measure the band gap energy of, and characterise deposited lead telluride films. Infra-red spectra were run on a Jasco 620 FTIR spectrometer using a mercury-cadmium telluride detector. The detector required cooling with liquid nitrogen for it to function. Spectra were obtained in the absorbance mode. Then a plot of the absorption coefficient (α) against wavelength is produced, figure 2.12 shows an example of such a plot. The next step is to convert the wavelength axis into energy expressed as electron volts (eV). This is done by using the relationship:

$$E = hc / \lambda \qquad (2.3)$$

Where E is energy in eV, h is the Planck's constant, c speed of light and λ the wavelength. Expressing h as 4.136×10^{-15} eV.s and c as 3×10^{14} μm/s gives;

$$E = 4.136 \times 10^{-15} \times 3 \times 10^{14} / \lambda \quad \text{or,} \quad E = 1.24 / \lambda \qquad (2.4)$$

Therefore to convert wavelength into eV equation 2.4 is used finally (absorption coefficient x eV)^2 is calculated. Then the energy (eV) data points obtained are plotted against $(\alpha h\nu)^2$, (absorption coefficient x eV)^2, this gives a plot as shown (if data is correct) in figure 2.13. Extrapolation of the linear part of the plot to the energy axis gives the band gap energy of the material.

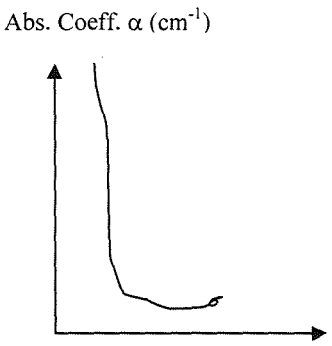

Fig. 2.12 Plot of absorbance coefficient *vs.* wavelength. Adapted from ref. 7

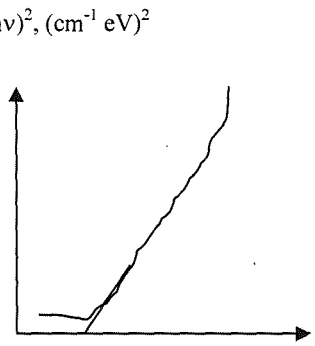

Fig. 2.13 Plot of $(\alpha h\nu)^2$ vs. energy Extrapolation of linear section gives the band gap energy. Adapted from ref. 7

2.7.6 Imaging of surfaces using atomic force microscopy

Atomic force microscopy was used to study the surface detail of silicon substrates and deposited mesoporous films. The main advantage of AFM is that unlike transmission electron microscopy (TEM) the film does not have to be scrapped off and placed on a TEM grid therefore the film is not damaged and can be reused, also no time consuming sample preparation is needed [8]. AFM is a scanning probe microscopy technique where a cantilever probe is scanned across the surface of the material being analysed. The movement of the sample is controlled by an xyz-piezoelectric stage. The deflection of the probe caused by inter-atomic forces of attraction and repulsion (Van der Waals) forces is measured by a laser reflecting off the cantilever onto a photodetector. This generates a signal which is used to produce an image of the surface, this is shown in figure 2.14. The force applied to the probe is kept constant by a feedback loop between the sample stage and the light lever detector. A Multimode Nanoscope III, (Digital Instruments, U.S.A.) AFM using tapping mode with a silicon cantilever/tip (Pointprobe, Nanoworld Technologies) linked to a PC running Nanoscope III software package was used to image films. Figure 2.15 shows a photograph of the Nanoscope III AFM. To image a surface the sample is placed onto the sample stage, then the cantilever-probe is carefully inserted into the cantilever holder and the holder locked into position. The laser is then aligned onto the back of the cantilever, this is done by bringing into focus the reflection of the cantilever

surface. This is done by adjusting the objective lens of the optical microscope and sample stage. Once in focus the laser spot is placed on the cantilever and its position on the photodetector is centred using the laser positioning controls. Tapping mode was then selected, where the cantilever is made to oscillate at its resonant frequency whilst scanning the surface. This helps to reduce stress on the tip and the sample as the tip is only in direct contact with the surface for a brief duration. The cantilever was tuned to its resonant frequency using the auto-tuning facility on the controlling software. After making final positioning adjustments of the sample and cantilever the tip was brought into contact with the sample. During imaging optimisation of the feedback controls and scan rate can be done to improve analysis of the film surface and image quality.

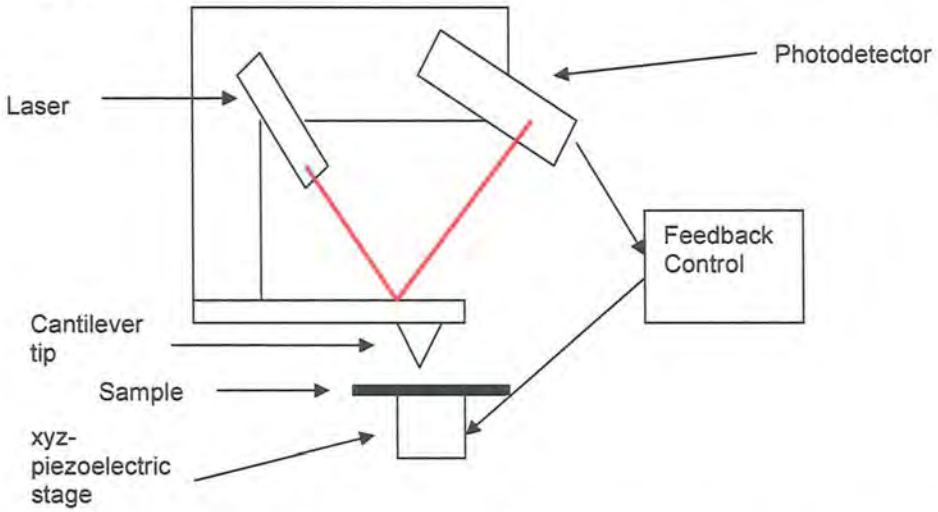

Fig. 2.14 schematic of a typical AFM illustrating the "light lever" detector and feedback control loop. Adapted from reference 9.

Fig. 2.15 Photo of the Nanoscope III AFM
Taken from reference 10

References

1. A. Sheludko, M. Todorova. *Bull. Acad. Bulg. Sci. Phys.* **(1952)**, vol. 3, p. 61

2. M. Ueda, H. Dietz, A. Anders, H. Kneppe, A. Meixner, W. Plieth. *Electrochim. Acta.* **(2002)**, vol. 48, p 377-386

3. G. Sandmann, H. Dietz, W. Plieth. *J. Electroanal. Chem.* **(2000)**, vol. 491, p. 78-86

4. S.A.A. Leclerc, Ph.D. Thesis, University of Southampton, **2000** p. 260

5. T. Gabriel. PhD thesis, University of Southampton, **(2005)**, p. 36

6. M.L. Markham, Ph.D. thests, University of Southampton, **(2006)**, p 33

7. S. Kumar, Z.H. Khan, M.A. Majeed-Khan, M. Husain. *Curr. Appl. Phys.* **(2005)**, vol. 5, pp. 561-566

8. I.S. Nandhakumar, T.J. Gordon-Smith, G.S. Attard, D.C. Smith. *Small*, **(2005)**, vol. 1 (4), pp. 406-408

9. Website reference: http://www.pacificnanotech.com/afm-tutorial_afm-theory.html, 6th Aug. 2007

10. Website reference: http://people.sabanciuniv.edu/~sonmez/labsd/labsd6.htm, 6th Aug. 2007

Chapter 3

Deposition of bulk lead telluride onto gold and silicon

3. Deposition of bulk lead telluride onto gold and silicon

To understand the electrochemistry of the deposition of lead telluride onto gold and silicon substrates a series of cyclic voltammetry experiments was undertaken. Then to investigate the feasibility of depositing lead telluride onto gold and silicon substrates bulk films were deposited. This chapter will firstly investigate the electrochemistry of lead telluride electrodeposition followed by studying bulk (non-mesoporous) lead telluride onto gold substrates. Then the electrochemistry and deposition of bulk lead telluride films onto silicon is examined. Investigation of double pulse deposition of bulk films onto gold and silicon will conclude the chapter.

3.1 Investigation of the electrochemistry PbTe deposition on gold

The electrochemistry of lead telluride deposition onto gold on glass substrates was investigated using cyclic voltammetry. A procedure based upon that used by Ivanova *et al* [1] who were studying lead telluride electrodeposition onto silicon was used. This examines each component of the electrolyte solution separately. First the behaviour of the nitric acid solution alone is investigated, then a solution of lead acetate with nitric acid followed by tellurium dioxide with nitric acid are studied. Finally a solution containing all three components is analysed. Gold substrates were cleaned by sonicating in IPA for 30 minutes before use. The solutions used were 1.5 M nitric acid, 10 mM tellurium dioxide and 500 mM lead acetate. Solutions were not stirred during the CV experiments and a fresh gold on glass substrate was used for each experiment. The sweep rate was set at 20 mV s^{-1} for all experiments performed. The cyclic voltammograms produced are shown in figures 3.1 to 3.4.

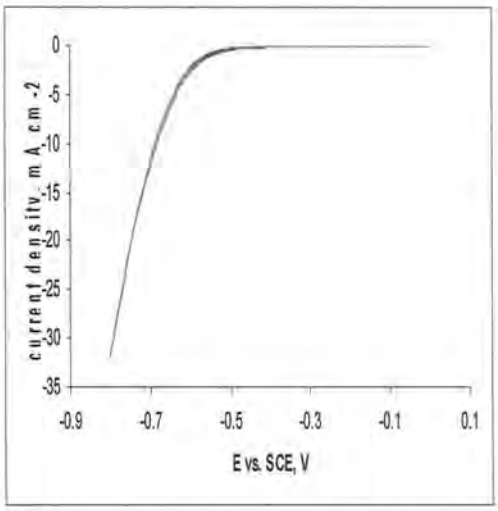

Fig. 3.1 CV of gold substrate in 1.5 M HNO_3 Sweep rate, 20 mV/s electrode area 1.20 cm^2

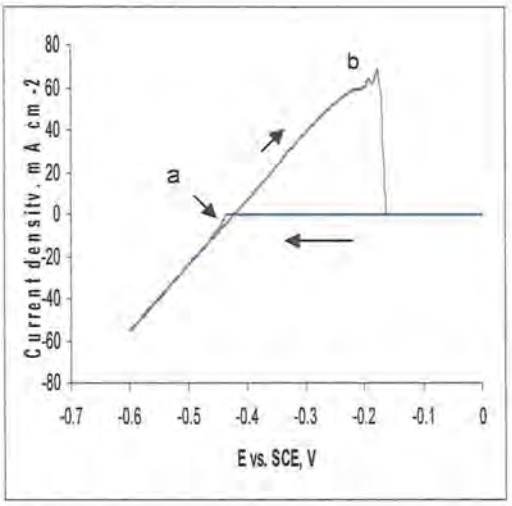

Fig 3.2 CV of gold substrate in 500 mM $Pb(Ac)_2$ 1.5 M HNO_3 Sweep rate, 20 mV/s, electrode area 1.17 cm^2 Direction of scan is shown by arrows.

CV for gold in nitric acid alone (figure 3.1) shows a cathodic current from about -0.5 V *vs.* SCE. This is from the reduction of H^+ to hydrogen, in fact at around this potential bubbles were observed forming on the surface of the gold substrate. No other electrochemical processes are indicated by the CV. Figure 4.2 is the CV for a gold substrate in a solution of 1.5 M nitric acid and 500 mM lead acetate. On the cathodic sweep no current is seen until a potential of about -0.43 V *vs.* SCE is reached where the current increases sharply at point "a". This is due to reduction of lead onto the gold substrate surface. At this point the exposed gold surface became darker as lead was deposited. At more negative potentials hydrogen evolution occurred. On the anodic scan a small nucleation loop is produced between -0.45 and -0.41 V *vs.* SCE. This is from the reduction of Pb^{2+} onto lead already deposited onto gold surface. A large stripping peak (b) is present arising from the oxidation of the deposited lead. A maximum current density of 67 mA cm^{-2} is reached at about -0.18 V *vs.* SCE then the current density suddenly drops off. No other electrochemical process were then observed.

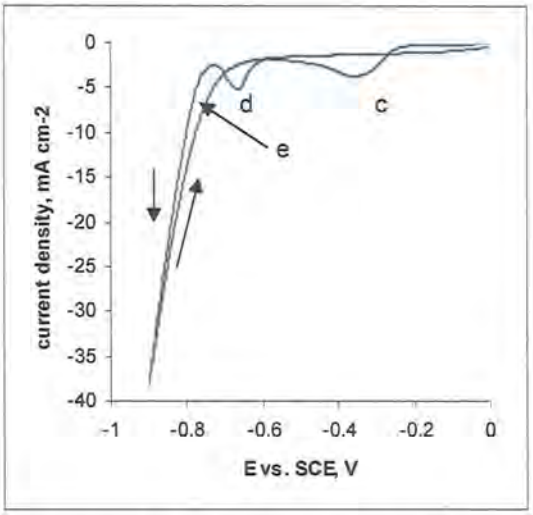

Fig. 3.3 CV of gold substrate in 10 mM TeO_2, 1.5 M HNO_3. Sweep rate 20 mV/s, electrode area 1.28 cm^2 Direction of scan is indicated by arrows.

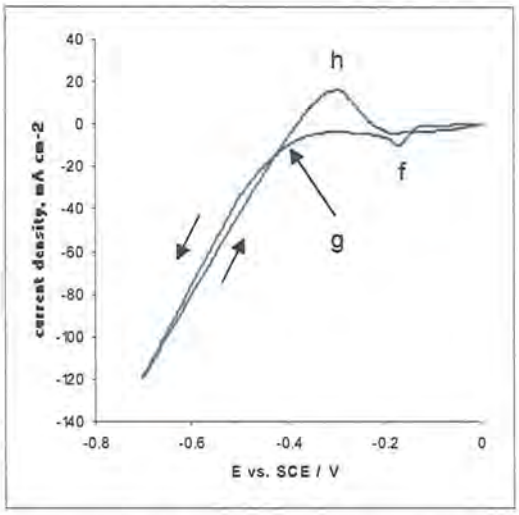

Fig. 3.4 CV of gold substrate in 10 mM TeO_2 500 mM $Pb(Ac)_2$, 1.5 M HNO_3. Sweep rate 20 mV/s, electrode area 0.63 cm^2. Direction of scan indicated by arrows.

The CV for a gold substrate in 10 mM tellurium dioxide 1.5 M nitric acid is shown in figure 3.3. On the cathodic scan two reduction waves are present. The first wave, labelled "c" with a maximum current density of -3.6 mA cm^{-2} at -0.35 V *vs.* SCE can be attributed to the direct four electron reduction of telluryl ions to tellurium on the gold substrate surface as proposed by Panicker *et al* [2]. At around -0.67 V *vs.* SCE a second reduction wave with a maximum current density of -5 mA cm^{-2} is seen, wave "d". This is probably due to the two step reduction of telluryl ions to elemental tellurium with formation of H_2Te as an intermediate species. At potentials greater than -0.75 V *vs.* SCE the current density sharply increases from the reduction of H^+ to hydrogen. On the anodic scan the trace crosses over the cathodic scan to form a nucleation loop at -0.69 V, point "e", this is due to further deposition of tellurium onto tellurium already deposited on the substrate surface. No other electrochemical reactions are indicated on the CV.

The CV of a gold substrate in a solution containing all three compounds that is used for deposition of lead telluride films is shown in figure 3.4. On the cathodic scan a reduction wave is observed starting at around -0.12 V *vs.* SCE with a current density maximum of -9.9 mA cm^{-2} at -0.17 V, wave "f". Then the current density plateaus off to about -4 mA cm^{-2} until -0.35 V *vs.* SCE where the current density starts to increase again due to reduction of lead and hydrogen evolution. Myung *et al* observed

reduction waves at a similar potential and attributed this to the co-reduction of lead and tellurium [4,5]. This CV demonstrates the underpotential deposition of lead to form lead telluride. The increase of current density due to tellurium deposition starts to occur at -0.12 V *vs.* SCE with a current density of -3.4 mA cm^{-2}. At this potential on the CV for deposition of tellurium alone the current density is only -0.9 mA cm^{-2}. The current density then reaches a maximum of -9.9 mA cm^{-2} at -0.17 V *vs.* SCE, on the CV for deposition of tellurium alone at this potential the current density is only about 0.2 mA cm^{-2}. The current observed on the CV for deposition of lead alone was only about 0.07 mA cm^{-2}. Therefore this increased current density is probably from the co-deposition of lead with tellurium to form lead telluride. From the CV of lead deposition on its own deposition did not occur until a potential of -0.43 V *vs.* SCE. This shows that the deposition potential of lead has been shifted positively by approximately 0.31 V, (taking the start of lead co-deposition to be around -0.12 V *vs.* SCE). This is not far from the potential shift theoretically calculated previously in equation 1.9. The anodic trace crosses over the cathodic trace at -0.42 V *vs.* SCE creating a nucleation loop, point "g". This arises from the deposition of lead ions onto lead that has already been deposited on the substrate. Then between -0.40 and -0.20 V a stripping peak "h" is observed arising from the oxidation of deposited lead. The size and current density associated with this stripping peak is much smaller compared to the stripping peak for the CV of lead on its own. This is because less lead is being oxidised as is it chemically bound to tellurium making it harder for it to go back into solution [6].

3.2 Deposition of bulk PbTe onto gold, investigating the effects of deposition potential on film composition and morphology

A series of bulk lead telluride films deposited onto gold on glass substrates was produced to investigate the effect of deposition potential upon film composition and morphology. Films were deposited using a solution containing 50 mM $Pb(Ac)_2$, 1 mM TeO_2 and 0.1 M nitric acid with a deposition duration of one hour at room temperature. The solution was not stirred during deposition. Films were characterised using SEM, EDXS and wide angle XRD. Figure 3.5 shows the film composition data obtained by EDXS as a plot of mean at.% lead against deposition potential. The upper and lower 95% confidence limits of the mean are indicated.

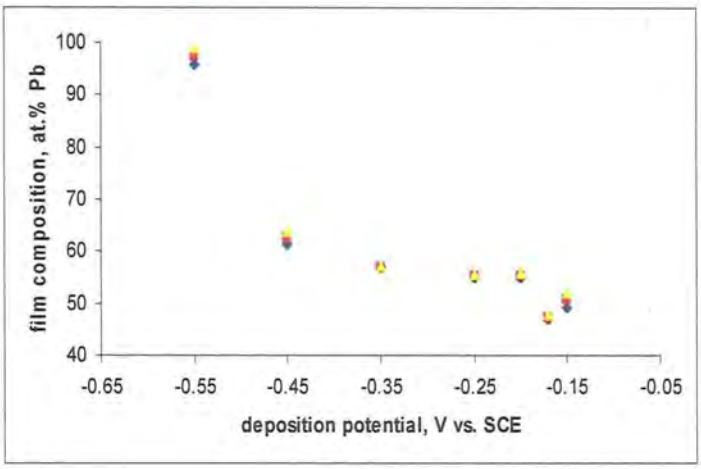

Fig. 3.5 Graph showing the mean composition of the deposited films as a function of the deposition potential. The upper and lower 95% confidence limits are indicated by the triangles and diamonds.

Almost stoicheometric films are deposited at potentials from -0.15 V to -0.20 V *vs.* SCE. This agrees with the CV for deposition of PbTe, figure 4.4 which suggests that PbTe is deposited in this potential range. At more negative potentials the proportion of lead that is deposited starts to increase. From between -0.20 V and -0.35 V the composition is stable at about 56 at.% lead. Then the proportion of lead increases, at -0.45 V it is about 63 at.% then at -0.55 V the film is almost entirely lead. Again this agrees with the CV for deposition of PbTe, at this potential deposition of lead was indicated by the large increase if current density. Saloniemi *et al* also found that there was a potential range over which lead telluride films were of a constant composition when deposited onto copper and tin oxide substrates [7]. Figures 3.6 to 3.11 are the SEM micrographs of the bulk films that were deposited.

Fig. 3.6 SEM micrograph of the film deposited At -0.17 V *vs.* SCE. Scale bar is 10 µm

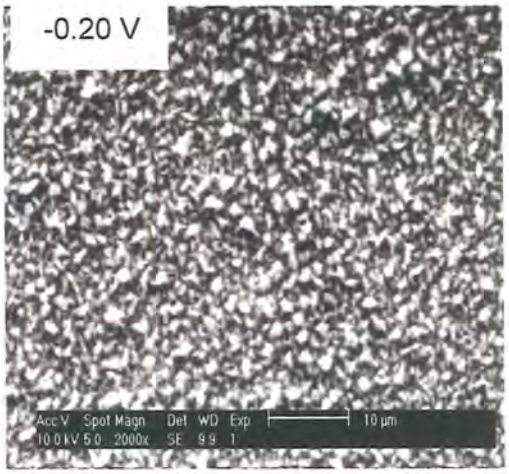

Fig. 3.7 SEM micrograph of the film deposited at -0.20 V *vs.* SCE. Scale bar is 10 µm

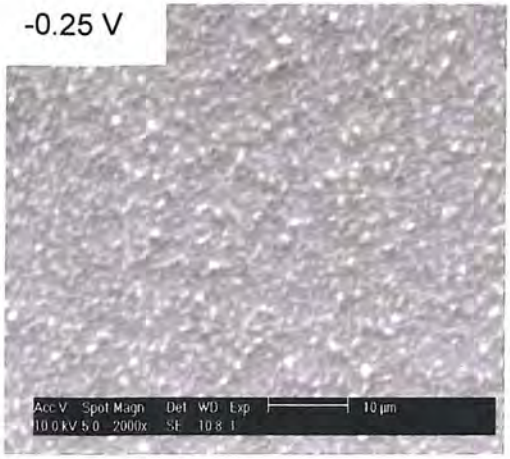

Fig. 3.8 SEM micrograph of the film deposited At -0.25 V *vs.* SCE. Scale bar is 10 µm

Fig. 3.9 SEM micrograph of the film deposited at -0.35 V *vs.* SCE. Scale bar is 10 µm

Fig. 3.10 SEM micrograph of the film deposited at -0.45 V *vs.* SCE. Scale bar is 100 µm

Fig. 3.11 SEM micrograph of the film deposited at -0.55 V *vs.* SCE. Scale bar is 500 µm

The films deposited at -0.15, -0.20, -0.25 and -0.35 V *vs.* SCE have the same morphology with grains of up to 1 µm in size. At more negative potentials the film morphology changes dramatically as bulk lead starts to be deposited. The film deposited at -0.45 V had much larger particles possibly consisting of lead and the film deposited at -0.55 V had a very rough surface with large flakes which according to the EDXS analysis would be mostly composed of lead. The very rough surface morphology could be due to hydrogen evolution which was observed during the deposition. Hydrogen bubble formation on the substrate surface would lead to uneven exposure of the substrate to the solution producing inhomogeneous film growth. Wide angle x-ray diffractograms of the films are shown in figures 3.12 to 3.17.

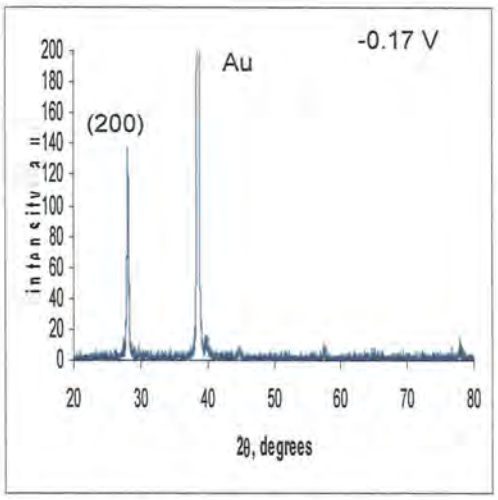

Fig. 3.12 Wide angle XRD of the film deposited 0.17 V.

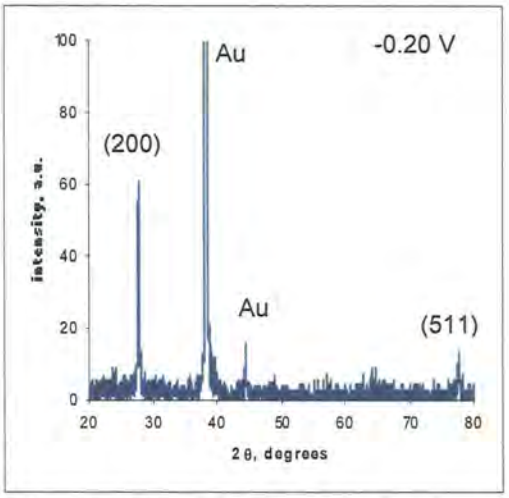

Fig. 3.13 Wide angle XRD of the film deposited at -0.20 V.

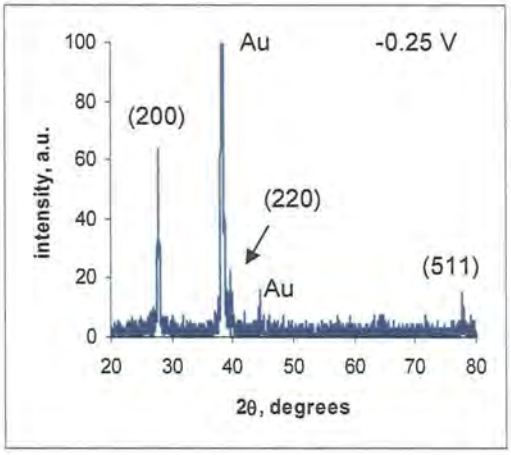

Fig. 3.14 Wide angle XRD of the film deposited at -0.25 V.

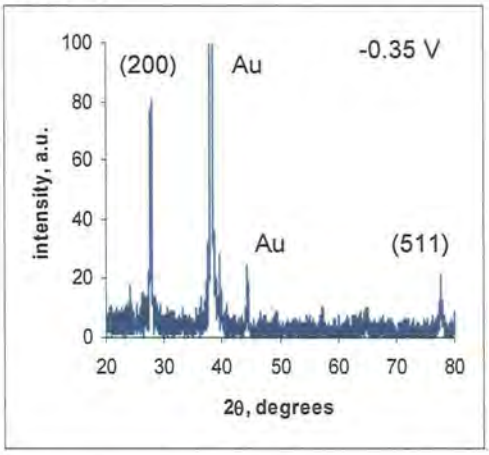

Fig. 3.15 Wide angle XRD of the film deposited at -0.35 V

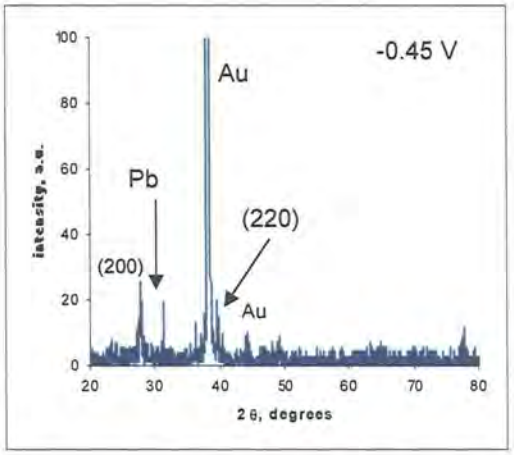

Fig. 3.16 Wide angle XRD of the film deposited at -0.45 V.

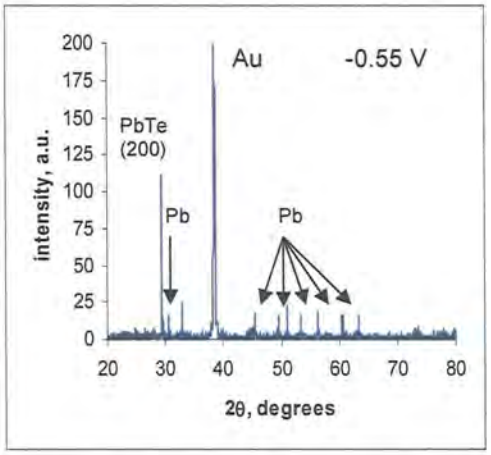

Fig. 3.17 Wide angle XRD of the film deposited at -0.55 V.

The XRD for the film deposited at -0.17 V shows a peak at 28.08° (2θ) corresponding to the (200) lattice planes of PbTe, this is the principle direction of film growth. No other diffraction peaks due to lead telluride are present. At -0.20 V a diffraction peak for the (200) planes is also present there is also a peak at 77.82° (2θ) this is probably from the (511) lattice planes. The diffractograms for the films deposited at -0.25 and -0.35 V are much the same. Again peaks are seen for the (200) and (511) planes for lead telluride. Also a peak is present for the (220) planes at 39.70° (2θ) although this is not very clear. At -0.45 V some changes in the diffractogram are seen. The diffraction peaks for the (200) and (220) lattice planes are almost the same height whereas before the (200) peak was much larger. This suggests that the (200) direction for film growth is less favoured. At around 31.2° (2θ) there is another peak not seen before. This is probably from bulk lead that has been deposited with PbTe, the (111) lattice planes of lead give a diffraction peak at this angle. For the film deposited at -0.55 V the diffractogram looks somewhat different. There is a peak at 29.38° (2θ) which is probably from the small amount of PbTe that was deposited. The other diffraction peaks are most likely from bulk metallic lead, this being inferred from the EDXS measurements of the film indicating that the mean composition was approximately 97 at.% lead. For comparison the wide angle XRD of a sample of commercial lead telluride (99.998% Sigma Aldrich, UK) is shown below, figure 3.18. The multiple sharp peaks indicate a polycrystalline material with a variety of crystal lattice directions. In agreement with the deposited films the principle lattice planes are the (200). The peak positions are close to the standard values for lead telluride given by the JCPDS diffraction studies database, as shown in table 3.1.

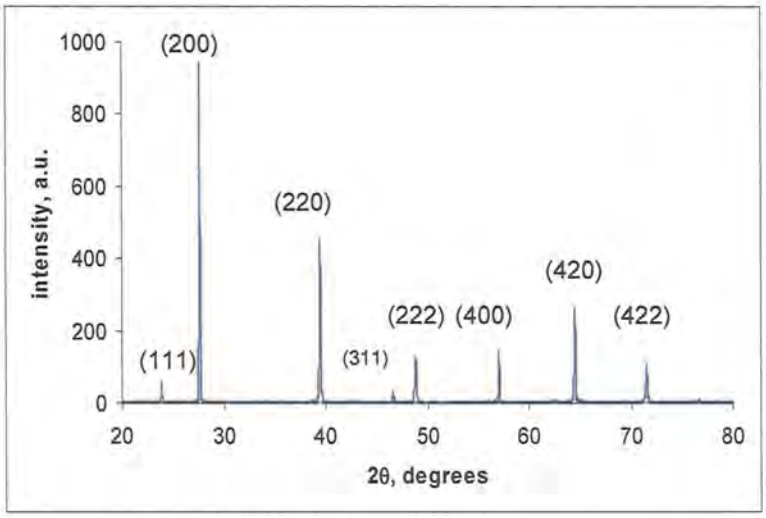

Fig. 3.18 Wide angle X-ray diffractogram of the high purity commercial lead telluride sample

Table 3.1 Comparison of the peak positions from the wide angle x-ray diffractogram of the commercial lead telluride powder with the JCPDS standard database values.

Lattice plane, (hkl)	(111)	(200)	(220)	(311)	(222)	(400)	(420)	(422)
Sample peak position, 2θ	23.88	27.64	39.44	46.68	48.86	57.04	64.52	71.56
JCPDS database value, 2θ	23.86	27.62	39.46	46.64	48.84	57.03	64.52	72.56

3.3 Investigation of the electrochemistry of PbTe deposition onto silicon

The electrochemistry of lead telluride deposition onto silicon was also investigated using cyclic voltammetry. The procedure was the same as that used in the previous chapter for deposition onto gold. The same solutions at the same concentrations were used and the solution was not stirred during the experiment. For each experiment a fresh piece of silicon substrate was used. The sweep rate for each CV experiment was set at 20 mV s^{-1}. Figures 3.19 to 3.22 show the voltammograms produced.

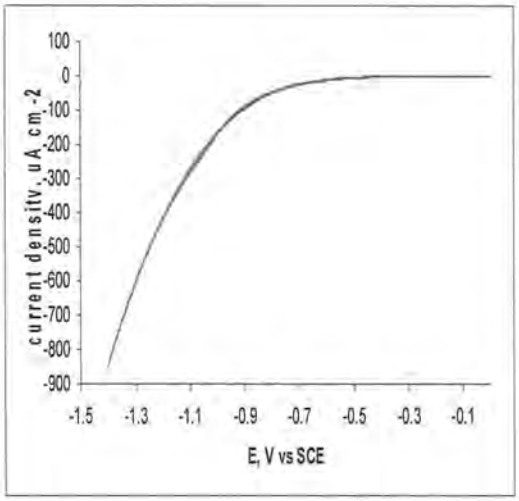

Fig. 3.19 CV of 1.5 M HNO_3 and silicon substrate Scan rate 20mV s^{-1}, electrode area 0.5cm^2

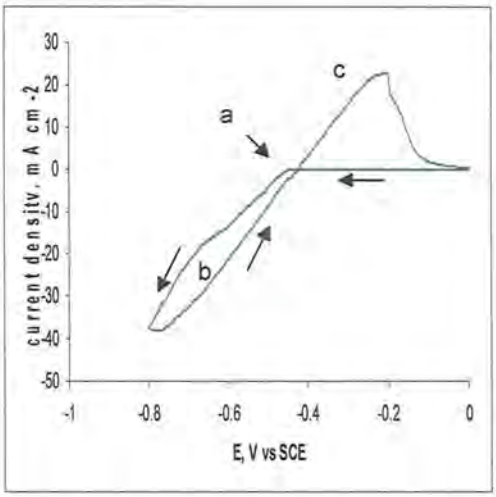

Fig. 3.20 CV of 1.5 M HNO_3 and 500 mM $Pb(Ac)_2$ with silicon substrate. Scan rate 20mV s^{-1}, electrode area 0.5cm^2. Direction of scan indicated by arrows.

Figure 3.19 shows the CV obtained for silicon in 1.5 M nitric acid. The only electrochemical process apparent is a cathodic current starting at -0.7 V *vs.* SCE arising from the reduction of H^+ to hydrogen. The reduction of hydrogen is occurring at a more negative potential compared to the gold substrate which started at around -0.5 V *vs.* SCE. This is because silicon is a poorer conductor than gold therefore a higher overpotential is required for H^+ reduction to occur. The CV of the solution containing 1.5 M nitric acid and 500 mM lead acetate is shown in figure 3.20 On the negative (cathodic) scan no current is seen until -0.45 V *vs.* SCE where the reduction of lead onto silicon starts to occur, (point a). A maximum current density of about -38 mA cm^{-2} is reached then on the reverse (anodic) scan a nucleation loop "b" is produced. This is from the reduction of Pb^{2+} onto lead already deposited on the substrate. At potentials from -0.42 V *vs.* SCE on the anodic scan a stripping peak is observed, "c". This is from the oxidation of deposited lead. Compared to the stripping peak on the CV of 500 mM lead acetate 1.5 M nitric acid with a gold electrode (figure 3.2) this peak is much smaller with a maximum current density of around 25 mA cm^{-2}, opposed to 67 mA cm^{-2} with the gold substrate. Again this probably due to the lower conductivity of silicon. The potentials for the reduction and stripping of lead are in close agreement to those obtained by Ivanova *et al* [1] they noted that the deposition potential for lead depositing onto silicon was more negative than $E^o_{Pb^{2+}/Pb}$ as is the case here and they suggested that this was indicating poor lead-silicon interaction, and 3D growth rather than 2D monolayer formation. This is supported by Staikov *et al*

who studied the growth of Pb films on silicon by electrodeposition [8]. Figure 3.21 shows the CV obtained for the solution containing 1.5 M HNO_3 and 10 mM TeO_2. At about -0.10 V *vs.* SCE on the cathodic scan the current density starts to increase this results from the reduction of $HTeO_2^+$ on to the silicon substrate. This assumption is supported by the results from Ivanova[1] and Myung[4] who showed that tellurium reduction started at this potential. Unlike the CV of the gold substrate in 10 mM TeO_2 there are no separate distinct peaks for the two tellurium reduction reactions. On the anodic scan there is a very narrow nucleation loop which is possibly from further reduction of $HTeO_2^+$ on to previously deposited tellurium (point d). Some of the current seen in this region of the scan is probably also from hydrogen evolution. No anodic current from oxidation of deposited tellurium is produced on the reverse scan implying that deposition of tellurium is irreversible.

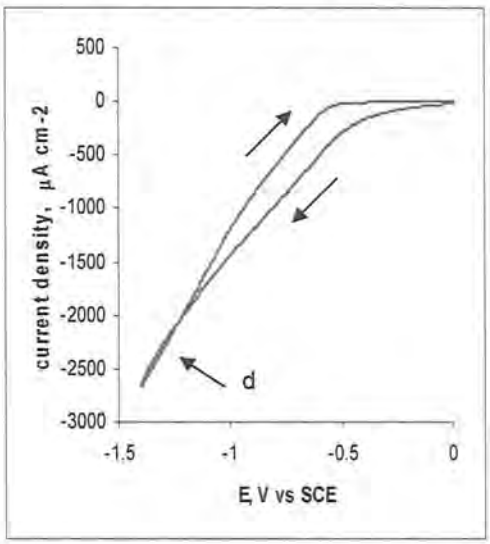

Fig. 3.21 CV of 1.5 M HNO_3 and 10 mM TeO_2 with silicon substrate, Scan rate 20mV s^{-1}, electrode area 0.40 cm^2. Direction of scan indicated by arrows

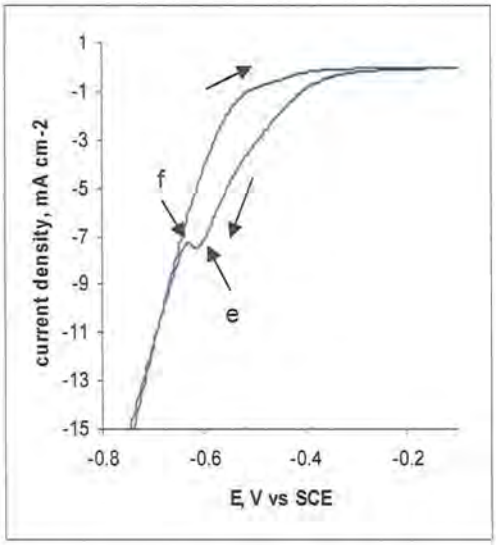

Fig 3.22 CV of 1.5 M HNO_3, 500 mM $Pb(Ac)_2$, 10 mM TeO_2 with silicon substrate. Scan rate 20mV s^{-1}, electrode area, 0.08 cm^2. Direction of scan indicated by arrows

Figure 3.22 is the CV from the solution containing all three components used in the deposition of lead telluride. On the cathodic scan at about -0.30 V *vs.* SCE there is an increase in current density due to $HTeO_2^+$ reduction. According to Ivanova *et al* [1] the current peak at -0.61 V *vs.* SCE (point e) is due to diffusion limited reduction of $HTeO_2^+$. From point f (-0.63 V *vs.* SCE) to more negative potentials the current density increases rapidly due to the deposition of bulk lead and hydrogen evolution. Between these two points is the potential range where stoicheometric PbTe is deposited. On the anodic scan there are no stripping peaks present indicating that

deposition of PbTe is irreversible. The data shown in the CVs demonstrates the underpotential deposition process as follows. For the deposition of lead alone no current is seen until -0.45 V where lead reduction begins. For the solution containing tellurium alone at this potential the current density was 0.23 mA cm^{-2}, however for the solution containing both lead and tellurium at -0.45 V the current was 1.95 mA cm^{-2}. This extra current is probably from the underpotential co-deposition of lead.

3.4 Deposition of bulk PbTe onto Silicon: the effects of deposition potential on film composition and morphology

A series of bulk films of PbTe were deposited at various potentials over the range from -0.35 V to -0.80 V *vs.* SCE. An etching solution based on that used by Vazsonyi *et al* [9] of 500 parts of 48% HF to 1 part nitric acid was used. Also 0.1 g per litre sodium nitrite was added to the solution to homogenise the etching, etching was for one minute. The solution used for depositing the films contained 50 mM $Pb(Ac)_2$, 1 mM TeO_2 and 0.1 M nitric acid. Depositions were carried out for two hours without stirring at ambient conditions. After each deposition the composition of the film was investigated by EDXS measurements, the morphology by SEM imaging and their crystallinity by wide angle x-ray diffraction analysis. Figure 3.23 shows the current density / time transients for each film deposition, the current density increases with increasing negative deposition potential, which is to be expected. Current density was calculated by dividing the current by the surface area of the wafer exposed to the solution. No curve is shown for deposition at -0.35 V since the current density was so small only a featureless line would be seen on the figure 3.23.

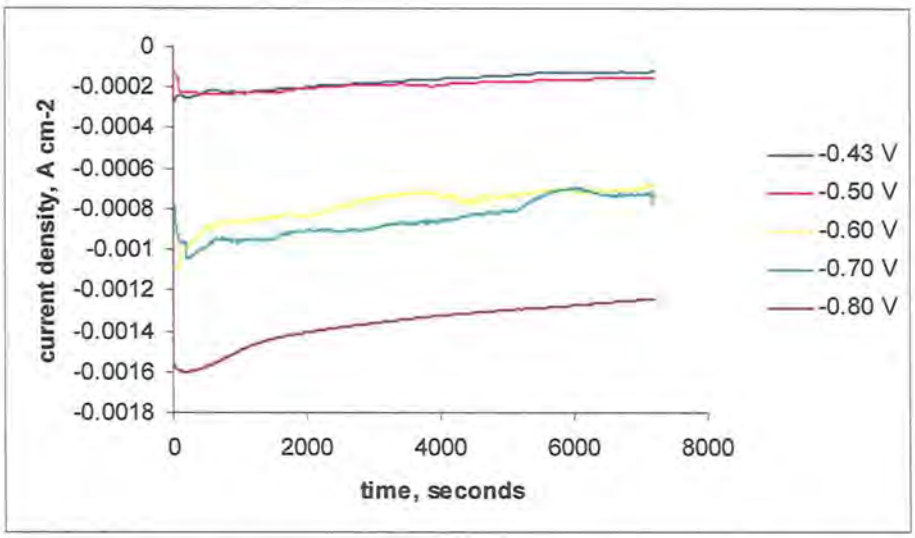

Fig. 3.23 Current density time transients for the deposition of bulk PbTe films on silicon at potentials between -0.43 V and -0.80 V vs. SCE.

The transients show the typical features of an initial increase of current density after the potential step due to double layer charging then a gradual decrease indicating nucleation and film growth under diffusion controlled conditions [10]. The smoother curves seen for -0.43 V, -0.50 V and -0.80 V suggest that a steady state condition is being reached.

The variation of film composition as a function of deposition potential is shown in figure 3.24 as a plot of average lead content, at.% Pb at each potential investigated as measured by EDXS

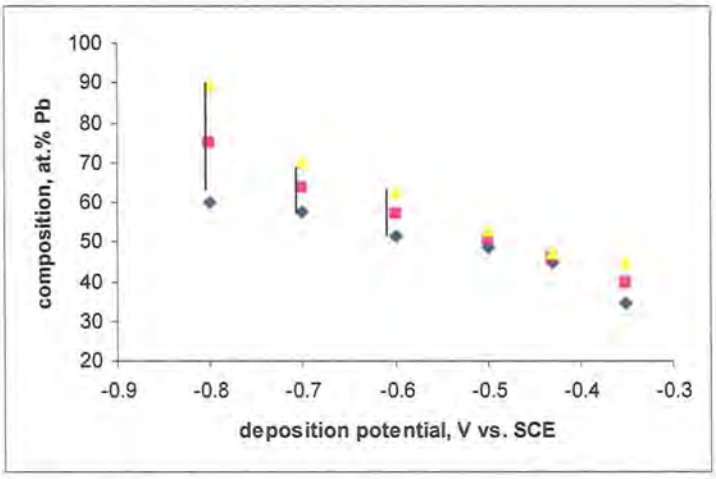

Figure 3.24 graph showing film composition as a function of deposition potential. Triangles and diamonds indicate the upper and lower 95% error limits.

The film composition clearly shows an almost linear trend of increasing lead content with increasing deposition potential. An average stoicheometric film was produced at -0.50 V. At lower potentials the films became tellurium rich and at higher potentials the films became lead rich. As the deposition potential becomes more negative the deposition of lead is favoured over that of tellurium therefore producing lead rich films. The potential range over which stoicheometric co-deposition of lead and tellurium occurs can be estimated from this data to be approximately between -0.45 and -0.55 V *vs.* SCE. Also with more negative potentials the film composition becomes less uniform as indicated by the wider error limits.

Wide angle XRD analysis was performed on each film producing the diffractograms as shown in figures 3.25 to 3.28. For the film deposited at -0.35 V no XRD was carried out as the film was too thin to obtain a useful result. In all the diffractograms multiple sharp peaks for PbTe are seen suggesting a polycrystalline structure [11]. The most intense reflections for all the films come from the (200) and (220) lattice planes for PbTe, in all cases the largest being the (220) reflection. This indicates that these are the dominant growth directions. At -0.43 V and -0.50 V peaks corresponding to elemental tellurium are seen at 22.92° (for -0.43 V) and 19.94°, 57.74° and 61.46° (for -0.50 V). At more negative potentials these peaks are not present instead peaks for lead are seen at approximately 31.5 ° and 36.5°. These correspond to the (111) and (200) lattice planes. At -0.80 V a third peak at 62.26° is observed which corresponds to the (311) planes.

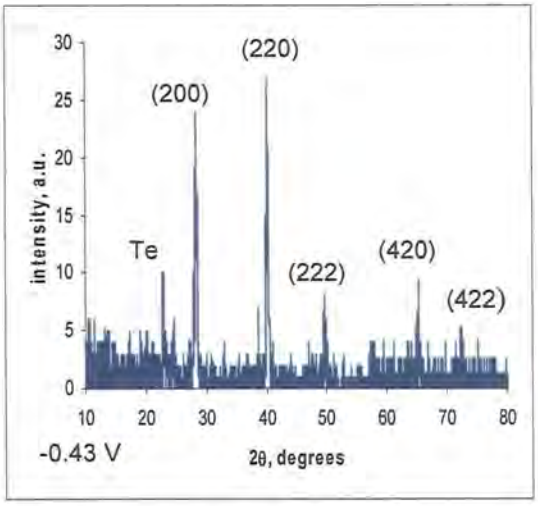

Fig. 3.25 Wide angle XRD for the film deposited at -0.43 V vs. SCE.

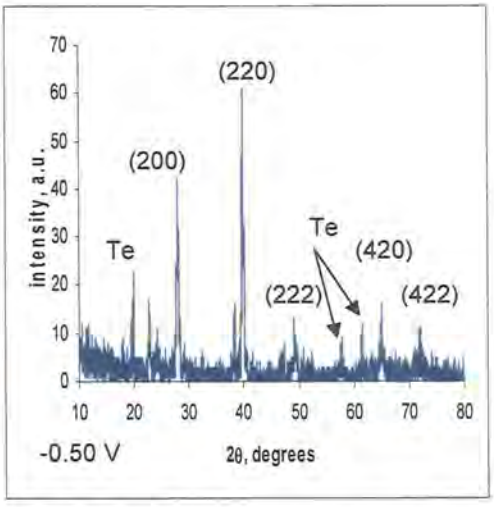

Fig. 3.26 Wide angle XRD of the film deposited at -0.50 V vs. SCE

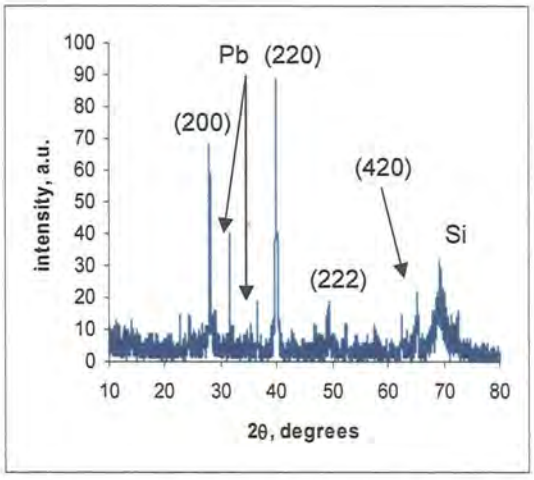

Fig. 3.27 Wide angle XRD for the film deposited at -0.70 V vs. SCE.

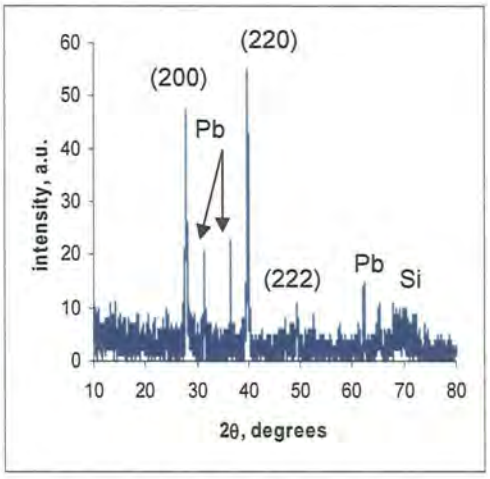

Fig. 3.28 wide angle XRD for the film deposited at -0.80 V vs. SCE.

These findings support the composition data obtained by EDXS that at more negative potentials lead deposition tends to predominate over tellurium. SEM micrographs of the deposited films are shown in figures 3.29 to 3.34. At -0.35 V *vs.* SCE the surface has relatively large crystals packed closely together, at more negative potentials the crystals become smaller and spaced further apart. At -0.70 V *vs.* SCE much larger regular blade or slab shaped crystals are seen. These are probably crystals of lead overpotentialy deposited onto PbTe.

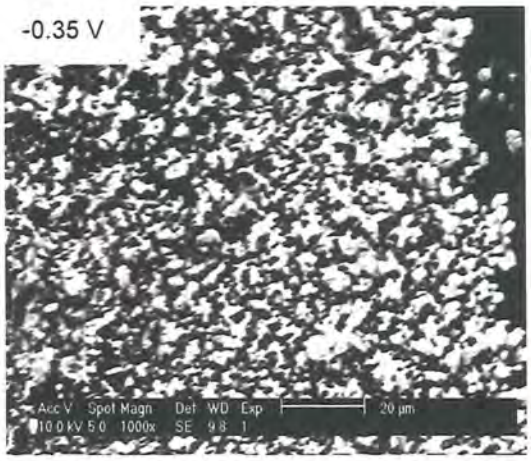

Fig. 3.29 SEM micrograph of the film deposited at -0.35 V vs. SCE. Scale bar is 20 µm

Fig. 3.30 SEM micrograph of the film deposited at -0.43 V vs. SCE. Scale bar is 20 µm

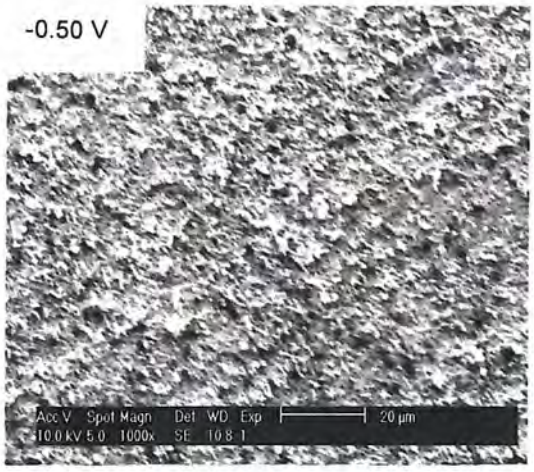

Fig. 3.31 SEM micrograph of the film deposited at -0.50 V vs. SCE. Scale bar is 20 µm

Fig. 3.32 SEM micrograph of the film deposited at -0.60 V vs. SCE. Scale bar is 20 µm

Fig. 3.33 SEM micrograph of the film deposited at -0.70 V vs. SCE. Scale bar is 20 µm.

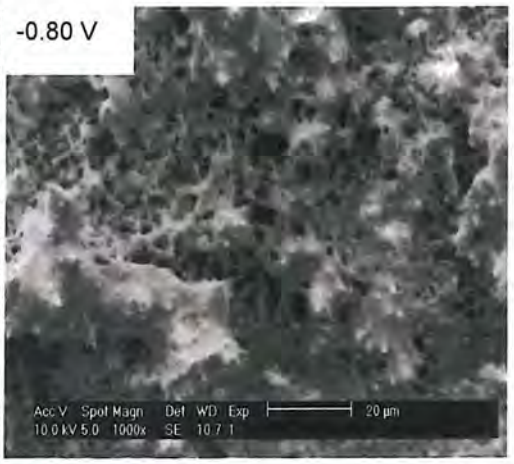

Fig. 3.34 SEM micrograph of the film deposited at -0.80 V vs. SCE. Scale bar is 20 µm.

This is supported by the composition and wide angle XRD data which indicate a lead rich composition and the presence of crystalline lead respectively at this potential. Finally at -0.80 V *vs.* SCE a porous mesh structure is observed, possibly arising from hydrogen bubble formation. This shows that the deposition potential also affects film morphology as well as composition. All of the films deposited were dark grey/black. They were powdery and not compact the powdery material is possibly the loose crystallites which are seen in the micrographs. This indicates poor adhesion to the silicon substrate.

3.5 Deposition of bulk lead telluride films onto gold substrates using a nucleation pulse

Two series of deposition experiments were performed. The first used very short nucleation pulses up to 500 μs in duration. The second used a nucleation pulse of one second followed by a deposition pulse lasting from five to 30 minutes.

3.5.1 Deposition using short nucleation pulses

Bulk lead telluride films were deposited from a solution containing 50 mM $Pb(Ac)_2$, 1 mM TeO_2 and 0.15 M HNO_3. The nucleation pulses were 50,100,250 and 500 μs in duration and all at a potential of -0.43 V *vs.* SCE. The growth pulses were for 10 minutes, 30 minutes, 1 hour and two hours all at a potential of -0.15 V *vs.* SCE. Depositions were carried out at room temperature without stirring. The mean composition of each film was found using EDXS and is shown in figure 3.35. The 95% confidence limits for the mean are also indicated to give an idea of the uniformity of the composition. For comparison the composition of two films deposited without a nucleation pulse are also included.

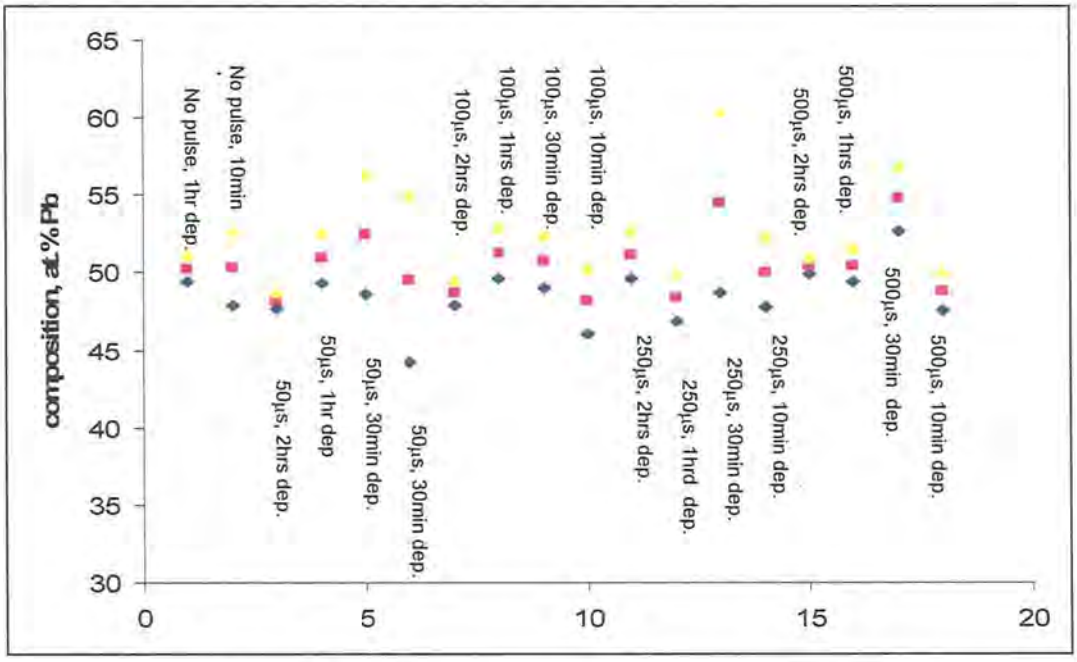

Fig. 3.35 Composition data from films deposited onto gold using a nucleation pulse prior to deposition, Ignore horizontal axis. Mean composition is indicated by squares upper and lower 95% confidence limits of the mean are indicated by the triangles and diamonds.

It can be seen that overall there is no significant effect on composition between films deposited with a nucleation pulse and those without. Also the duration of the nucleation pulse does not seem to influence the film composition. However it seems that the duration of deposition after the pulse has some effect on the uniformity of film composition. With decreasing deposition times the film composition becomes less uniform as indicated by the widening of the confidence interval of the mean. This is seen most clearly with the films deposited with a 50 μs nucleation pulse. Scanning electron microscopy of the deposited films (figures 3.36 to 3.51) showed that the duration of deposition had a significant effect on film morphology. For all the films deposited the film morphology became rougher and polycrystalline with increasing duration of deposition. The films deposited for two hours where a 250 or 500 μs nucleation pulse were used (figs. 3.36 and 3.37) appear to be somewhat less rough then the films deposited for two hours with a 50 or 100 μs nucleation pulse (figs. 3.44 and 3.45). For films deposited over one hour the difference in morphology is more obvious between using longer and shorter nucleation pulses, figs 3.38/3.39 vs. 3.46/3.47.

250 µs nucleation pulse -0.43 V, depot. -0.15 V

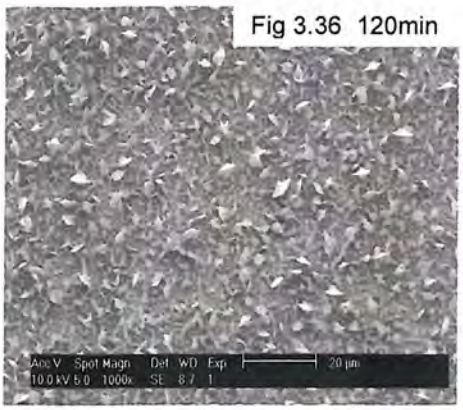

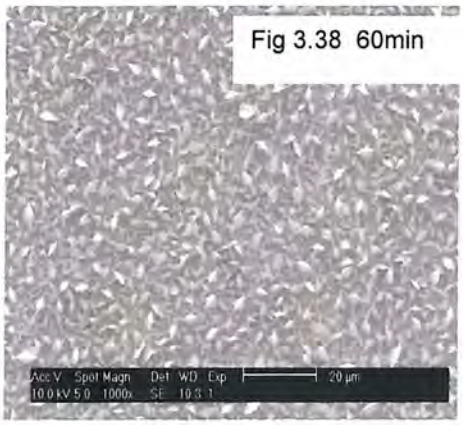

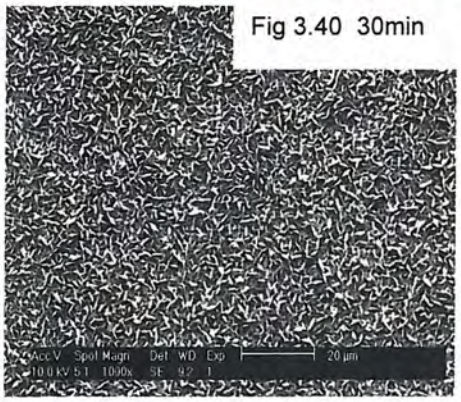

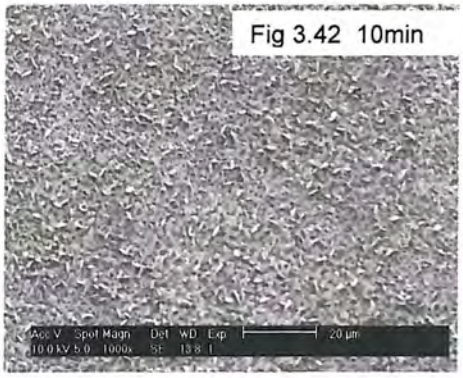

500 µs nucleation pulse -0.43 V, depot. -0.15 V

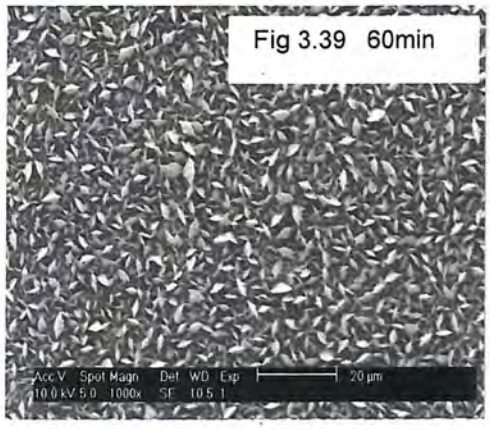

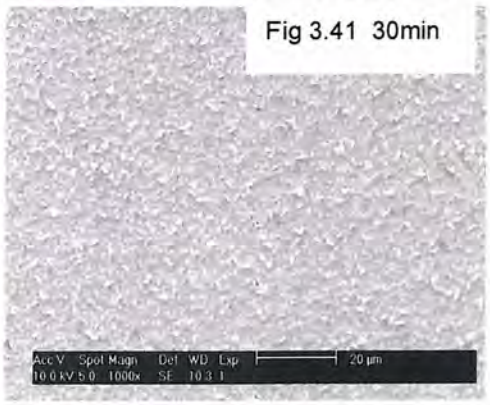

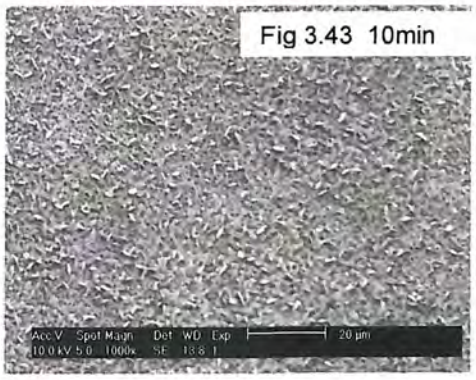

Scale bar is 20 µm for all micrographs

50 µs nucleation pulse -0.43V, depot. -0.15V

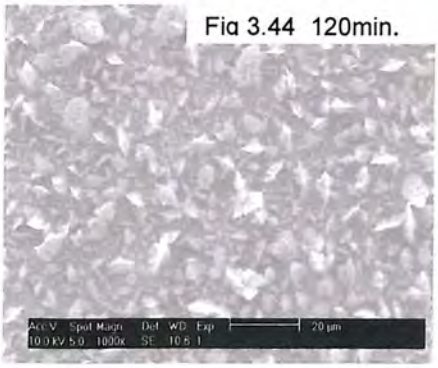

Fig 3.44 120min.

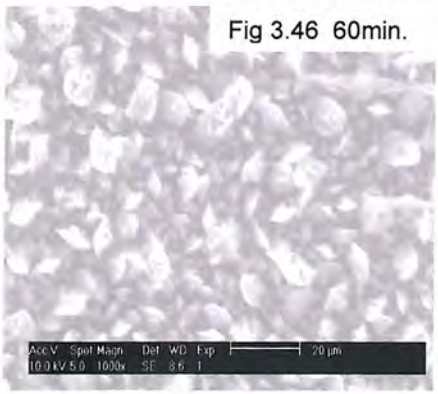

Fig 3.46 60min.

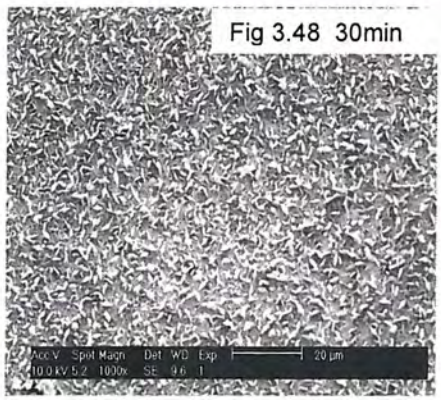

Fig 3.48 30min

Fig 3.50 20min

100 µs nucleation pulse -0.43V, depot. -0.15V

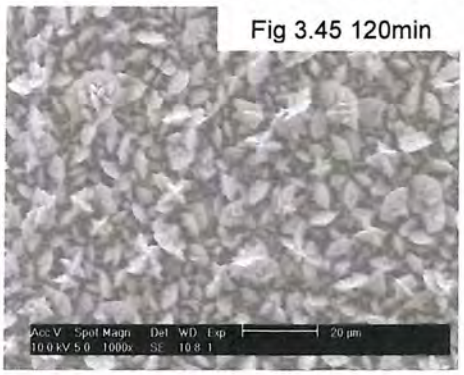

Fig 3.45 120min

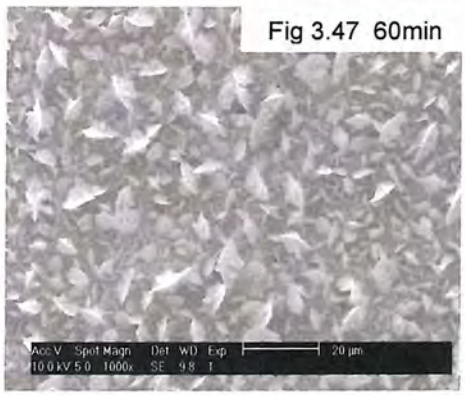

Fig 3.47 60min

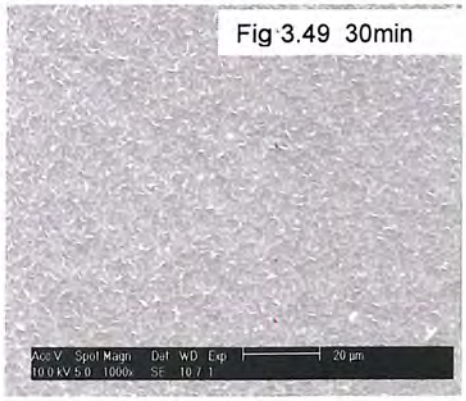

Fig 3.49 30min

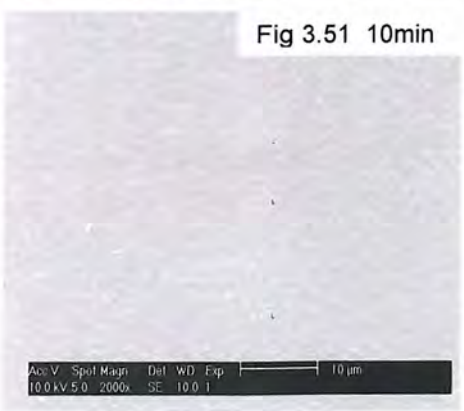

Fig 3.51 10min

Scale bar is 20 µm for all micrographs

The observed increase in crystalline structure as deposition progresses may be due to a changes in film growth direction. At early stages the film growth is possibly two dimensional as the nucleation sites grow outwards and then coalesce to form a continuous film. Then growth becomes three dimensional with crystals starting to form on the film surface. The increase in a polycrystalline film morphology with a longer deposition period is also demonstrated by the wide angle x-ray diffractograms of the films. Figures 3.52 to 3.55 are the diffractograms for films deposited using a 100 μm and 250 μm nucleation pulse and deposition durations of 10 minutes and two hours.

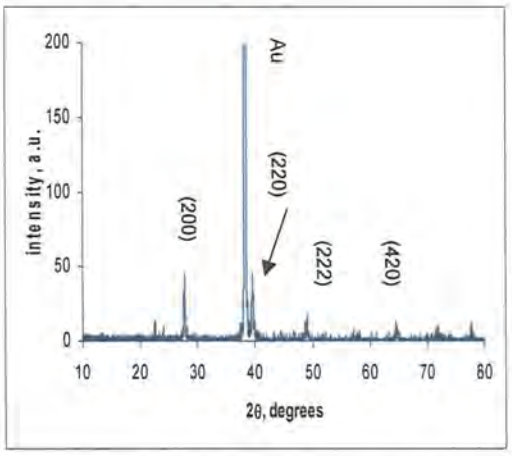

Fig. 3.52 100 μs pulse and deposition for 2 hours

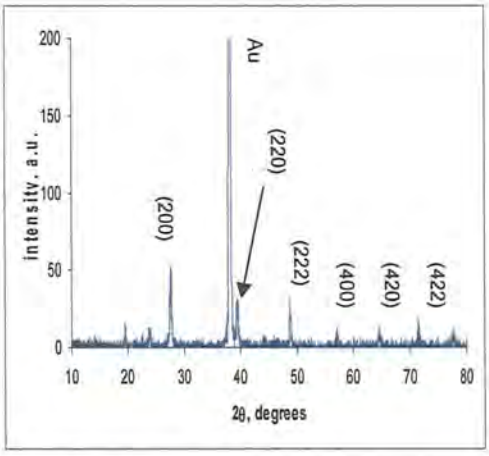

Fig. 3.53 250 μs pulse and deposition for 2 hours

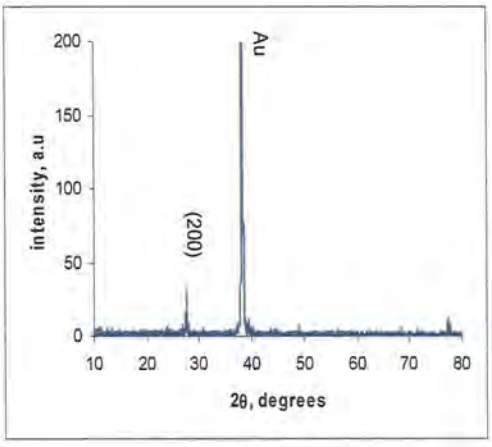

Fig. 3.54 100 μs pulse and deposition for 10 min.

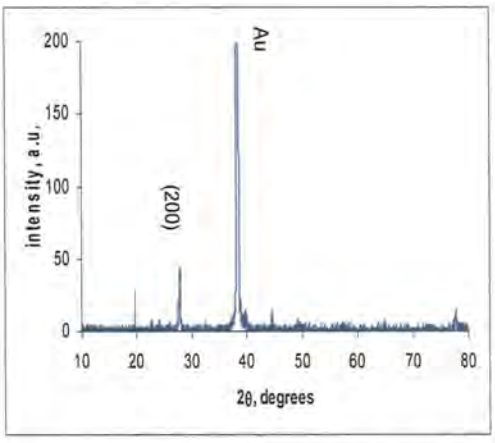

Fig. 3.55 250 μs pulse and deposition for 10 min

For the films deposited for ten minutes one diffraction peak due to the (200) lattice planes of PbTe is present. The diffractograms for the films deposited over two hours show higher order diffraction peaks indicating a less ordered film morphology as demonstrated by the SEM micrographs.

3.5.2 Deposition using long nucleation pulses

A series of bulk lead telluride films were deposited onto gold using a one second nucleation pulse at -0.43 V *vs.* SCE followed by deposition at -0.15 V *vs.* SCE for 5,6,8,10 and 30 minutes. The solution was the same as that used for the depositions with shorter pulses. For deposition durations up to and including eight minutes the films appeared to be grey and metallic. After ten minutes the film looked darker and less metallic and the film deposited for 30 minutes was dull and not compact. All the films were deposited with stirring of the solution. Three more films were deposited using the same pulse potentials without stirring for 7,15,30 and 60 minutes, again the films were shiny grey and metallic in appearance. Film composition was good, all the deposited films had a mean composition ranging from 46 to 50 at.% Pb determined by EDXS. There appeared to be no difference in film composition between stirring and not stirring the solution during deposition. The SEM micrographs of some of the films (figures 3.56 to 3.59) however show that films deposited without stirring the solution were much smoother than the films deposited with stirring. In fact at 2000x magnification no surface features were visible for films deposited without stirring.

Fig. 3.56 SEM micrograph of film deposited for 8 minutes at -0.15 V with stirring.
Scale bar is 10 microns

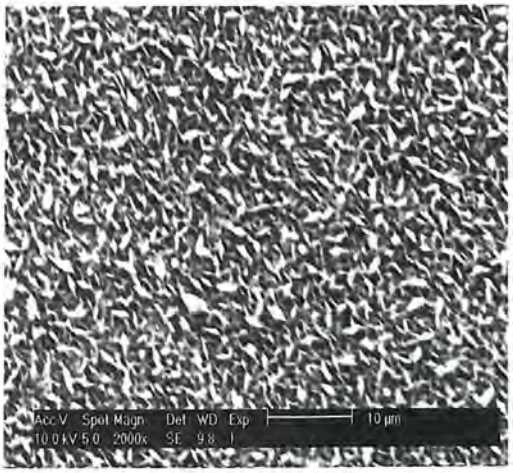

Fig. 3.57 SEM micrograph of film deposited for 30 minutes at -0.15 V with stirring.
Scale bar is 10 microns.

Fig. 3.58 SEM micrograph of film deposited for 30 min at -0.15V with no stirring, scale bar 10 µm

Fig. 3.59 SEM micrograph of film deposited for 1hr at -0.20 V with no stirring. Scale bar is 10 µm.

It also seems that the duration of deposition affects the film morphology more when the solution is stirred. No difference is seen for the films deposited without stirring over 30 minutes or one hour. For the films deposited with stirring a fairly rough surface is produced after 30 minutes. The wide angle x-ray diffractograms for the films were all the same indicating very weak diffractions form the (200) lattice planes, just exceeding the background "noise". The low intensity of the diffraction peaks is probably due to the films being very thin since the deposition duration was short. Figure 3.60 is a XRD typical of the films, in this case the deposition regime was -0.43 V for 1.5 s then deposition at 0.30 V for 15 minutes. Mean composition was 48.38 at.% Pb (+/- 0.52 at.% Pb).

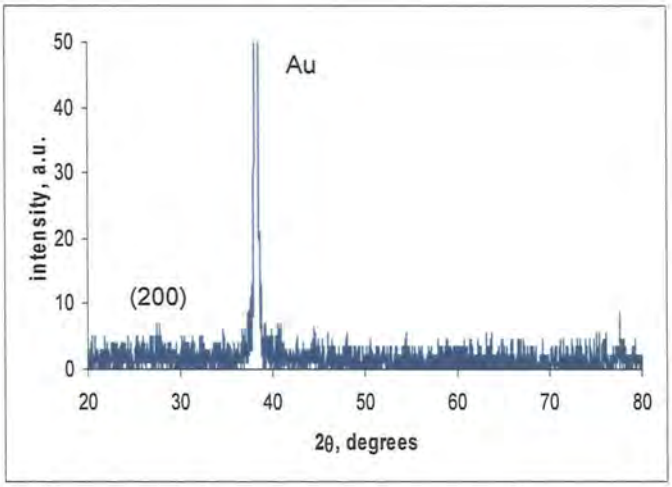

Fig. 3.60 Wide angle XRD showing the pattern typical of the metallic films deposited using a longer nucleation pulse and short deposition duration.

Summarising the results, it can be said that using a longer nucleation pulse and shorter deposition duration produces better film morphology, although because of the short duration of deposition the films are very thin. There seems to be no difference in composition between films deposited with and without a nucleation pulse.

3.6 Deposition of bulk lead telluride films onto silicon substrates using a nucleation pulse

Bulk films of PbTe were deposited onto silicon using a double pulse regime. Results from three of the films obtained are presented. Films were deposited using the standard solution, 50 mM $Pb(Ac)_2$, 1 mM TeO_2, 0.15 M HNO_3 without stirring during deposition. Silicon substrates were cleaned in 50% v/v nitric acid at 80°C for 1 minute then etched in 5 M NH_4F for 10 minutes. The deposition regime was a nucleation pulse for 0.5, 1 and 1.5 seconds at -0.60 V *vs.* SCE followed by deposition for one hour at -0.43 V *vs.* SCE. All of the films were smooth and showed improved adhesion as compared to other bulk films on silicon. The mean film composition was also good, 47.94 at.% Pb using a 1.5 s pulse, 49.65 at.% Pb for 1.0 s and 49.30 at.% Pb for a 0.5 s nucleation pulse. The film composition therefore improved slightly for shorter nucleation pulses. Three other films were also deposited using a nucleation pulse at -0.65 V *vs.* SCE for the same durations and deposition at -0.50 V *vs.* SCE for one hour. Again the best compositions were seen for films deposited with the shorter nucleation pulses. Figure 3.61 shows the film compositions obtained.

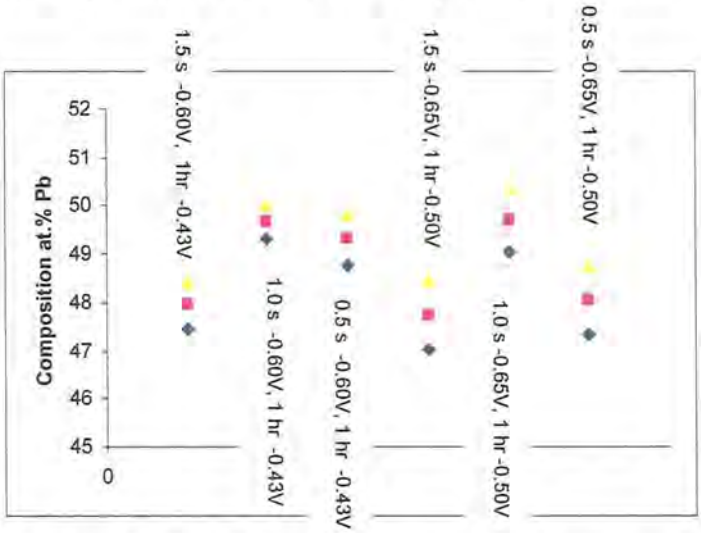

Fig. 3.61 Composition data for the bulk films deposited onto silicon using a nucleation pulse. 95% confidence limits are indicated by the triangles and diamonds.

The SEM micrographs for the films are shown below. The film deposited using a 1.5 second nucleation pulse has a slightly rougher morphology than the films deposited with shorter nucleation pulses. The scale bar is 10 μm for each micrograph.

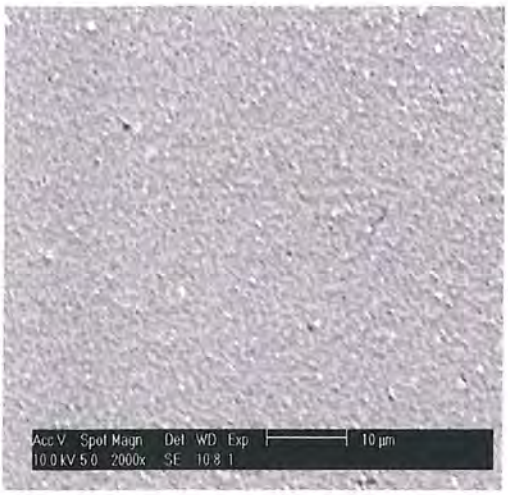

Fig. 3.62 of film deposited after 1.5 s at -0.60V then deposition at -0.43 V for 1 hour.

Fig. 3.63 SEM of film deposited after 1 s at -0.60V then deposition at -0.43V for 1 hour.

Fig. 3.64 SEM of film deposited after 0.5 s at -0.60V then deposition at -0.43V for 1 hr.

Figures 3.65 to 3.67 overleaf show the wide angle x-ray diffractograms for the films. All three diffractograms show peaks indicating that the principle growth direction is in the (200) and (220) lattice planes. For the film deposited with a 1.5 second nucleation pulse the (200) direction is more favoured than the (220). For the other two films deposited with one and 0.5 second nucleation pulses growth is only slightly more favoured in the (200) direction over the (220) direction. For the film deposited

with a 0.5 second nucleation pulse there is a small peak at 49.30 ° (2θ) indicating some growth in the (222) planes as well. This suggests that the direction of crystalline growth is possibly influenced by the duration of the nucleation pulse. The diffractogram for the film deposited with a one second nucleation pulse also shows an extra peak for silicon.

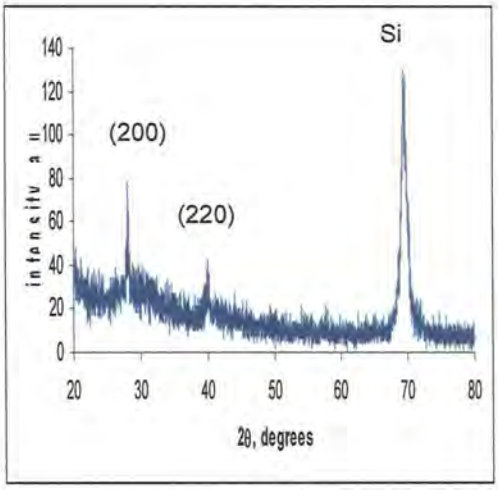

Fig. 3.65 Wide angle XRD for the film deposited using a 1.5 s nucleation pulse at -0.60 V, then deposition at -0.43 V for one hour.

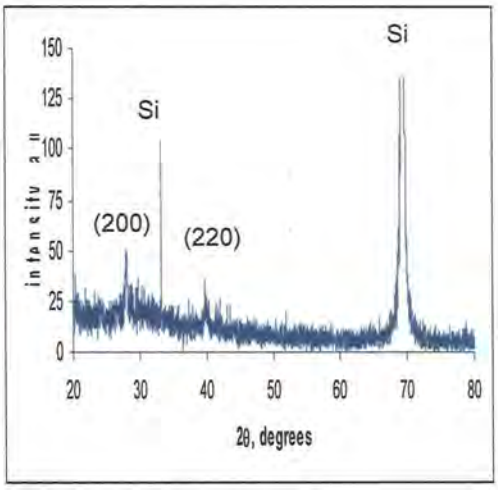

Fig. 3.66 Wide angle XRD for the film deposited using a 1 s nucleation pulse at -0.60 V then deposition at -0.43 V for one hour.

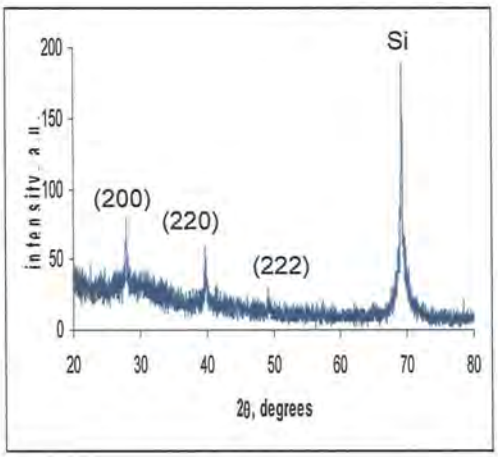

Fig. 3.67 Wide angle XRD for the film deposited Using a 0.5 s nucleation pulse at -0.60 V then deposition at -0.43 V for one hour.

3.7 Conclusions

The cyclic voltammetry experiments performed using gold on glass substrates indicated that an underpotential deposition mechanism was occurring for the deposition of lead telluride. For the experiment with both lead and tellurium species in the solution an increase in current density in the potential range of tellurium deposition was observed. The increased current density can be attributed to the underpotential co-deposition of lead with tellurium to form lead telluride. For CV experiments using silicon substrates similar results were obtained. The underpotential co-deposition of lead with tellurium was also demonstrated. The current densities observed were lower than those with gold electrodes due to the lower conductivity of silicon. No stripping peak was seen on the CV for lead telluride deposition indicating that deposition of lead telluride is not reversible. The peak/wave positions on the CVs for both gold and silicon substrates were in good agreement with the literature [1,4,5,6].

For depositing PbTe films on gold an almost stoicheometric composition could be produced over the deposition potential range of -0.20 V to about -0.35 V *vs.* SCE where the mean composition was 56 at.% Pb. At more negative deposition potentials the films became progressively lead rich. Micrographs of the films also show a stable morphology up to -0.35 V *vs.* SCE. At more negative potentials the films become much rougher, the micrograph of the film deposited at -0.80 V shows a very flaky surface. This is possibly due to hydrogen evolution creating an uneven exposure of the substrate surface to the solution. The wide angle x-ray diffractograms support both the composition data and SEM images. They indicate that films deposited at -0.17 to -0.35 V *vs.* SCE were composed of PbTe whereas at more negative potentials peaks indicating the presence of bulk lead were seen. The favoured direction of growth for PbTe was in the (200) lattice planes. The deposited films looked dark grey/black and were not metallic in appearance. They demonstrated poor adhesion, when scratched gently.

For films deposited onto silicon there was a linear trend of increasing proportion of lead with increasing cathodic deposition potential. Approximately stoicheometric films were deposited between -0.40 and -0.50 V *vs.* SCE. Wide angle XRD supports this finding. Diffractograms for films deposited at more positive potentials indicate the presence of bulk tellurium mixed in with PbTe. For films deposited at higher cathodic potentials diffraction peaks from bulk lead were seen.

SEM micrographs showed a change in film morphology as well. With increasing cathodic potential the films became rougher. Like the films deposited onto gold the deposited films were black and non-metallic they also demonstrated poor adhesion to the silicon substrate. These results mirror those from the films deposited onto gold. Both sets of data suggest that there is a potential range over which reasonably stoicheometric films with good morphology can be deposited. This range is about the same for depositions on gold and silicon substrates. More negative deposition potentials produce films of poor quality.

When a nucleation pulse was used to deposit bulk films onto gold no overall effect in film composition was seen. However the duration of the nucleation and growth pulses affected the film morphology. Longer nucleation pulses and shorter deposition times produced the best films. The shorter deposition time possibly improves film morphology by preventing the formation of a rough film surface. Stirring the solution did not seem to have much effect on the composition and morphology of films. For bulk films deposited onto silicon with a nucleation pulse again there was no overall difference in film composition compared to films deposited without a nucleation pulse. In contrast to films deposited onto gold, stirring the solution during deposition adversely effected the film composition and morphology. One film deposited with stirring using a nucleation pulse of one second at -0.70 V and deposition at -0.43 V for one hour was almost entirely tellurium (98.4 at.% Te). The duration of the nucleation pulse might possibly be influencing film composition and morphology. A shorter pulse seemed to slightly improve both characteristics. The wide angle x-ray diffractograms seem to show that the direction of growth of the PbTe crystal structure is affected by the duration of the nucleation pulse.

References

1. Y.A. Ivanova, D.K. Ivanou, E.A. Streltsov. *Electrochem. Commun.* **(2007)**, vol. 9, pp. 599-604

2. M. P. R. Panicker, M. Knaster, F. A. Kroger, *J. Electrochem. Soc.* **(1978)**, vol. 125, p. 566-572

3. M.S. Martın-Gonzalez, A.L. Prieto, R. Gronsky, T. Sands, A.M. Stacy. *J. Electrochem. Soc.* **(2002)**, vol. 149, p. C546-C554

4. F. Xiao B. Yoo, M.A. Ryan, K-H. Lee, N.V. Myung. *Electrochemica Acta,* **(2006)**, vol. 56, pp. 1101-1107

5. F. Xiao, B Yoo, K.N. Bozhilov, K-H. Lee N.V. Myung, *J. Phys. Chem. C,* **(2007)**, vol. 111, p. 11397-11402

6. I.S. Nandhakumar, X. Li, *Electrochem Commun.* **(2008)**, vol. 10, p. 363-366

7. H. Saloniemi, T. Kanniainen, M. Ritala, M. Leskelä, *Thin Solid Films* (**1998**), 326, pp. 78-82

8. Rashkova B. Guel B. Potzschke R.T. Staikov G. *Electrochim Acta.* **(1998)** vol. 43, p. 3021

9. E Vazsonyi, E. Szil´agyib, P. Petrika, Z.E. Horv´atha, T. Lohnera, M. Frieda, G. Jalsovszky. *Thin Solid Films.* **(2001)**, vol. 388, pp. 295-302

10. T. Gabriel. PhD thesis, University of Southampton, **(2005)**, p. 57

11. S. Kumar, Z.H. Khan, M.A. Majeed-Khan, M. Husain. *Curr. Appl. Phys.* **(2005)**, vol. 5, pp. 561-566

Chapter 4

Deposition of mesoporous lead telluride onto gold and silicon

4. Deposition of mesoporous lead telluride onto gold and silicon

This chapter will first look at the phase diagram and small angle X-ray diffractograms of the liquid crystal template mixture used for mesoporous depositions. This is followed by a brief investigation of the electrochemistry of PbTe deposition onto silicon from a templating mixture. Then the deposition of PbTe onto bare and chemically modified silicon substrates to improve film adhesion is presented. Finally electrodeposition of H_1e-PbTe using double pulse deposition is presented.

4.1 Phase diagram of the liquid crystal templating mixture

Figure 4.1 shows the phase diagram of the liquid crystal mixture that was used for the deposition of mesoporous lead telluride films using the surfactant $C_{16}EO_8$ and 50 mM lead acetate, 1 mM tellurium dioxide, 0.15 M nitric acid.

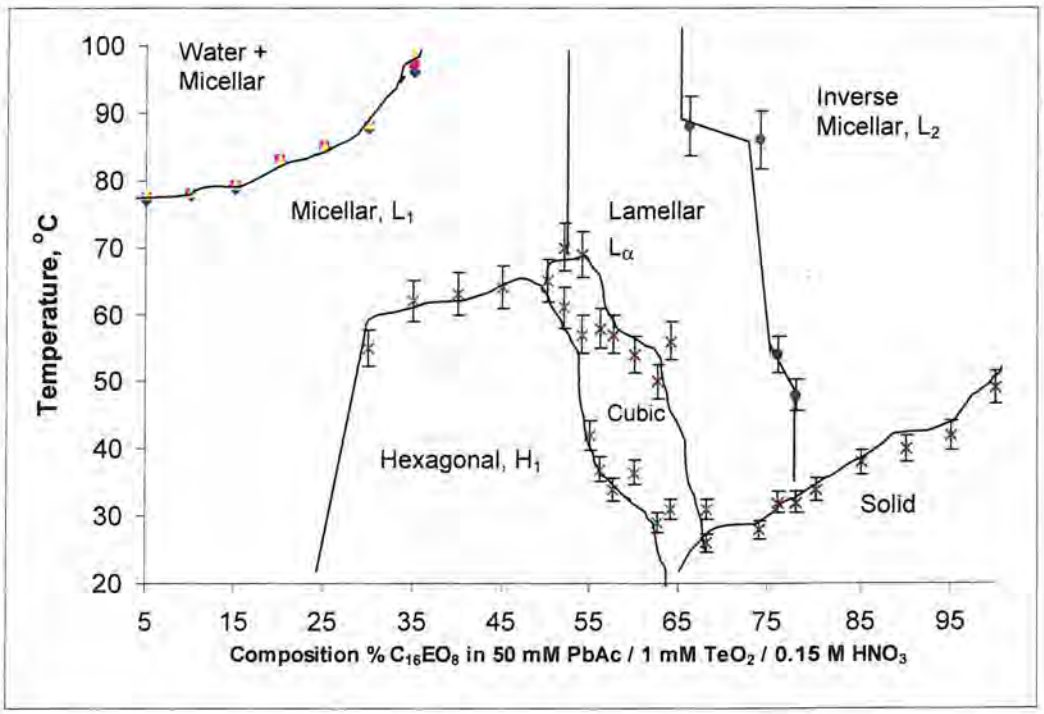

Fig. 4.1 Phase diagram of the $C_{16}EO_8$ / 50 mM $Pb(Ac)_2$, 1 mM TeO_2, 0.15 M HNO_3 electrolyte system, the 95% confidence limits for the mean phase transition temperature are shown.

Comparing the phase diagram shown in figure 6.1 with that of $C_{16}EO_8$ and water (figure 1.7) there seems to be very little change of phase behaviour with addition of the lead acetate / tellurium dioxide / nitric acid electrolyte. No cubic micellar phase is shown as phase transitions occurring at room temperature and above were investigated. The cubic phase is stable only over a narrow composition range and between 30 and 70°C. This would make using this as a templating phase difficult (but not impossible) as heating of the mixture during deposition is required. Also since heating would be needed drying out of the liquid crystal template mixture has to be prevented to maintain the correct composition. The hexagonal phase however is stable over a wide composition range from 25 wt.% to 65 wt.% $C_{16}EO_8$ and up to a temperature of 65 °C which is ideal for deposition of mesoporous films.

4.2 Small angle X-ray diffraction of the liquid crystal template mixture

Figure 4.2 is the small angle x-ray diffractogram of the liquid crystal template mixture used for electrodeposition of mesoporous hexagonal phase lead telluride, 50 wt.% $C_{16}EO_8$ with 50 mM lead acetate, 1 mM tellurium dioxide and 0.15 M nitric acid electrolyte solution.

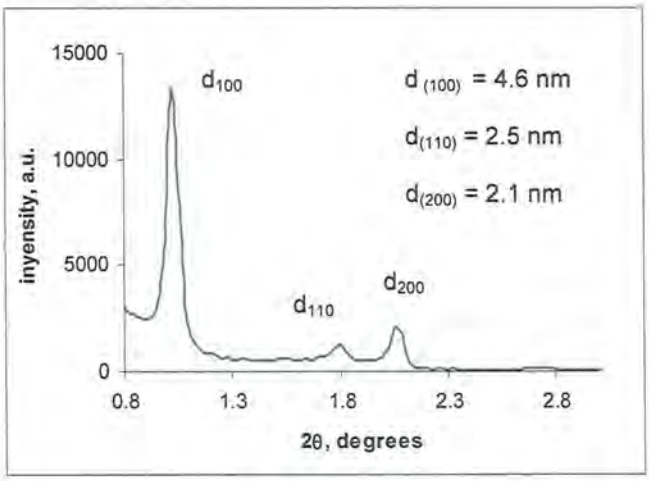

Fig. 4.2 Small angle x-ray diffractogram of 50 wt.% $C_{16}EO_8$ with 50 mM lead acetate and 1 mM tellurium dioxide

Three peaks can clearly be seen arising from diffractions from (100), (110) and (200) lattice planes. The presence of multiple peaks indicates a highly ordered liquid crystalline structure. The principle orientation of the pores is in the (100) direction as

indicated by the dominating peak at 1.02° (2θ). Using Braggs law (equation 2.1) the d-spacings for the (100), (110) and (200) lattice planes are 4.3 nm, 2.5 nm and 1.2 nm. The ratio of these spacings comes close to 1:√3:2 which is the d-spacing ratio for the hexagonal phase. Increasing the concentration of the electrolyte leads to degradation of the liquid crystalline phase structure. This is illustrated with the SAXD of a liquid crystal template mixture composed of 50 wt.% $C_{16}EO_8$ with 500 mM lead acetate, 10 mM tellurium dioxide 1.5 M nitric acid, figure 4.3 below.

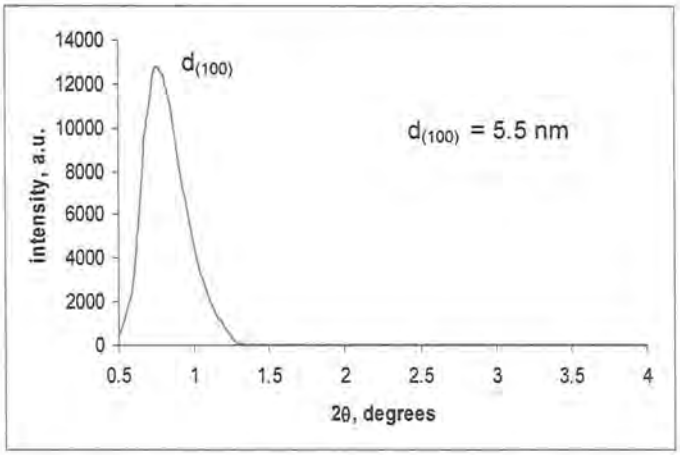

Fig. 4.3 Small angle x-ray diffractogram of 50 wt.% $C_{16}EO_8$ with 500 mM lead acetate and 10 mM tellurium dioxide.

In striking contrast to the diffractogram of the template mixture with 50 mM lead acetate, 1 mM tellurium dioxide only one peak is seen for the (100) pore lattice planes. The higher order diffraction peaks are completely absent indicating a breakdown of the liquid crystalline structure, also the (100) peak is broader and is shifted to a lower angle at about 0.8° 2θ. This indicates a reduced long range spatial order of the pores and the pore spacing is larger at about 5.5 nm. The peak broadening may also be partly due to the presence of the lamellar phase mixed with the hexagonal phase structure. Clearly the higher concentration of the ionic species is having a detrimental effect on the liquid crystal structure this is probably due to the lead and telluryl ions interacting with the surfactant molecules and inhibiting their ability to form a stable and ordered liquid crystal structure.

4.3 A brief study of the electrodeposition of lead telluride onto silicon substrate from a liquid crystal templating mixture

The electrodeposition of lead telluride from a liquid crystal template based on the surfactant $C_{16}EO_8$ was investigated using cyclic voltammetry. Figure 4.4 is a CV of the deposition of lead telluride using a liquid crystal template onto a silicon substrate. The liquid crystal mixture was composed of 50 wt.% $C_{16}EO_8$ and 50 wt.% electrolyte solution containing 50 mM $Pb(Ac)_2$, 1 mM TeO_2 and 0.15 M HNO_3.

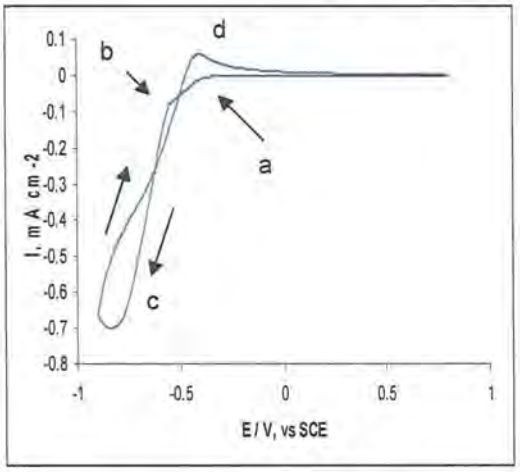

Fig. 4.4 CV of deposition of lead telluride from a liquid crystal template composed of 50 wt.% $C_{16}EO_8$ and 50 wt.% electrolyte solution containing 50 mM $Pb(Ac)_2$, 1 mM TeO_2 and 0.15 M HNO_3. Scan rate, 10 mV s^{-1} electrode area 0.5 cm^2. Direction of scan is indicated by the arrows.

During the cathodic scan no current is seen until about -0.40 V vs. SCE (point a) then there is a gradual increase from the reduction of tellurium. After point "b" the current density increases rapidly from the bulk deposition of lead. Between points "a" and "b" deposition of lead telluride is probably occurring. On the reverse scan a nucleation loop, "c" is produced, this is indicating the further reduction of Pb^{2+} onto deposited lead. At about -0.45 V vs. SCE an anodic peak (d) is seen which represents the stripping of lead. The overall current densities observed for the deposition of mesoporous PbTe are much lower than that for bulk deposition. This is because the liquid crystal template mixture is less conductive than the bulk solution and the higher density slows the movement and diffusion of the lead and tellurium ionic species.

4.4 Deposition of a mesoporous lead telluride film on a silicon substrate and measurement of the band gap energy using FTIR

Preparation of a mesoporous film was attempted using a liquid crystal template mixture composed of 50 wt.% $C_{16}EO_8$ and 50 wt.% electrolyte solution containing 250 mM $Pb(Ac)_2$, 5 mM TeO_2 and 1.5 M HNO_3. Silicon pre-treatment was sonication in IPA for 30 min, hot wash in hydrogen peroxide/HCl for 15 min and etching in 5 M HF for one hour. Deposition was for 20 hours at -0.43 V *vs.* SCE. The template mixture was then removed by soaking in IPA, unlike most films deposited on unmodified silicon the film did not peel off even after overnight soaking. This indicates that film adhesion onto unmodified silicon can be good occasionally but is not reproducible. The film composition was found to be approximately stoichiometric with a mean composition of 51.66 at.% Pb and 48.34 at.% Te. The wide angle x-ray diffractogram presented in figure 4.5 below shows sharp peaks for the (200), (220), (222) and (420) planes of PbTe with the (200) and (220) being much larger than the other two indicating that the crystal growth was principally in these directions. The peak positions and calculated lattice spacings agree closely with the standard data for lead telluride, (see inset). The multiple sharp peaks are indicative of a polycrystalline film structure. The small angle XRD of the same film (diffractogram not shown) did not show any peaks suggesting a mesoporous structure was not present.

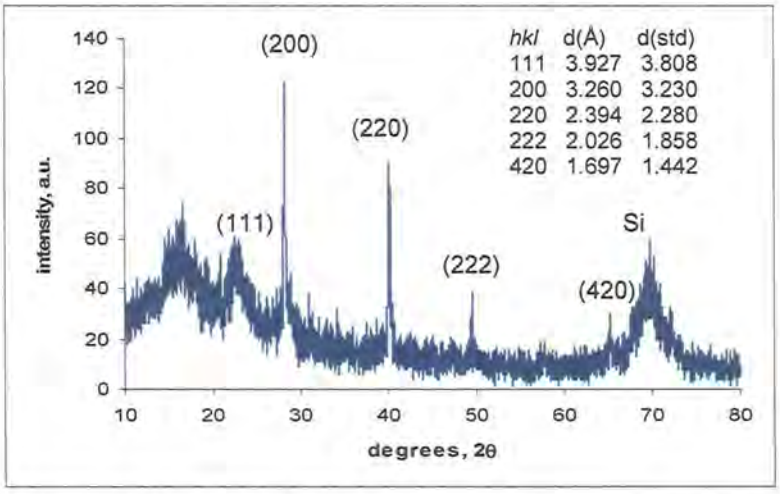

Fig. 4.5 Wide angle XRD of the film, indicating calculated and standard lattice spacings

The optical band gap energy was determined by the process outlined in section 2.6.5. Before obtaining the FTIR spectrum the film thickness was measured using SEM, the observed film thickness was found to be 850 nm, the FTIR absorbance spectrum of the film is shown in figure 4.6

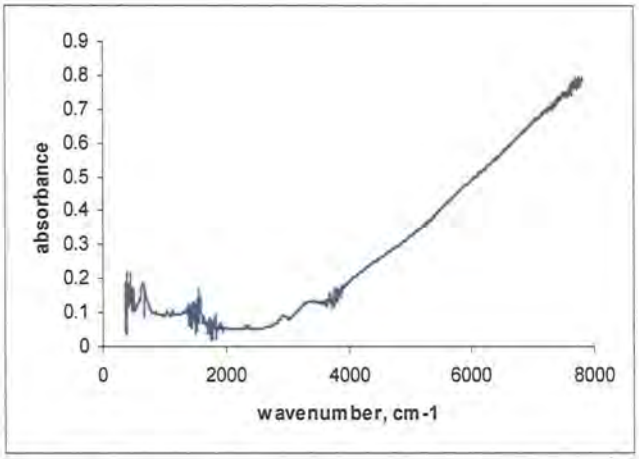

Fig. 4.6 FTIR absorbance spectrum of the film

By converting the wave number scale into μm and obtaining the absorbance coefficient at each data point, the absorbance verses wavelength plot as shown below was obtained, figure 4.7.

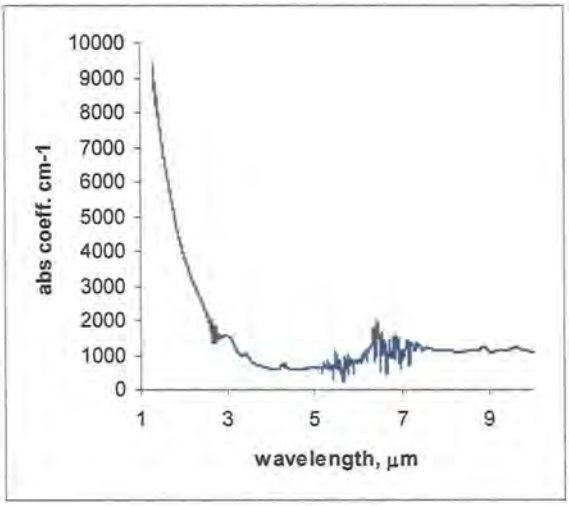

Fig. 4.7 Absorbance coefficient *vs.* wavelength plot for the film

It can be seen that the absorbance coefficient increases rapidly below about 3 μm this is the fundamental absorption edge where the absorbance coefficient changes rapidly with wavelength. Finally converting the wavelength into energy and plotting this against $(\alpha\hbar\nu)^2$ gives the plot in figure 4.8.

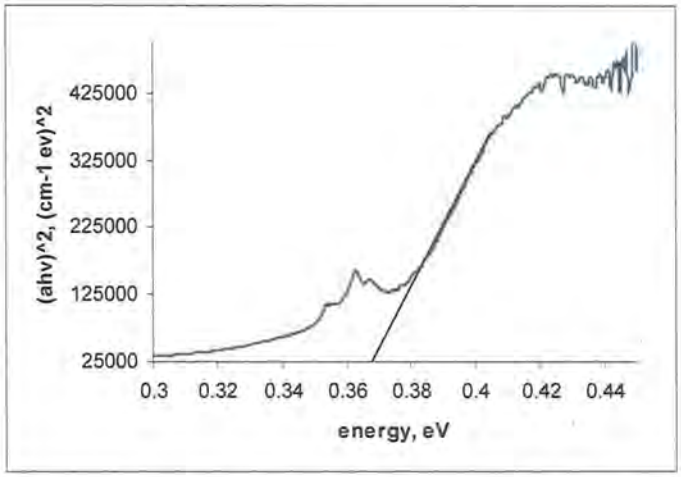

Fig. 4.8 Plot of energy against $(\alpha\hbar\nu)^2$ the extrapolation of the linear part as shown gives the optical band gap energy of the PbTe film

The wide range of linearity over the absorbed photon energy indicates a direct band gap. Extrapolation of the linear portion of the plot to the energy axis gives a band gap energy of 0.37 eV, this is in the region of the band gap energy measurement (0.33 eV) found for PbTe by Kumar *el al* [1]. The broad peak centred at 0.36 eV is probably due to residual surfactant on the film, the $-CH_2-$ groups of the surfactant molecules absorb IR of this energy strongly.

For comparison figure 4.9 shows the band gap energy plot for a bulk lead telluride film on silicon deposited from a solution of 50 mM lead acetate, 1 mM tellurium dioxide, 0.1 M nitric acid. This time the band gap energy is much closer to the literature value, just under 0.32 eV. This shift of the band gap energy to a higher energy level that is seen in the mesoporous material is probably caused by quantum confinement. Quantum confinement effects occur when the photo-generated charge carriers (electrons and electron holes) become trapped in the mesoporous structure, because the pore diameter is similar to the effective size of the charge carriers [2]. The "trapped" electrons require a higher energy to be promoted to the conduction band, i.e. the band gap energy becomes greater.

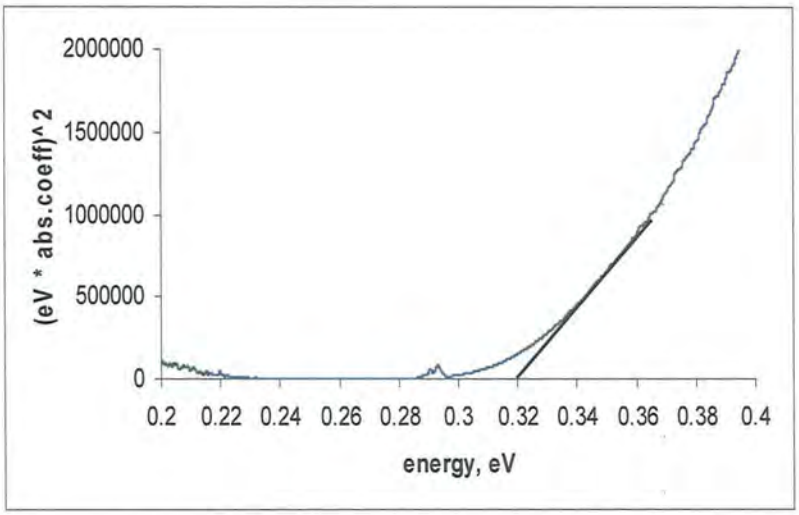

Fig. 4.9 Band gap energy plot of a bulk PbTe film on silicon indicating a band gap energy of 0.32 eV.

Figures 4.10 and 4.11 show SEM and AFM images of the film structure, in both micrographs crystalline structures are seen, some having a star shaped form. These structures can also be seen in the AFM image. These images support the wide angle XRD data indicating a polycrystalline film structure.

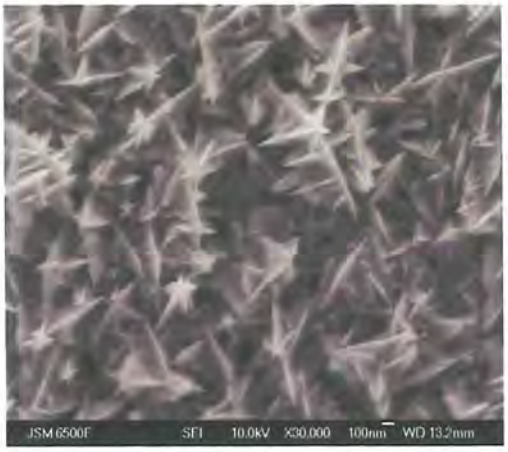

Fig 4.10 SEM micrograph of the film showing star shaped crystalline structures. Scale bar 100nm

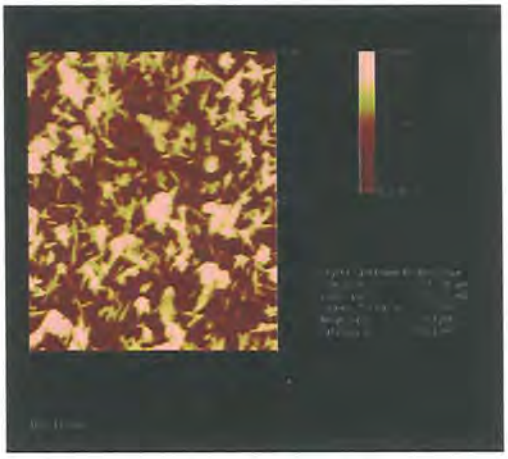

Fig. 4.11 AFM image of the film. Area shown is $5\mu m^2$

4.5 Deposition of mesoporous lead telluride films onto 3-MPTMS modified silicon substrates

The previous results describing the deposition of lead telluride onto silicon using the liquid crystal templating technique was fairly unique in the sense that the film showed good adherence to the silicon substrate. However this was often not the case, films would peel off the surface quickly after being immersed in IPA to remove the templating mixture. The most likely reason for this is that there is a large crystallographic lattice mismatch between lead telluride and silicon therefore there is a weak interfacial interaction between the lead telluride film and silicon substrate leading to the observed adhesion problems [3,4]. In fact this is also the case with other lead chalcogenide films. Often to get around this difficulty a buffer layer of barium fluoride, calcium fluoride or strontium fluoride is applied between the silicon substrate and the lead chalcogenide film to improve adhesion and stability [5]. Instead of using a buffer layer chemical modification of the silicon substrate surface using 3-mercaptopropyl-trimethoxysilane (3-MPTMS), $(CH_3O)_3SiCH_2CH_2CH_2SH$, (Aldrich, UK) was investigated. After pre-treatment of the wafer as described in 2.2 the silicon surface was "activated" by soaking in 5 M KOH for one minute to produce a hydroxyl terminated silicon surface. Then the wafer was rinsed in dry, HPLC grade ethanol (Rathburn, UK) three times to remove any water. The wafer was then soaked in a 10% ethanolic solution of 3-MPTMS overnight (up to 15 hours). After surface modification the wafer(s) were rinsed thoroughly with dry alcohol to remove excess 3-MPTMS. It is essential that the wafer is kept dry as any water would cause polymerisation of the 3-MPTMS rendering the modification process useless. Waste 3-MPTMS solution and ethanol used for rinsing was discarded into hypochlorite solution as this compound is harmful to the environment. Glassware used was also decontaminated in this solution. Figure 4.12 shows the surface modification process. Surface modification using 3-MPTMS has been used to create cadmium sulphide nanopartical coated electrodes [6]. Chemical modification of silicon substrates using other silane based reagents has also been carried out, successfully improving film adhesion [7,8].

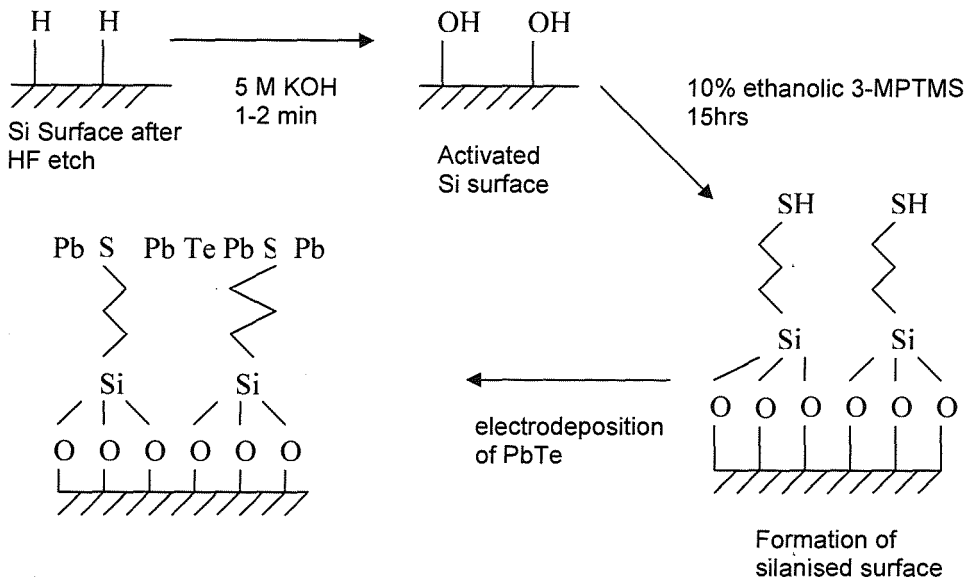

Fig. 4.12 Schematic of the formation of the chemically modified silicon surface using 3-MPTMS

Two films were deposited onto silicon wafers modified with 3-MPTMS. The first film was deposited using a liquid crystal template mixture consisting of 50 wt.% $C_{16}EO_8$ and 50 wt.% electrolyte solution with 500 mM $Pb(Ac)_2$, 10 mM TeO_2 and 1.5 M HNO_3. Silicon pre-treatment was by sonication for 30 minutes in IPA, soaking in a mixture of two volumes of H_2O_2, one volume of concentrated HCl and eight volumes water for 30 minutes at 80°C, then etching in 5 M HF for two hours. Deposition was at a potential of -0.50 V *vs.* SCE for 48 hours at ambient temperature. The longer duration of deposition was required because the modified surface is less conducting therefore reducing deposition rate. The films macroscopic appearance was patchy and dark grey. The mean film composition measured by EDXS was 81.69 at.% Te and 18.32 at.% Pb, tellurium rich. Compared to films deposited onto unmodified silicon the film adhesion was very strong. No peeling or film loss was observed after soaking for over 12 hours in IPA this was probably due to the film being strongly bound to the wafer via the 3-MPTMS layer. SEM showed a fairly rough nodular surface with small areas not covered by deposit, see figure 4.13.

Fig. 4.13 SEM micrograph of the first mesoporous film deposited onto modified silicon substrate. Scale bar is 10 µm.

Wide angle x-ray diffraction shows peaks for the (200), (220), (222) and (420) lattice planes for PbTe crystal structure. Peak positions and calculated lattice spacings were in good agreement with standard data [1], see figure 4.14. The sharp peaks in the diffractogram indicate a polycrystalline film structure with growth mainly in the (200) and (220) directions. The small angle XRD diffractogram shows a broad peak centred at about 1.85°, figure 4.15. This indicates the presence of a mesoporous structure over a short range, the absence of higher order diffraction peaks also suggests that the long range mesoporous structure is poor.

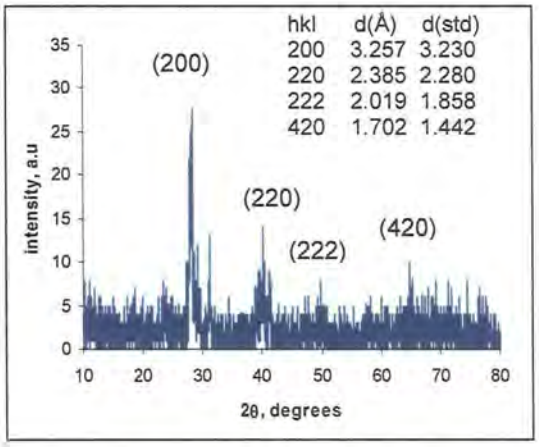

Fig. 4.14 Wide angle XRD of first mesoporous film using modified silicon surface.

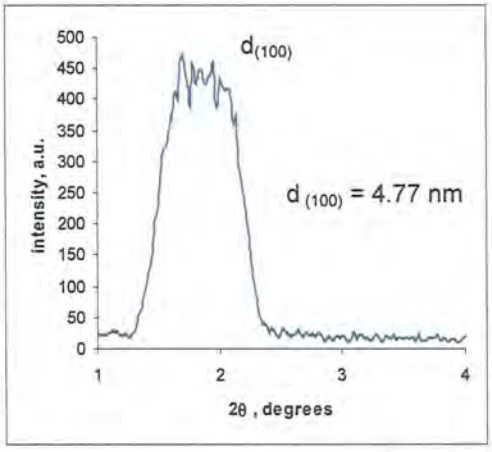

Fig. 4.15 Short angle XRD of the first mesoporous film indicating the nanostructure and the lattice spacing.

The second film with a mesoporous structure was deposited using a liquid crystal template of the same composition as used for deposition of the first film. Silicon

wafer pre-treatment was also not changed. The deposition potential was set at -0.55 V *vs.* SCE, which was more negative than the first deposition to improve the film composition. Duration of deposition was 29.25 hours. The film did not peel off during soaking to remove the template mixture, again showing that surface modification improved the film adhesion. The film composition measured by EDXS was approximately the same as the first film, 19.02 at.% Pb and 80.98 at.% Te. The wide angle XRD revealed a strong peak for the (200) planes and a much smaller peak for the (220) planes of PbTe at 28.28° and 40.26° respectively, figure 4.16. This indicates that the crystal growth is principally in the (200) direction. The higher order peaks which were seen for the first film were not present showing that crystal growth is more uniform than in the first film. Small angle XRD revealed a very broad asymmetrical peak wider than that seen for the first film between 1.1° to 2.5°, figure 4.17. This suggests that there is some mesoporous structure present but it is less well ordered than in the first film also no higher order diffraction peaks were observed. A very strong peak from the silicon substrate was present suggesting a thinner film and/or less uniform coverage of the silicon substrate.

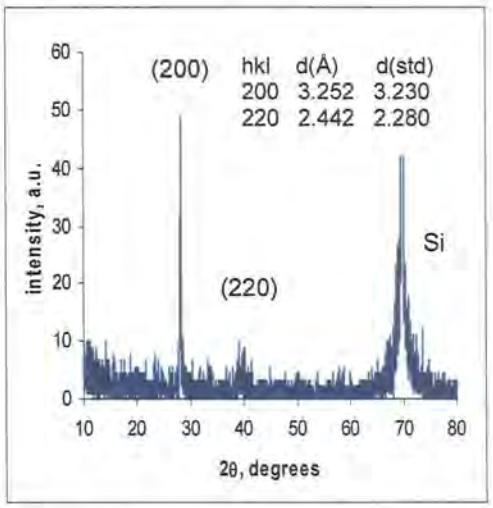

Fig. 4.16 Wide angle XRD of the second mesoporous film deposited on modified silicon

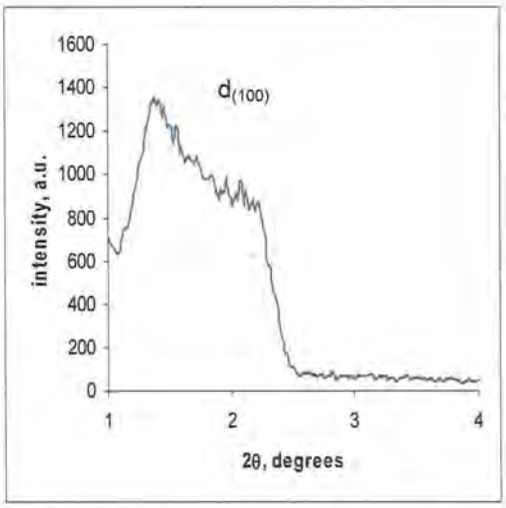

Fig. 4.17 Small angle XRD of the second film. The peak is indicative of a nanostructure

Electron microscopy of the film showed a smoother surface and more compact morphology than the first film, see figure 4.18 below.

Fig. 4.18 SEM micrograph of the surface of the second film deposited onto modified silicon. Scale bar is 10 µm

The highly tellurium rich compositions of these films is probably due to the high tellurium concentration in the electrolyte. Here the TeO_2 concentration was 10 mM, compared to the film discussed earlier which was almost stoichiometric a TeO_2 concentration of only 5 mM was used. The effect of using a higher concentration of TeO_2 has been investigated by Lincot and Lepiller. They showed that with increasing TeO_2 concentrations the potential range over which stoichiometric films were deposited was reduced and the tellurium content of electrodeposited films increased [9]. Therefore the use of higher TeO_2 concentrations should be avoided for stoicheometric film compositions.

4.6 Deposition of mesoporous PbTe on gold using a nucleation pulse

Several attempts were made to produce a mesoporous film on gold using a nucleation pulse deposition regime. The best two are presented here. The films were deposited using a liquid crystal template mixture consisting of 50 wt.% $C_{16}EO_8$ and 50 wt.% 50 mM $Pb(Ac)_2$, 1 mM TeO_2, 0.15 M HNO_3 electrolyte. Both films were deposited using the same deposition regime, a nucleation pulse at -0.70 V *vs.* SCE for 3 seconds then deposition at -0.45 V *vs.* SCE for 3 hours. For the first film to improve the coating of the template mixture on to the gold substrate the mixture was gently heated on a warm hotplate after being put on to the substrate until it was liquefied. Then it was cooled back slowly to reform the hexagonal phase before cell construction was finished. The deposited film on visual inspection was mostly smooth and metallic grey. SEM

revealed a smooth and uniform morphology, figure 7.28. The mean film composition obtained from ten EDXS measurements was 47.04 at.% Pb, almost stoicheometric.

Fig. 4.19 SEM micrograph of the first H_1-PbTe film using a nucleation pulse. Scale bar is 10 µm.

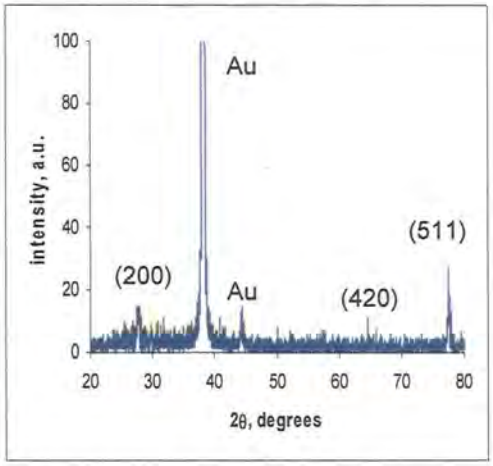

Fig. 4.20 Wide angle XRD of the first film.

The wide angle x-ray diffractogram shows diffraction peaks for the (200), (420) and (511) lattice planes. Although the peak assigned for the (511) direction could also be from diffraction from tellurium (114) planes which also give a peak around this range of diffraction angles. The small angle x-ray diffractogram of the film (figure 4.21) shows a broad peak centred at 1.36° (2θ). This indicates the possibility of a mesoporous structure with a d-spacing of 6.5 nm and a pore to pore spacing of 7.4 nm, although the long range order of the mesoporous structure is probably poor as indicated by the wide peak and the lack of higher order diffractions.

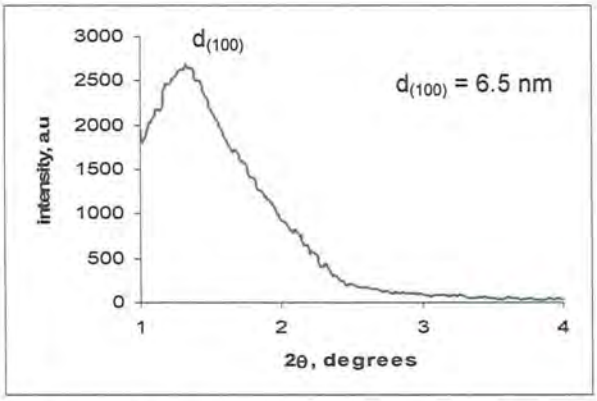

Fig. 4.21 Small angle XRD of the film indicating the presence of a mesoporous structure

For the second film the template mixture was not heated and melted before completing cell preparation. The deposited film looked shiny and metallic. The mean composition from ten EDXS measurements this time indicated a lead rich deposit, 57.74 at.% Pb. The SEM micrograph showed a smooth and featureless film surface, figure 4.22.

Fig. 4.22 SEM micrograph of the second H_1-PbTe film using a nucleation pulse. Scale bar is 10 µm

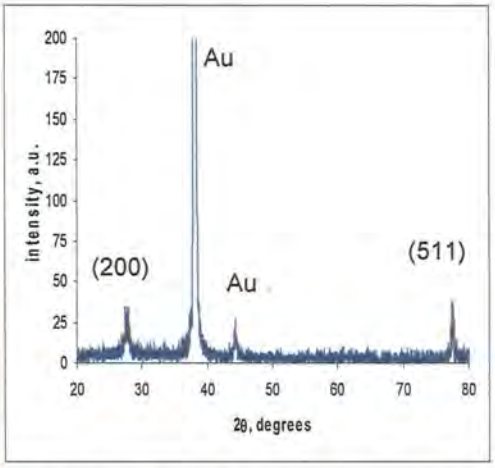

Fig. 4.23 Wide angle XRD of the second film

The wide angle x-ray diffractogram indicates that the direction of growth is the (200) and the (511) lattice planes. No peak is seen for growth in the (420) direction. Figure 4.24 is the small angle x-ray diffractogram of the film.

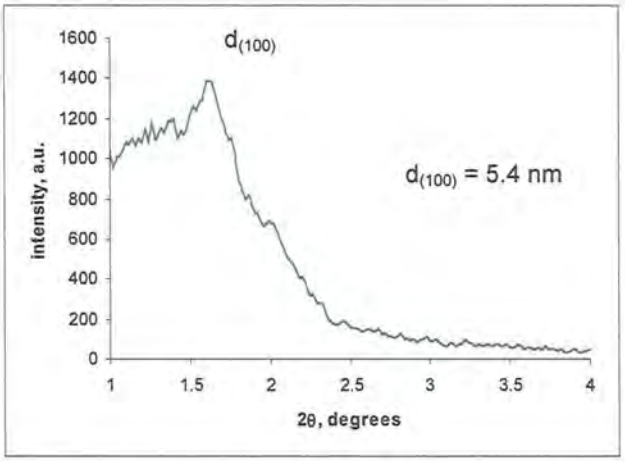

Fig. 4.24 Small angle XRD of the second film indicating the presence of a mesoporous structure

The diffractogram shows a peak centred at 1.64° (2θ) indicating that a mesoporous structure within the film is present. The peak position corresponds to a d-spacing of

5.4 nm with a pore to pore spacing of 6.2 nm. Again the peak is not will defined and there are no higher order diffraction peaks which suggests that the long range order of the mesoporous structure is poor. Figure 4.25 is a TEM image of a mesoporous PbTe film deposited onto gold. In this case no nucleation pulse was used. The pores are seen from the side and appear as lighter lines.

Fig. 4.25 TEM micrograph of a H1-PbTe film deposited on to gold. The scale bar is 50 nm.

4.7 Investigating the formation of porous silicon surface using AFM

Another approach to improve the adhesion of lead telluride films directly deposited onto silicon is creating a porous silicon surface. The porous surface has a much higher surface area and acts like a sponge allowing improved adsorption of the deposited film. The first instance of using a porous silicon substrate was by Bondarenko *et al* [10] who grew lead sulphide films by molecular beam epitaxy onto porous silicon. Lead telluride films have been grown by vacuum deposition onto porous silicon by Zimin *et al* [3]. A porous silicon surface can be produced by stain etching. The silicon substrate is immersed in a solution of concentrated hydrofluoric and nitric acid (500 parts HF to one part nitric acid) for up to ten minutes [4,11,12]. Also the silicon can be anodically etched in concentrated hydrofluoric acid to create the porous surface [13]. The formation of the porous surface as a function of time was investigated using atomic force microscopy. This was done by etching small pieces of silicon in an etching solution consisting of 500 parts of 48% HF to one part concentrated nitric acid. Sodium nitrite was also added to the solution with a concentration of 0.1 g/L to

homogenise the etching. Etching was for one, five and ten minutes, an unetched piece of silicon was used as a control. Tapping mode AFM was used to examine the surface structure. Figures 4.26 to 4.29 show AFM profile images of the surfaces. The unetched silicon surface shows a relatively smooth surface. After etching for one minute a dramatic change is evident where a porous topography is formed. After five minutes the porosity increases further, the layer of porous silicon appears to get thicker up to this point the porous structure looks fairly homogenous. However after ten minutes the porous structure seems to become less even. The increase in the homogeneity of the porous layer for longer etching times has been also been noted by Abramof *et al* [11] they attribute this effect to the formation of hydrogen bubbles during the etching process. These bubbles form in the etched pores, as the porous layer becomes thicker they prevent the etching solution from reaching the silicon surface and therefore prevent or reduce the rate of etching. This produces different etching rates in different locations depending on the size and number of bubbles being formed, and hence an uneven inhomogeneous porous surface is formed.

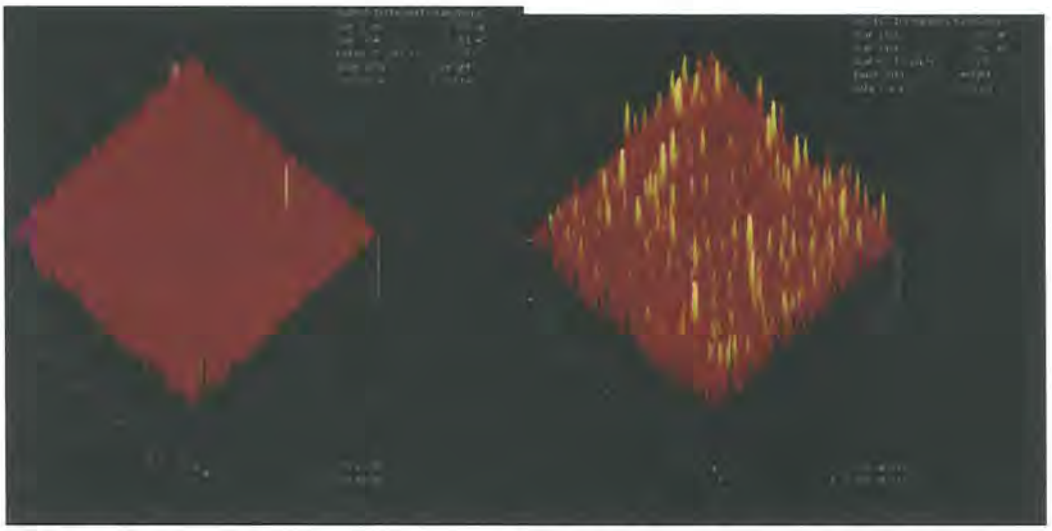

Fig. 4.26 AFM image of unetched silicon substrate surface. Area of scan, 1 μm^2 data scale height, 2nm

Fig. 4.27 AFM image of silicon substrate surface after etching in 500:1 48% HF/ conc. nitric acid for one minute. Area of scan, 1 μm^2, data scale height, 2nm

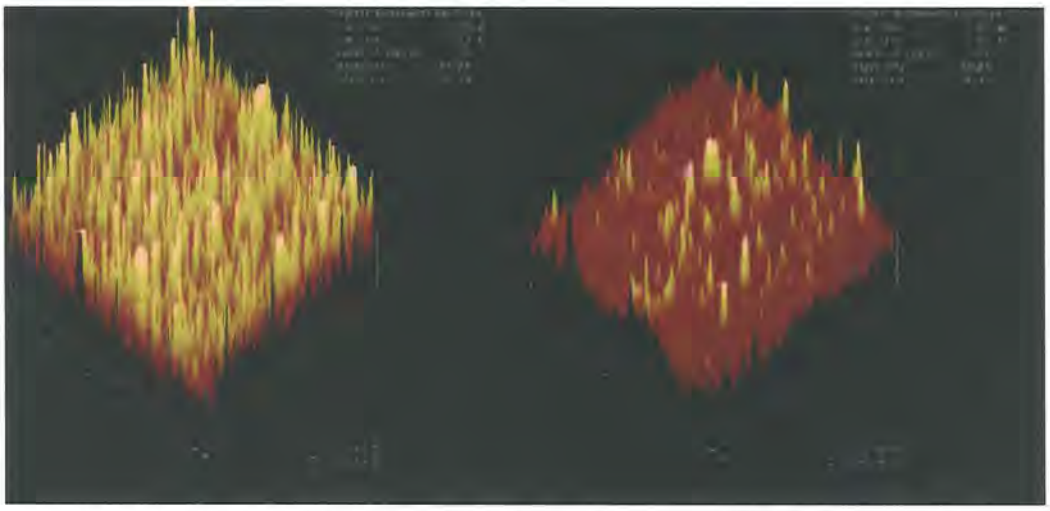

Fig. 4.28 AFM image of silicon substrate surface after etching in 500:1 48% HF/ conc. nitric acid for five minutes. Area of scan, 1 μm^2, data scale height, 2nm

Fig. 4.29 AFM image of silicon substrate surface after etching in 500:1 48% HF/ conc. nitric acid for ten minutes. Area of scan, 1 μm^2, data scale height, 2nm

4.8 Conclusions

Initial investigation of the liquid crystal template mixture using $C_{16}EO_8$ and 50 mM $Pb(Ac)_2$, 1 mM TeO_2 0.15 M HNO_3 showed that the phase behaviour was not significantly affected by the presence of the electrolyte. The phase diagram was comparable to that of $C_{16}EO_8$ and water. The hexagonal phase was stable over a wide composition range. The small angle XRD showed that a 50 wt.% $C_{16}EO_8$ composition had a well ordered hexagonal phase structure at room temperature. The optical texture revealed by POM also indicated that the hexagonal phase was present. All mixtures with this composition had the streaky "feathery" appearance typical of this phase. The hexagonal phase was stable up to around 65°C. Small angle XRD of a liquid crystal template made with an electrolyte containing 500 mM $Pb(Ac)_2$, 10 mM TeO_2 1.5 M HNO_3 showed that the hexagonal phase was breaking down and the long range order of the structure was much poorer. This is probably due the ionic species at higher concentration interfering with the assembly of the cylindrical micellar structures. This affect has also been seen with $C_{16}EO_8$ and cadmium sulphate solution liquid crystal mixtures [14].

Deposition of mesoporous films onto silicon proved to be difficult. Often the film would peel off the surface when placed in IPA to remove the liquid crystal template. This usually occurred after a few minutes of immersion. The most probable

reason for this is due to a large crystal lattice structure mismatch between silicon and lead telluride [3,4]. One film showed improved adhesion suggesting that occasionally PbTe films can grow directly on silicon, however this appears to occur rarely. Wide angle XRD indicated the film was polycrystalline, small angle XRD could not provide any evidence of a hexagonal mesoporous structure. Measurement of the band gap energy by FTIR was 0.37 eV, a bulk PbTe film on silicon had a band gap of 0.32 eV closer to the literature value. The shift to a higher band gap energy could possibly be due to a quantum confinement effect indicating the presence of a mesoporous structure in the film.

Using 3-MPTMS to modify the silicon substrate surface proved at least partially successful. The deposited film was strongly adherent and did not peel after several hours of soaking to remove the templating mixture. However the deposited films were not very uniform and the composition was poor. The poor composition is possibly due to the higher (10 mM TeO_2) concentration leading to tellurium rich films. It would be useful to repeat the experiment using the electrolyte with TeO_2 at the lower concentration of 1 mM. The small angle XRD diffractograms for both films indicated that a mesoporous structure was present but with a poor long range order. The higher concentration of ionic species in the electrolyte could possibly be contributing to the reduced long range order of the mesoporous structure. Again it would be interesting to see if using the lower concentration electrolyte would improve this.

Using a double pulse deposition regime to deposit mesoporous lead telluride films on gold was successful. Both films were smooth uniform and metallic in appearance and had a reasonably good composition. The films were thin since the deposition periods were short, a longer deposition duration produced films that were powdery and polycrystalline. These findings are similar to the bulk PbTe films deposited onto silicon. Therefore there is a trade off between film quality and thickness. Small angle XRD of both films showed that there was possibly a mesoporous structure present but with a poor long range order.

References

1. S. Kumar, Z.H. Khan, M.A. Majeed-Khan, M. Husain. *Curr. Appl. Phys.* **(2005)**, vol. 5, pp. 561-566

2. K.S. Rathorea, D. Patidara, Y. Janub, N.S. Saxenaa, K. Sharma, T.P.Sharma, *Chalcogenide Lett.* **(2008)**, vol. 5, p. 105-110

3. S.P. Zimin, M.N. Preobrazhensky, D.S. Zimin, R.F. Zaykina, G.A. Borzova, V.V. Naumov *Infrared Phys. and Tech.* **(1999)**, vol. 40, pp. 337-42

4. C.R.B. Miranda, P.G. Abramov, F.C.L. de Melo, N.G. Ferreira, *Materials Res.* **(2004)**, vol. 7, p. 619-623

5. H. Zogg, M. Huppi, *Appl. Phys. Lett.* **(1985)**, vol. 47 p. 133

6. S. Drouard, S.G. Hickney, D. J. Riley. *Chem Commun.* **(1999)**, pp. 67-68

7. R.A Simon, A.J Ricco, M.S. Wrighton. *J. Am. Chem. Soc*, **(1982)**, vol. 104, pp. 2031-2034

8. M.S. Wrighton. *Science,* **(1986)**, vol. 231, pp. 32-37

9. 48. C. Lepiller, D. Lincot, *J. Electrochem Soc.* **(2004)**, vol. 151(5), pp. C348 – C357

10. V.P. Bondarenko, N.N. Vorozov, V.V. Dikareva *et al. Tech. Phys. Lett.* **(1994)**, vol. 20, p. 51

11. P.G. Abramof, N.G, Ferreira, A.F. Beloto, A.Y. Ueta, *Journal of Non-Crystalline Solids,* **(2004)** vol. 338–340, pp. 139–142

12. E. Vazsonyi, E. Szil´agyib, P. Petrika, Z.E. Horv´atha, T. Lohnera, M. Frieda, G. Jalsovszky. *Thin Solid Films*. **(2001)**, vol. 388, pp. 295-302.

13. K. Imai, H. Unno. *IEEE Trans. on electron dev.* **(1984)**, vol. 31, p. 297-302

14. T. Gabriel, PhD thesis, University of Southampton, **(2005)** p. 82-83

Chapter 5

Final conclusions and further work

5. Final conclusions and further work

The findings of this research project show that the deposition of mesoporous and bulk lead telluride films has been partially successful. The electrochemistry of the deposition of lead telluride on silicon and gold from acidic aqueous solutions of lead acetate and tellurium dioxide was investigated. Current densities seen for the deposition of mesoporous lead telluride are much smaller because of the lower diffusion rate of lead and tellurium ionic species through the denser liquid crystal template mixture. As a consequence of this longer deposition times are required for deposition of mesoporous films compared to bulk films. The underpotential co-deposition process was demonstrated using cyclic voltammetry experiments. Films were easier to deposit directly onto gold. Direct deposition of lead telluride films onto silicon was much harder due to the poor lattice mismatch between the two materials. Chemical pre-treatment of the silicon substrate using 3-MPTMS improved film adhesion, but the films deposited on pretreated silicon wafers were not uniform and were heavily tellurium rich. The band gap energy of a bulk film on silicon was measured by FTIR and was found to be 0.32 eV which is close to the literature value of PbTe. Some evidence of a mesoporous structure was seen for films deposited onto gold and pretreated silicon substrates from small angle x-ray diffractograms of the films but the long range mesoporous structure was probably poor. A nucleation pulse technique also seemed to have some positive effect on film morphology for films deposited on both gold and silicon but no significant effect on composition was seen.

Further work is needed to improve the film composition and morphology of films deposited onto silicon wafers pre-treated with 3-MPTMS. The films described in this work using this technique used an electrolyte with a high tellurium concentration (10 mm TeO_2). Experiments should be performed using the lower concentration solution, 50 mM $Pb(Ac)_2$, 1 mM TeO_2, 0.15 M HNO_3 to see if the lower tellurium concentration improves the film composition. Experiments could be performed to find the optimum duration of the modification of the silicon surface with 3-MPTMS. Perhaps producing a series of films over the potential range used for the bulk films described in section 3.4 could be attempted to determine the potential that produces the best film composition and morphology. Bulk films on pretreated silicon substrates over the same potential range should also be deposited as only mesoporous

films on pretreated substrates were made. More work should be performed using the double pulse nucleation technique. The deposition of mesoporous PbTe films on silicon using this technique could be carried out for instance as this was not properly covered in the experiments. Another possibility would be to perform pre-treatment of silicon wafers with 3-MPTMS and then try bulk and mesoporous depositions using the nucleation pulse technique. The band gap energy of these films could also be measured by FTIR to see if pre-treatment with 3-MPTMS and the nucleation pulse technique has any effect on this parameter. Finally the mesoporous structure of deposited films could be investigated further with AFM. This could be done on films deposited using the nucleation pulse technique and chemical pre-treatment. Also to obtain more direct evidence of a mesoporous structure more TEM work could be done on films that small angle XRD suggests that a mesoporous structure is present. Finally for deposition on to silicon, the effect of using silicon wafers with a higher phosphorous doping could be investigated. The increased phosphorous doping would possibly improve the semiconductor properties of the wafer hopefully leading to better film morphology and adhesion.